Karlsruhe Institute of Technology

Studies of the muon content in extensive air showers with the IceCube/IceTop surface array

Studien des Anteils von Myonen in ausgedehnten Luftschauern mit dem IceCube/IceTop Oberflächendetektor

Master's Thesis of

Sally-Ann Browne

at the
KIT - Department of Physics
Institute of Experimental Particle Physics (ETP)
Institute for Astroparticle Physics (IAP)

Reviewer:	Prof. Dr. R. Engel
Second reviewer:	Prof. Dr. K. Valerius
Advisor:	Dr. D. Kang and Dr. A. Haungs

24th September 2020 – 23rd September 2021

I declare that I have developed and written the enclosed thesis completely by myself, and have not used sources or means without declaration in the text. I have respected the rules for safeguarding good scientific practice at the Karlsruhe Institute of Technology (KIT) in its relevant version.

Karlsruhe, 15th September 2021

. . . . . .
(Sally-Ann Browne)

. . . . . .
(Prof. Dr. Ralph Engel)

Abstract

Studies of the muon content in extensive air showers with the IceCube/IceTop surface array

The IceTop surface array is an air shower detector at the South Pole with the goal to study cosmic rays in the energy region of 100 TeV to EeV. It operates an array of ice-Cherenkov tanks which detect the Cherenkov light emitted by traversing secondary particles of the incident air showers. The light detection results in a charge signal which is either in coincidence with the signal capture in a neighboring tank (HLC signal) or not (SLC signal). So far, only HLC charge distributions are then used for air shower reconstruction and other analysis. However, there are currently a few studies performed with the attempt to effectively include SLC charges in the cosmic-ray mass composition analysis at IceTop.
SLC signals have the advantage over HLC signals that they are more often created by single muons. Especially the detection of muons is of high interest because it was shown that the muon number in an extensive air shower depends on the mass of the primary particle initiating the air shower. Therefore, SLC signals hold the potential to advance the studies of the cosmic-ray mass composition.
This thesis contributes to those composition studies by investigating the character of SLC charge signals and compare simulated with experimentally derived distributions. The latter one is an important step to reassure that the ongoing SLC studies can continue to rely on the use of simulated datasets for the development of new analytical parameters and methods. The comparison performed in this thesis showed that the Monte-Carlo simulations are good enough to be used for composition analysis with SLC signals, despite having some smaller deviations to experimentally measured SLC signals. Likewise, it was found that differences due to the use of various hadronic interaction models are small for studies using the SLC charge signals.

Zusammenfassung

Studien des Anteils von Myonen in ausgedehnten Luftschauern mit dem IceCube/IceTop Oberflächendetektor

Das IceTop Oberflächenfeld ist ein Luftschauerdetektor am Südpol mit dem Ziel, kosmische Strahlung im Energiebereich von 100 TeV bishin zu EeV zu untersuchen. Es operiert ein Feld aus Eis-Cherenkov-Tänken, welche das Cherenkov-Licht detektieren, das von den durch den Tank propagierenden Sekundärteilchen der einfallenden Luftschauer emittiert wird. Die Lichtdetektion resultiert in einem Ladungssignal, welches entweder zeitgleich mit einem Signal in einem anderen Tank aufgenommen wurde (HLC Signal) oder nicht (SLC Signal). Bislang werden nur HLC-Ladungssignale für die Luftschauer-Rekronstruktion und andere Analysen benutzt. Jedoch werden zur Zeit mehrere Studien durchgeführt mit dem Versuch, ebenfalls SLC-Ladungsverteilungen effektiv in IceTops Analysen der Massenzusammensetzung von kosmischer Strahlung miteinzubeziehen.
SLC Signale haben den Vorteil gegenüber HLC Signalen, dass sie mehrheitlich von einzelnen Myonen erzeugt werden können. Besonders die Detektion von Myonen ist von großem Interesse, da gezeigt wurde, dass die Myonenanzahl eines Luftschauers von der Masse des Luftschauer erzeugenden Primärteilchens abhängt. Deshalb tragen SLC Signale das Potential, die Studien der Massenzusammensetzung von kosmischen Strahlen weiter voranzubringen.
Diese Arbeit verfolgt das Ziel, einen Teil zu diesen Untersuchungen der Zusammensetzung beizutragen, indem der Charakter von SLC-Ladungssignalen erkundet und ein Vergleich zwischen simulierten und experimentell gefundenen Verteilungen gezogen wird. Letzteres ist ein wichtiger Schritt hin zu der Vergewisserung, dass aktuelle SLC Studien sich weiterhin auf den Gebrauch von simulierten Datensätzen verlassen können, um neue analytische Parameter und Methoden zu entwickeln.
Der in dieser Arbeit durchgeführte Vergleich zeigte, dass die Monte-Carlo-Simulationen gut genug für die Verwendung in Kompositionsanalysen mit SLC-Ladungssignalen sind, trotz einiger kleiner Abweichungen zu experimentell gemessenen SLC-Signalen. Auch wurden für diese Art von Studien keine großen Unterschiede bei der Verwendung von unterschiedlichen hadronischen Wechselwirkungsmodellen festgestellt.

Contents

List of Figures

List of Tables

1. Introduction

Studying cosmic rays has been a very active field of research since their discovery in 1912. Cosmic rays are high-energetic atomic nuclei from protons to iron nuclei and even a few heavier nuclei, which originate from within and outside our Galaxy. The energy spectrum of primary cosmic rays (the flux of cosmic ray particles reaching the Earth per energy unit) reveals some characteristic features which hold information about the particles' origin, acceleration and mass composition.
The origin of cosmic rays and their propagation mechanism are not completely understood yet, and there exist a lof of theories which need to be confirmed or discarded with the help of experimental findings.
There are many experiments which detect cosmic rays either directly or indirectly. The indirect method is used in ground-based detectors where the secondary particles of extensive air showers are detected. Here, secondary particles are mainly electrons/positrons and photons (the electromagnetic shower component) and muons and neutrinos (the muonic component). Muons play an important role in air shower detection. One reason is that their number in a shower is directly dependent on the mass of the cosmic ray particle which generated the air shower. Another reason is that muons leave a trace of the hadronic interactions which need to be understood in order to interpret the air shower. Thus, the muon content is of high interest in any cosmic ray composition study.

One of many experiments based on the ground is the IceTop experiment, the surface array of the IceCube Neutrino Observatory at the South Pole. IceTop's goal is the investigation of cosmic rays with energies from several TeV to EeV. As any ground-based experiment, IceTop detects extensive air showers initiated by cosmic rays. IceTop uses ice-Cherenkov detectors in which the Cherenkov light emitted by traversing charged secondary particles is measured and transformed to charge signals. There are two types of charge signals: The Hard Local Coincidence (HLC) charge signals, i.e. two neighboring tanks show signals, and the Soft Local Coincidence (SLC) charge signals, i.e single tank signals. While the standard detection mode of IceTop is collecting HLC signals, it was lately proposed to also include SLC signals. The reason is that SLC signals carry information about single muons reaching the detector which can't (or very unlikely) be captured by HLC signals. Thus, SLC signals are relevant for composition studies at IceTop.
Since SLC signals have not yet been used in the standard procedure of IceTop's data analysis, this thesis focuses on the inspection of those SLC signals, more precisely the SLC charge distributions which contain all SLC signals within a certain distance range from the shower core. In particular, the simulated SLC charge signals are looked at and compared to experimentally measured signals. A good agreement of both, simulation and experimental

data, is crucial as any analysis relies on the usage of simulated datasets. If the comparison is satisfactory, then the base, namely reliable simulation, for developing new analytical methods including SLC charge signals is confirmed.

The next Chapter 2 will give an introduction to cosmic rays with a short historical review, followed by a summary of physical characteristics and experimental methods for the detection of cosmic rays. Chapter 3 will cover the physical basics of extensive air showers. Then, Chapter 4 will be about the IceTop experiment, explaining its setup and signal capture. The last part of that chapter will deal with the Monte Carlo simulations used in IceTop. Chapter 5 will describe the analysis which was performed in this thesis. The results will be shown and discussed in Chapter 6 where only main plots will be presented. The rest of the plots created during the analysis are collected in Appendix A. A conclusion and an outlook will be given in Chapter 7.

2. Cosmic Rays

As an introduction to the physical motivation of this thesis, the very first chapter is dedicated to cosmic rays. In this chapter, an historical and theoretical overview of cosmic rays will be given. Extensive air showers will be discussed in detail in Chapter 3.

2.1. History

The discovery of cosmic rays dates back more than 100 years, and followed another fundamental physical discovery from 1896, which was the natural radioactivity. Scientists started to investigate radioactive sources and their radiation, amongst other things the radiation's absorption in ambient air. Having found the Earth as the main source of natural radioactive radiation and knowing about the ionizing effect of this radiation, it was assumed that the air would become less ionized with increasing height due to its absorption in air.
In 1912, the Austrian physicist V. Hess undertook several balloon flights with the goal to measure the ionization of the atmosphere. The expectation of the measurement results in that time was clear: The ionization of air should have decreased and even completely disappeared with higher altitudes because the radioactive radiation of the Earth was supposed to be fully absorbed at the altitudes Hess' balloon was flying (up to 5000 m). Instead, Hess found the atmosphere to become more ionized with increasing height. He was able to prove that the yet unknown ionizing radiation was neither coming from the Earth nor the sun, by performing his ionization measurements at different altitudes, partially at day and partially at night. However, Hess' observation did not receive a lot of attention until it was confirmed by the German physicist W. Kolhörster in 1913. Kolhörster undertook balloon flights to altitudes up to 9000 m where he found even higher ionization rates than Hess did in his measurements [1].
The observation of Hess and Kolhörster led to the question about the physical nature of the mysterious ionizing extraterrestrial radiation. Gamma rays were first believed to be the reason for the air ionization. This theory was discarded many years later when it was discovered that charged, high-energetic particles were responsible for the ionization phenomenon. Those particles are referred to as cosmic rays and are studied since the day of their discovery. In the first few decades of cosmic ray studies, the cloud chamber and the emulsion chamber were very useful instruments to detect and track cosmic ray particles. With these experimental methods it was possible to discover new particles like the positron in 1932 or the charged pion in 1947 [2]. The development of new technologies as well as the continuous gain in knowledge of particles and particle interactions brought the research of cosmic rays on a whole new level. At this stage, many experiments exist worldwide and in space, differing in their setup, detection method and analysis tools. Some use detectors

which cover a large area to measure secondary particles of so-called Extensive Air Showers initiated by cosmic ray particles, while others are space-based or attached to balloons, in order to measure cosmic rays directly. An overview of modern experimental methods for the research of cosmic rays will be given in Section 2.4. The main goals of all experiments are the same: Finding out about the identification, origin, and energy (including acceleration and propagation mechanisms) of the cosmic ray particles.

2.2. Composition and origin

The amount of experimental data gathered over many decades made it possible to show what charged particles the cosmic rays are composed of. Protons account for the greatest part of cosmic rays. But heavier nuclei up to iron were also observed in the cosmic radiation. Those particles are called the primaries. The flux of primary particles that reach the Earth is dependent on their energy, location of origin and propagation. The energy will be looked at in Section 2.3. Secondary particles are produced through the interaction of primary particles with the molecules of the medium they traverse.
Figure 1 shows the composition of cosmic rays (up to Cupper nuclei) compared to the elemental abundances of the solar system [3].

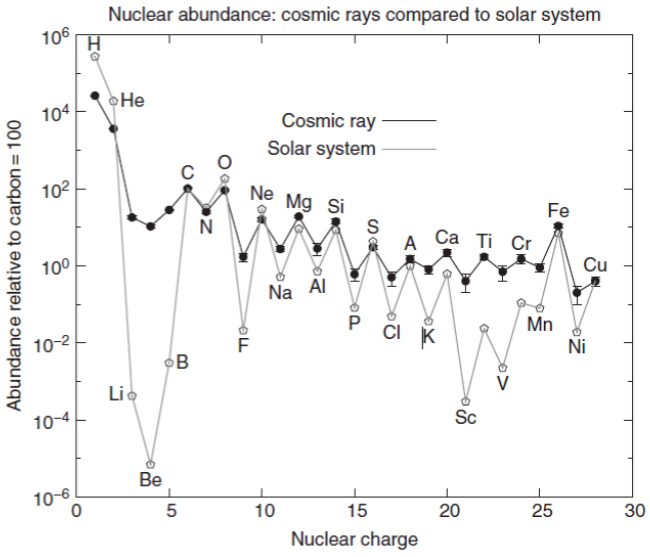

Figure 1: The elemental abundances in cosmic radiation measured on Earth (filled symbols connected by solid lines) compared to the one in the solar system (open symbols), all relative to carbon = 100, for particles in GeV range [3].

There are obvious differences between the cosmic radiation and solar system abundances in which one of them gives an interesting clue about the propagation of cosmic ray nuclei: The abundances of the light nuclei Li, Be and B (Lithium, Beryllium and Boron) as well

as of the heavier nuclei Sc, Ti, V, Cr and Mn (Scandium, Titanium, Vanadium, Chromium and Manganese) are considerably higher in cosmic rays. This can be explained with the process of spallation which takes place when cosmic rays collide with particles from the interstellar medium through which they propagate. In this process the above-mentioned nuclei are ejected from heavier nuclei (Carbon and Oxygen or Iron). Thus, the spallation products can also be counted as secondary cosmic rays. The detectable ratio of primaries and secondaries can give information about the distance [3] which the cosmic rays have traveled, or the residence time [4] of the cosmic rays in the Galactic disk. However, to do so, several assumptions need to be made, i.e. the source of the cosmic rays lies within our Galaxy, or the cosmic rays gather their grammage (this means their mass per unit of area) while being in the interstellar medium rather than inside their source. This shows the strong connection between studies of cosmic-ray compositions and studies of their origins [4].

The elemental abundances can be studied very well with balloon or satellite-borne detectors which directly measure the primary's charge to identify the detected particle (see Section 2.4). This is only possible for particles of low energies up to TeV. However, the steeply falling flux of particles makes it very difficult to extend direct measurements even by one decade in energies. The mass composition for higher energies (above TeV) is harder to obtain because the detection is done solely indirect (see Section 2.4), and the elemental abundances as well as the mass composition are found by fitting simulated mass groups (not individual particle masses) to the measured atmospheric depth of the detected air shower. Commonly used simulated mass group templates are Proton, Helium, Nitrogen, and Iron nuclei. There are several simulation models available which mostly differ in their calculation of hadronic interactions. The comparison of experimental data with the simulation templates indicates the trend of the composition towards light, intermediate or heavy nuclei in certain energy ranges. The mass composition analysis at high energies is limited by the uncertainties that come with the choice of the simulation model, and the amount of experimental data. Even though those observed "mass trends" can already contribute to the investigation of the origin and propagation of the detected primary particles, there is still the need for ground-based experiments with a good mass resolution, especially, for the ultra-high energy range [5].

Finding the sources of origin of cosmic rays is not a trivial task, because the particles carry electrical charge and therefore get deflected in the interstellar magnetic fields before reaching the Earth. Therefore, it is still a very active field of research to find out what the cosmic rays originate from. On the one hand, the proposed sources must be able to accelerate charged particles to very high energies, unless the particles gain the majority of their energy during their travel through the interstellar medium. On the other hand, they need to lead to the observed chemical composition of cosmic-ray particles. Information and clues about the sources of cosmic rays can be obtained by looking closely at the behavior of elemental abundances and energy spectra (see Section 2.3) of cosmic rays. But also including the studies of gamma rays and neutrinos, as it is done in multi-messenger astroparticle

physics [5], can reveal relevant information. Gamma rays and neutrinos are secondary particles of the interaction of cosmic rays with the source or the interstellar medium. In fact, it was shown by the observation of gamma rays, that the bulk of cosmic rays in the GeV region is coming from within our Galaxy. Cosmic rays at higher energies might stem from extragalactic sources.
One of the well-known and mostly accepted candidates of galactic sources is the supernova and its' remnant in the Galactic disc. Supernova explosions are very energetic and powerful enough to create the particle acceleration which could lead to the observed cosmic ray energy spectrum. The acceleration process can be explained more specifically with the Fermi acceleration mechanism [3]. This mechanism describes how charged particles are accelerated by moving gas clouds (second-order mechanism) or shock fronts (first-order mechanism) from supernovae through the diffusion in the clouds' turbulent magnetic fields [3]. The case of a supernova shock front is shown in Figure 2.

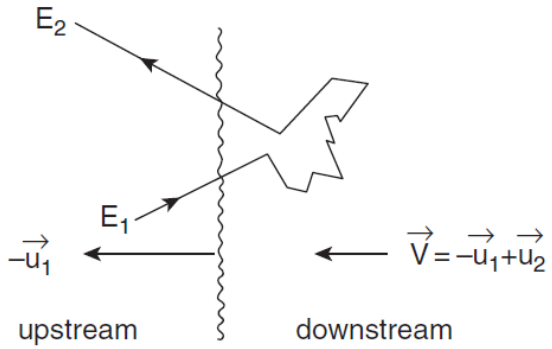

Figure 2: First-order Fermi acceleration at a plane shock front [3].

When a star is exploding (supernova), it sends out a shock front with velocity $-u_1$ and the supernova remnant expands. u_2 is the velocity of the gas behind the shock wave. When the cosmic ray particle (upstream) ejected by the supernova is overtaken by the shock wave, it gets irregularly deflected in the turbulent magnetic fields of the shocked gas (downstream) behind the shock wave. The elastic diffusion moves the particle along with the gas until it leaves this region through the shock front again. As the particle escapes through the shock front, its energy changes from E_1 before scattering to E_2, with the relation given by Equation (1).

$$E_2 = \Gamma^2 E_1 (1 - \beta \cos\theta_1)(1 + \beta \cos\theta_2'). \tag{1}$$

Γ and $\beta = v/c$ are the Lorentz factor and velocity of the cloud, where v is the velocity of the shocked gas and c is the speed of light. θ_1 and θ_2' are the angles of the particle's trajectory as it enters and leaves the downstream area relative to the direction of travel of the shock front. The collision with the shock front can happen many times, and with each time the cosmic ray's energy is changed. In case of a gas cloud, E_2 can be smaller than E_1 for certain angles and so the collision results in an energy loss. But in case of shock fronts which are approximated as large plane shocks, only energy gain is possible because, just for geometrical reasons, the term $\cos(\theta_1)$ will always have a negative value, and $\cos(\theta_2')$

will always be positive. An estimation of the maximum energy that cosmic rays can reach through the Fermi acceleration is given in Equation (2), under the assumption that the magnetic field in the acceleration region is approximately the same as in the interstellar medium with ≈ 3 μG. But the magnetic field could also have much higher strengths. The maximum energy gives then

$$E_{max} \leq Z \times 3 \times 10^4 \text{GeV}. \tag{2}$$

Z is the particle's charge. E_{max} might be influenced by nonlinear effects of the accelerated particle on the turbulent magnetic field, which would increase the magnetic field. This theory is still under investigation.

The scenario of supernova remnants as source of origin and acceleration is only one plausible theory. Other galactic source candidates are explosive events in the Galactic center and stellar winds [3]. A good overview of possible cosmic ray sources provides the Hillas plot, which is shown in Figure 3. The plot shows the magnetic field strength and the size of known Galactical and extragalactic objects. The general maximal energy that particles can reach through the acceleration in any kind of object, is depending on the radius R of the object as well as the magnetic field B and charge Ze of the particle. Here, the gyroradius r_L of the circular motion of the accelerated particle in the magnetic field has to be smaller than R as long as the acceleration process continues. This condition is often called the "Hillas condition" [5]. When r_L becomes bigger than R, the particle is no longer confined within the object, so it leaves the acceleration region. So, the general expression of E_{max} per nucleus is the one in Equation (3), with $r_L < R$,

$$E_{max} < Z \times e \times B \times R. \tag{3}$$

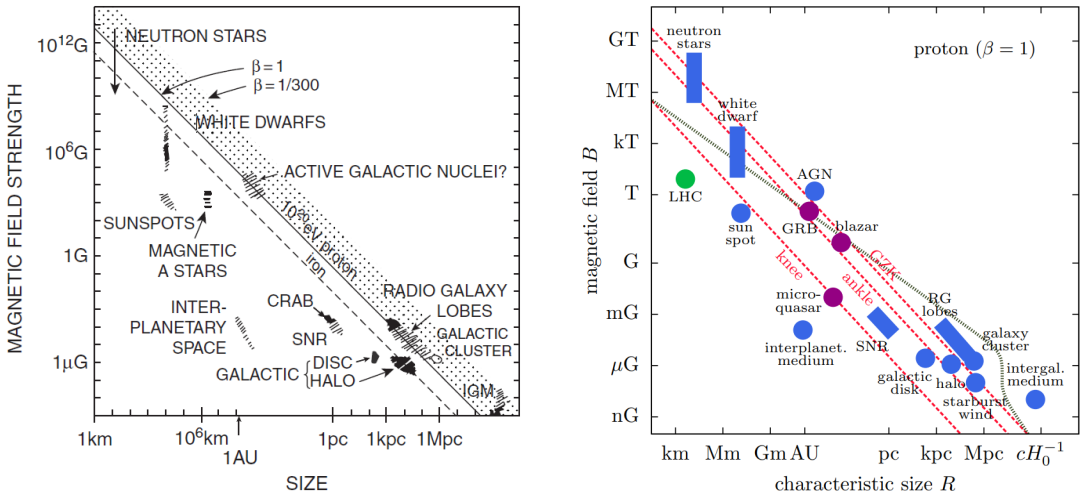

Figure 3: Left: Original Hillas plot from [3]. Right: Modern adaption of Hillas plot from [6] with upper limits on cosmic ray energies to the knee, the ankle and the GZK cutoff. These energy regions will be looked at in Section 2.3.

The lines in Figure 3 represent the energy limits that cosmic rays can reach, derived from E_{max}. Due to their high B and R values, some objects (like Neutron stars or active galactic nuclei, AGN) are able to accelerate particles to ultra-high energies up to 10^{20} eV if the Hillas condition is fulfilled [6, 3]. However, it is difficult to theoretically develop and describe acceleration scenarios in detail because they rely on the knowledge of the source's characteristics like the magnetic field and size. The theories of possible cosmic ray sources require further inspections and experimental confirmations. On all accounts, the search for the cosmic rays' origin will greatly benefit from increasing precision measurements of the energy spectrum, especially in the high energy regions [4, 3].

2.3. Energy spectrum

As seen in the previous Section, the energy of a cosmic ray particle is directly impacted by its source and acceleration process. Therefore, the energy spectrum is the most powerful tool for the study of cosmic rays. Thanks to increasing precision in experimental measurements, more details of the energy distribution, especially the behavior of its spectral index, was revealed.
The observed energy reaches from 10^9 eV (see Figure 5) to a few 10^{20} eV (see Figure 4). The energy spectrum for all primary particles measured by different cosmic-ray experiments is shown in Figure 4, giving the flux F (the number of particles per unit area, time, and solid angle) as a function of the energy-per-nucleus E. The flux was multiplied by $E^{2.6}$ to make the characteristic changes in the slope more obvious. Those changes are the steepening around 10^{16} eV (called the knee), another steepening at about 10^{17} eV (called the second knee), the flattening at about $10^{18.5}$ eV (called the ankle), and another flattening ankle-like behavior between the first and second knee [7, 5].
At energies of a few 10^{20} eV, the particle flux is greatly suppressed. The reason for this suppression is not certain yet. The Hillas plot would suggest the cut-off coming from reaching the maximal energy possible in the source's acceleration process. Another explanation could be the energy loss of cosmic rays through the GZK effect, which was independently calculated by Greisen, Zatsepin and Kuzmin (GZK). This effect describes the interaction of particles with the photons of the cosmic microwave background (CMB). In case of very high energetic protons traversing the CMB, the interaction with the CMB photons would lead to pion production and the proton energy would be limited to the energy threshold for pion production at about 6×10^{19} eV. Experimental results from the Pierre Auger Observatory do not agree with the assumption of the GZK cut-off being the dominant effect, while the results from the Telescope Array don't rule out this assumption. The experimental results can be seen in Figure 4. So, at this point of time, one can conclude that the GZK effect might be only one contributing factor to the energy cut-off [5].
The appearances of the spectral breaks before the cut-off have also not been fully understood, yet. The most common interpretations of the knee, second knee and ankle structures in the energy spectrum are the following: The cause for the knee is supposed to be either a change in the propagation process, or reaching the maximum energy of the Galactic source. In case

of SNR as main Galactic source, the latter would again be derived from the Equation (2) for the maximum energy. Even though E_{max} for SNR seems to be below the PeV region, where the knee occurs, the scenario of magnetic field amplification within the SNR (as mentioned in Section 2.2) could lead to the acceleration of cosmic rays even into the PeV region. In the same way, the former interpretation of the knee implies the source to be able to accelerate cosmic rays up to energies of a few PeV. However, the current knowledge of Galactic objects makes it questionable if Galactic sources can achieve this kind of acceleration [5].

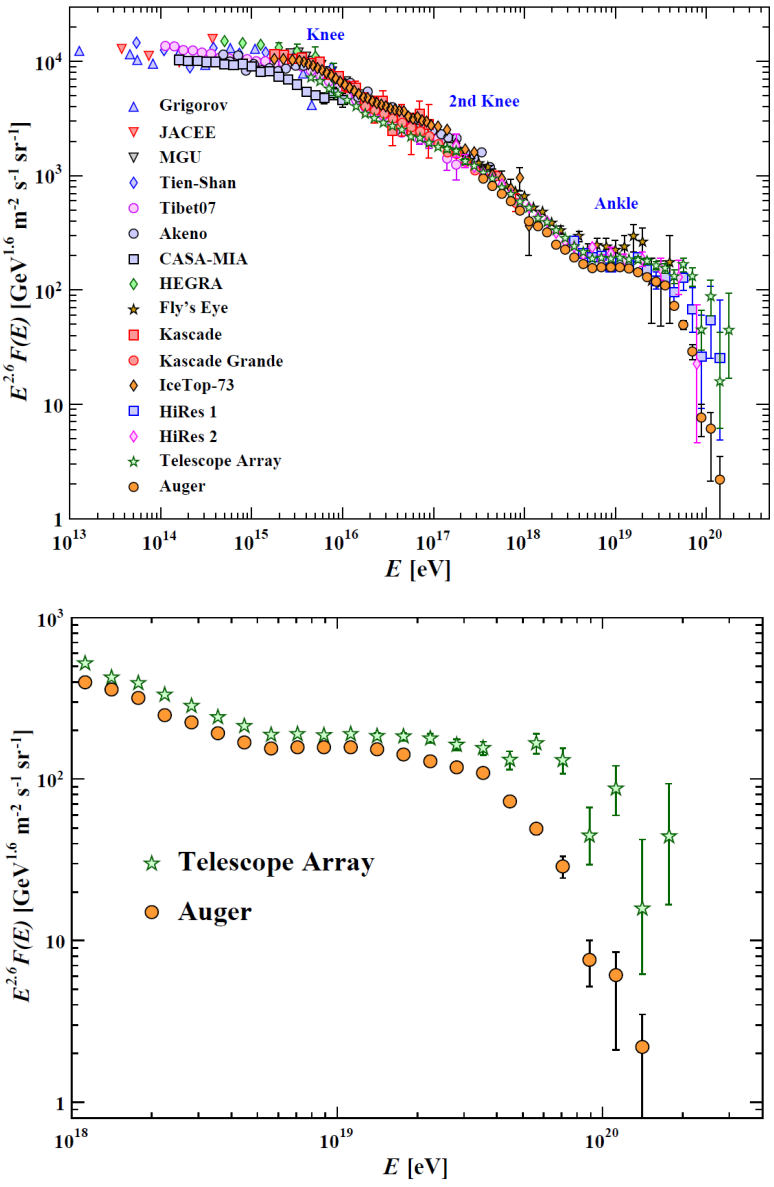

Figure 4: On the top is the all-particle energy spectrum, observed by 16 different experiments. On the bottom is the all-particle spectrum for energies between 10^{18} eV to several 10^{20} eV, only showing the measurement results from Telescope Array and Pierre Auger experiments [7].

While it is assumed that the knee is mostly composed of protons, the second knee is believed to be dominated by iron nuclei depending on rigidity and therefore also referred to as iron knee. If this is true, the physical explanation for the second knee would be the same as for the knee [5].
There is experimental evidence for the suggestion that the ankle indicates the transition from galactic to extragalactic sources. It was found that the mass composition becomes lighter around and after the second knee. This observation indicates the arrival of light particles from places of origin different to the origin responsible for the particles in the lower energy region. Another clue is the anisotropic direction of arrival which was discovered at large scales at energies beyond the ankle: The cosmic-ray flux was found to be higher in regions on the sky map which do not point to Galactic but rather extragalactic sources. The cosmic-ray anisotropy itself is a huge subject of discussion and investigation in the physics' world and relies on more precise measurements of the astrophysical sky to be explored in more depth. For more details on the experimental results and interpretation concerning the energy spectrum, see Refs. [5, 7].

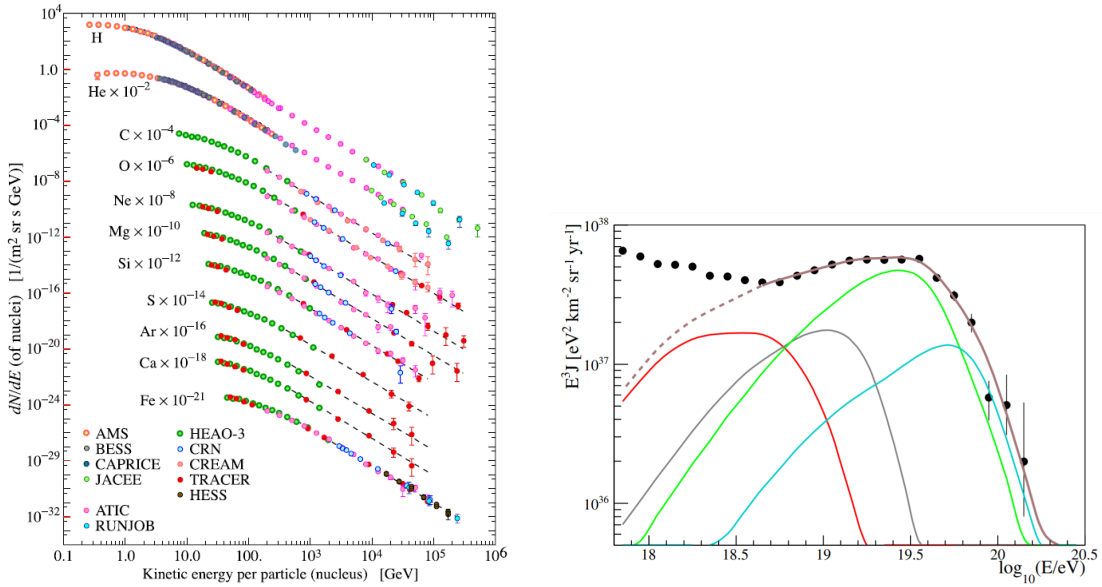

Figure 5: Left: Fluxes of primary CR nuclei as a function of the energy per nucleus. Comparison of experimental results of different experiments [7]. Right: All-particle energy spectrum measured by the Pierre Auger Observatory (black dots) and fitted (brown line), and partial spectra of the 4 mass groups H (red), He (grey), CNO (green) and Si (blue), simulated with CORSIKA [8].

While the plots in Figure 4 present the all-particle energy spectrum, the left plot of Figure 5 shows the 1-component-spectra of some specific primary particles, measured by experiments with direct detection methods on balloons or satellite in space (see Section 2.4). The particle flux decreases with the mass of the particle. Yet, the different fluxes show

approximately the same energy dependence which indicates the same origin and acceleration mechanism, respectively, for all shown particles in this specific energy range. For higher energies, 1-component-spectra are not available due to the indirect detection method, as mentioned in Section 2.2. Instead, one can calculate the spectra of predefined mass groups which are H (A = 1), He ($2 \leq A \leq 4$), CNO ($5 \leq A \leq 22$), Si ($23 \leq A \leq 38$), Fe ($39 \leq A \leq 56$), with the mass number A. For each mass group, the energy spectra and other parameters can be simulated and compared with the experimental results. As an example, the right plot of Figure 5 shows results of the measurement by the Pierre Auger Observatory and simulated mass group spectra calculated with the program CORSIKA [9, 8]. Thus, the type and setup of an experiment predefine what kind of information can be gained about cosmic rays. This is what the next Section is about.

2.4. Experimental methods

Since the discovery of cosmic rays, many experiments have been developed and performed for either the direct or indirect detection of cosmic rays. The detection method depends on, amongst other things, the mass and energy of the cosmic ray particle and therefore also on the particle flux. If the flux is high enough, primary particles can directly be measured with instruments attached to balloons or satellites. The indirect detection is done by ground-based experiments through the detection of air showers initiated by primary particles. Below, I will shortly describe one balloon-borne, one space-based and one ground-based experiment to give an example of how the experimental detection methods work.

Figure 6: Launch of the Super-TIGER balloon on the 8^{th} December 2012 in Antarctica [10].

A direct detection of cosmic rays is possible for particles with energies below 10^{14} eV because their particle flux is large enough to be detected by relatively small detectors. The experimental instruments are carried as payload by either super pressure balloons, which can fly up to altitudes of 36 km, or satellites at the International Space Station (ISS). In all

cases, the cosmic rays can be detected before they interact with molecules of the Earth's atmosphere. In general, balloon-borne or space-based experiments use a combination of different detection techniques in order to obtain the charge, energy and mass of the incident cosmic ray particle. That includes solid-state detectors for particle tracking, scintillators to determine the charge and Cherenkov detectors and calorimeters for energy determination [9, 11].

One of the most recent cosmic-ray balloon measurements was done with the Super-TIGER experiment which is an upgrade of the TIGER (Trans-Iron Galactic Element Recorder) experiment. The photograph in Figure 6 shows the Super-TIGER balloon during its launch. Both experiments, TIGER and Super-TIGER, were used to measure the abundance of ultra-heavy galactic cosmic-ray nuclei, that are nuclei heavier than iron. They undertook so-called long duration balloon (LDB) flights which means that their balloons were flying for several days up to several weeks. Super-TIGER has set a new record for the longest LDB flight in 2012/2013 with a flight over a period of 55 days. It also flew for 32 days in 2019/2020. The full Super-TIGER payload weights 1770 kg and consists of plastic scintillators for charge determination, hodoscope detectors for trajectory determination and two types of Cherenkov counters to obtain the particles velocity. In this way, Super-TIGER gained, amongst others, the abundances of the galactic cosmic-ray nuclei from Zinc to Zirconium with very high statistics. The experimental results are consistent with the assumption that OB associations (loose groups of O-type and B-type stars) could be one origin of galactic cosmic rays. More details can be found in Refs. [12, 13, 14, 15, 11].

The CALET (CALorimetric Electron Telescope) experiment belongs to the space-based cosmic-ray experiments, deployed at the ISS and in operation since 2015. Its goals are, on the one hand, the precise measurements of the electron and positron spectra which might hint at possible astrophysical sources of high-energetic cosmic rays, and on the other hand measurements of heavy and ultra-heavy cosmic-ray nuclei with energies up to 10^{12} eV. This is achieved by using a calorimeter to obtain the identity and energy of the detected cosmic-ray particle. The calorimeter consists of a charge detector for charge determination, an imaging calorimeter and a total absorption calorimeter for particle tracking and energy determination. After about three years of data taking, CALET obtained a high-precision energy spectrum for cosmic-ray electrons and positrons in the range from 10^{10} to 10^{12} eV, which shows some differences to the spectra measured by other experiments like DAMPE or Fermi-LAT (see Ref. [16] for the comparison details). The differences might be a consequence of unknown systematic effects and are still under investigation. CALET continues to take data with the goal to increase statistics and decrease systematic errors [16, 17].

Comparing the results of different experiments is an important procedure to not only critically interpret the outcome of data analysis of one single experiment, but also to complement the findings and conclusions in the field of interest. After all, each experiment is unique and has got its specific sensitivity in certain physical areas. As shown above, experiments like CALET, (Super-)TIGER and ACE-CRIS [12] are designed in a way to effi-

ciently study heavy cosmic-ray nuclei which are rare compared to the lighter nuclei (mainly cosmic-ray protons and helium nuclei). The light component of cosmic rays was, and still is, precisely measured in experiments like CREAM [18], PAMELA [19] or AMS [20].

As can be seen in the energy spectra in Figure 4 and 5, the particle fluxes decrease with increasing particle's energy. From a certain energy region (approximately from the PeV region) onwards, the particles can't be observed directly anymore, or if they would, then the statistics would be too low due to the current state of technology. For this reason, the detection of high- and ultra-high-energetic cosmic ray particles are observed with ground-based experiments only. The larger the detector, the higher-energetic particles can be studied. As mentioned above, cosmic ray particles initiate extensive air showers of secondary particles as they enter and interact with the molecules of the Earth's atmosphere. In Chapter 3, I will have a closer look at the physics of extensive air showers. The secondary particles of extensive air showers can either be detected with large detector arrays on the ground, or their light emission through interaction with atmospheric molecules can be observed with telescopes, likewise set up on the ground. Using both techniques simultaneously is called "hybrid" detection [9], which is illustrated in Figure 7.

To give a current example of such a hybrid experiment, the Telescope Array (TA) will be shortly presented. The TA experiment is set up in Utah, USA, and has been operated since 2008. It pursues the goal of measuring cosmic rays with ultra-high energies above 10^{18} eV. The experiment consists of two types of detectors: plastic scintillation detectors and fluorescence telescopes. The 507 scintillator surface detectors, positioned in an approx. 700 km^2 large array, measure the charged secondary particles of extensive air showers, which cause the scintillating molecules inside the detector to get excited and emit ultraviolet light that is detected within the detector. Combining the signals of all the scintillator detectors gives the particle densities as well as the time and direction of arrival of the observed extensive air shower. Together with the 3 fluorescence telescope stations, each including 12 to 14 telescopes, the energy, direction of arrival and identity of the primary particle can be gained. Those telescopes basically consist of a large spherical mirror, which reflects fluorescence light[1] onto a camera made of PMTs (photomultiplier tubes). Observing this fluorescence light with telescopes from two sites simultaneously makes it possible to reconstruct the air shower direction. However, the telescopes can only take data on clear moonless nights [22, 23, 24].
Since April 2019, additional 257 surface detectors have been deployed and operated which belong to a newly developed array called TAx4. TAx4 is an upgrade to the TA experiment with the goal to more efficiently (and faster) study cosmic rays with energies above 57 EeV. Additionally, two more fluorescence telescope stations are planned and designed [22].

[1]Fluorescence light is emitted when charged secondary particles in an air shower ionize and excite molecules in the atmosphere, and the excitation results in the emission of visible or ultra-violet light [21].

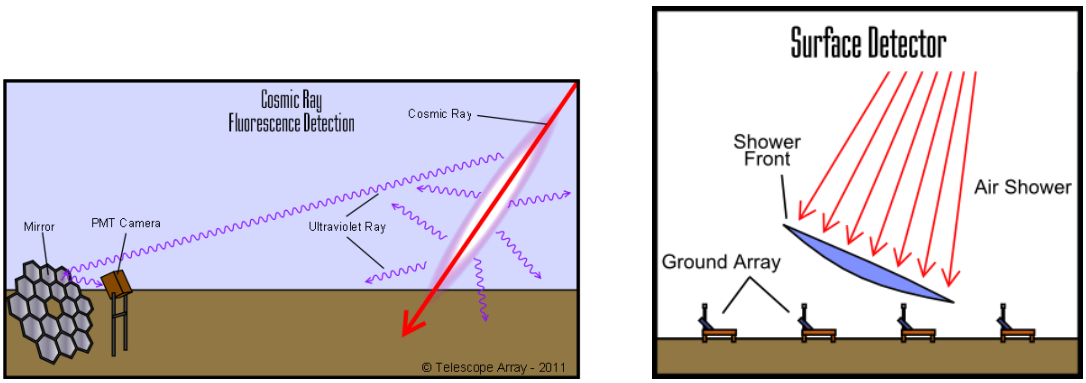

Figure 7: Hybrid detectors using telescopes and detector arrays. Left: Schematic of detection of scintillation ("fluorescence") light emitted by a cosmic-ray initiated air shower, using a fluorescence telescope [25]. Right: Schematic of the detection of charged secondary particles with the surface array [26].

After several years of operation, the TA experiment published a number of interesting results in its cosmic ray studies. One of them is the observation of a hotspot on the sky map where a cluster of events with energies above 57 EeV appears ("event" stands for one detected air shower which was generated by a cosmic ray). The cause for this hotspot, which might hint to yet unknown cosmic ray sources, is not clear and requires more statistical data for better interpretation. The hotspot is one of many reported indications of anisotropy in the cosmic ray sky. Another observation of this anisotropy is that a dependence on the declination[2] band was found for the break point in the energy spectrum. More details about the measured energy spectrum of the TA experiment can be seen in Refs. [27, 22, 28].
The TA experiment and the Pierre Auger Observatory, which also observed hotspots in the sky map, are the largest air shower detectors built to this day and have been able to detect primary cosmic rays at ultra-high energies above 10^{18} eV up to the energy cut-off at a few 10^{20} eV. Other ground-based experiments like the HAWC Observatory (using water Cherenkov detectors [29]), the Tibet hybrid experiment (operating two air-shower arrays [30]) or the KASCADE(-Grande) experiment (using a field array, central detector and muon tracking detector [31]), to only name three, cover the energy spectrum from 10^{12} eV to a few 10^{18} eV.
The IceTop array (air shower surface array of the IceCube observatory, described in more detail in Chapter 4) is using ice Cherenkov tanks (a planned enhancement will add a scintillator and radio detector array to the experimental setup [32]) in order to measure the energy spectrum in the region of about 100 TeV to 1 EeV [33]. This region connects the results of direct and indirect measurements and is plotted in Figure 8 with experimental results from several experiments.

[2] "declination" is a certain angle in the equatorial coordinate system

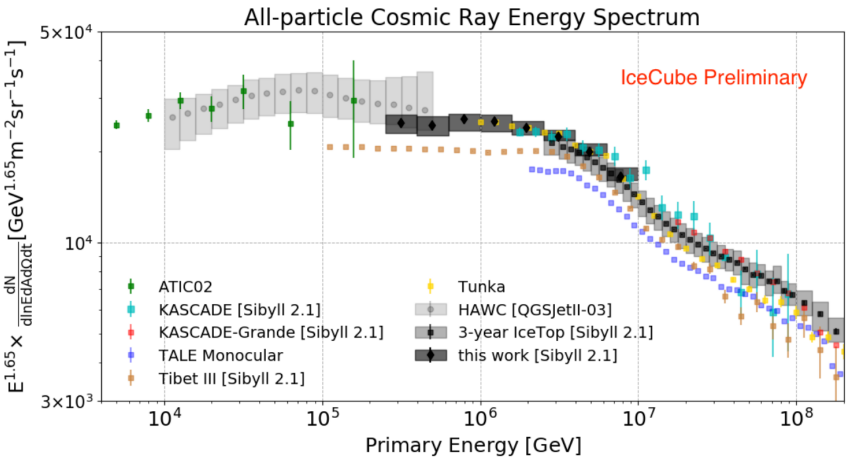

Figure 8: Comparison of all-particle spectra measured by IceTop 2016 and other experiments. The result from "this work" represents the analysis done in [34].

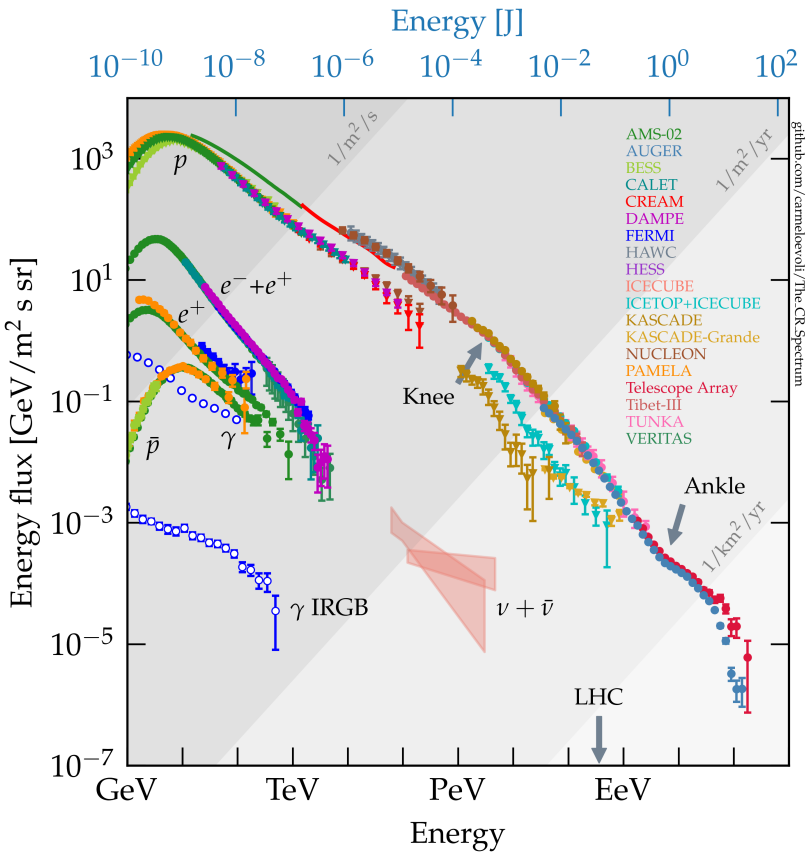

Figure 9: Compilation of the cosmic-ray energy spectrum measured by several experiments after 2000. Results from γ-ray and neutrino measurements are also included [35].

Looking at Figure 9, which shows all-particle energy spectra but also spectra for a few certain primaries measured by a range of different experiments, one can notice some differences between the experiments. This might be due, among other things, to the fact that the experiments do not all use the same analytical parameters or hadronic interaction model, which the data simulation and therefore the air shower reconstruction are depending on. Yet, in the all-particle spectrum the majority of experiments seem to be in agreement with each other.

To draw a conclusion on the topic of experimental methods, the diversity of experimental approaches has advanced the study of cosmic rays a great deal. On the way to find answers to the general questions about the cosmic ray's origin, mass composition and acceleration mechanism, many interesting observations have been made concerning the anisotropy on the cosmic ray sky, the detailed investigation of the energy spectrum and elemental abundances. But many new and more specific questions accompany the complex results of high-precision measurements [5]. New experiments and upgrades of existing experiments, along with continual improvement of simulation programs and theoretical concepts and models, give hope for more statistics and lower systematic uncertainties, and will sooner or later lead to the confirmation, adjustment, or rejection of theories about the cosmic-ray sources, acceleration and propagation mechanism.
Regarding the air shower experiment IceTop, one attempt to improve its cosmic-ray studies, in particular the mass composition studies, is to modify the way of gaining information about single muons in detected air showers from experimental data. This can be done by investigating signals from single muons, the so-called SLC charge signals, which so far have not been included in the standard data analysis at IceTop. As will be explained in the following chapter, muons produced in air showers hold information about the mass of the primary particle initiating the shower. The efficient use of SLC signals is still under investigation, but it shows great promise to advance IceTop's mass composition analysis. Therefore, this thesis focuses on the study of general features of those SLC charge signals in order to provide a basis for studies of the muon content in extensive air showers measured at IceTop.

3. Extensive Air Showers

Cosmic rays with energies higher than 10^{15} eV can only be detected indirectly because of their low flux of one particle per square meter per year. The indirect detection is based on the detection of extensive air showers generated by cosmic ray particles in the Earth's atmosphere. In this Section, the development and main features of extensive air showers will be described.

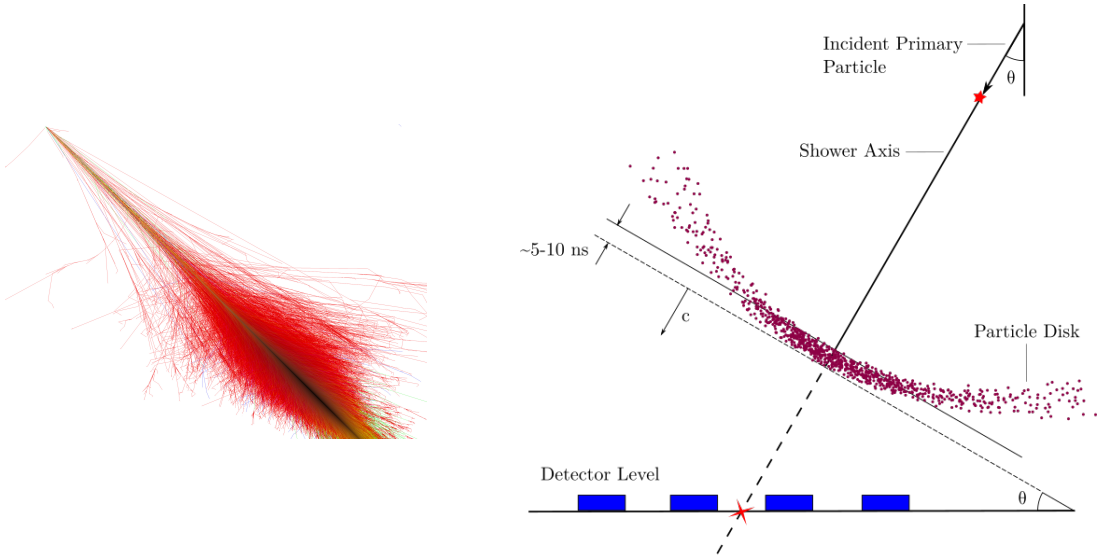

Figure 10: Left: Simulation of a 10^{15} eV - proton induced extensive air shower (red = e^+, e^-, γ, green = μ, blue = hadrons) [36]. Right: Schematic of geometrical parameters of an extensive air shower [37].

The starting point of an air shower is the point of interaction between the incident primary particle, being a hadron, and a nucleus in the atmosphere at heights typically above 15 km. This high-energetic hadronic interaction, which is explained in detail in Ref. [38], produces new hadrons and other particles. A lot of those particles again interact with atmospheric particles and thereby create a shower of secondary particles. A simulation of an extensive air shower is shown in Figure 10 to the left, some of its geometrical parameters are shown in the same figure to the right. The shower axis denotes the general direction of the air shower propagation. The angle between the shower axis and the vertical z-axis is called zenith angle θ. After a short time of propagation through the atmosphere, a particle disk (often approached as plane wave) reaches the Earth's surface and can be measured by surface or underground particle detectors.

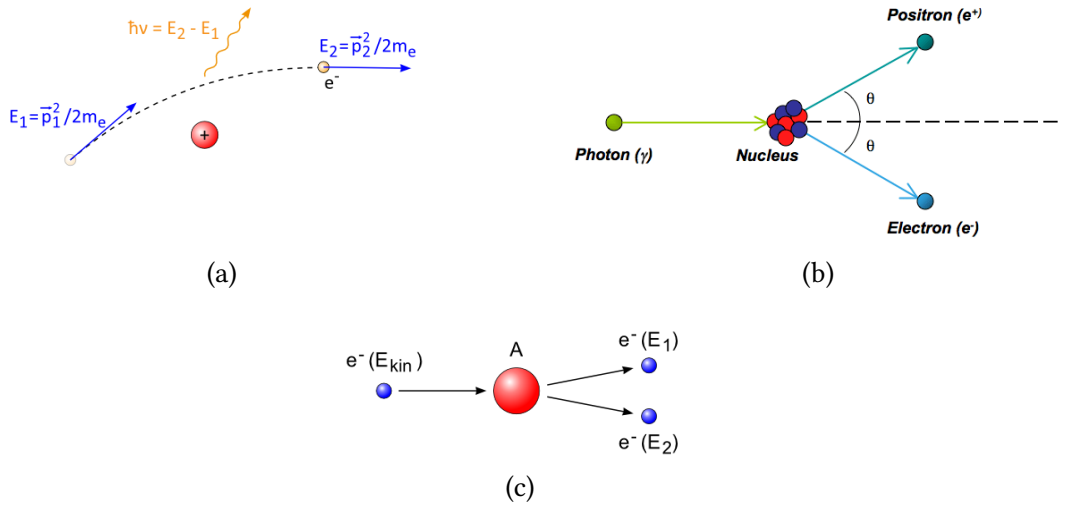

Figure 11: Interactions of the electromagnetic component:
(a) Bremsstrahlung: An electron/ positron loses energy through photon emission during its deflection in the nucleus' magnetic field [39].
(b) Pair production: In the magnetic field of a nucleus, a photon creates an electron-positron pair [40].
(c) Ionization: A high-energetic electron collides with a nucleus A so that it emits an electron and becomes an ion A^+ [41].

Not only the properties of the primary particle, but also the behavior of the secondary particles determine how the air shower will develop. The ensemble of particle interactions with matter, energy losses and scattering processes will lead to an air shower with a certain size N, lateral and longitudinal particle distribution, a specific particle composition, and other air-shower specific characteristics. So, in order to gain useful information from air showers, one has to understand and study those particle processes in detail. Here, I will only give a short summary of the main processes.
Depending on the identity and energy of the secondary particle, it either interacts with other particles with a possible production of more particles, or it decays, or it reaches the Earth's surface. As the secondary particles become less and less energetic with each interaction step, particle production can only happen down to a certain stage of air shower evolvement until the energy threshold for particle decay is reached. Thus, during the development of the air shower, the number of particles N (referred to as shower size) increases up to a maximum at a specific slant depth X, from where it decreases again due to the processes of decay and absorption. X is the depth of the shower in the atmosphere, measured from the top of the atmosphere downward, in the direction of the air shower axis. Other particle processes that affect the air shower development are energy losses through bremsstrahlung, ionization, and pair production. Those processes are illustrated in Figure 11. The lateral distribution of the air shower is a result of two processes. First, electrons and positrons in the shower can undergo elastic Coulomb interactions (deflection in the electromagnetic field of a nucleus) by which they are scattered at small angles. Second, the lateral distribution of secondary

hadrons at large angles comes from their transverse momentum which they gain during their production. As described on the next page, muons mainly stem from hadrons, do not undergo further interactions and are therefore spread wider than electromagnetic particles.

The shower size N is an important characteristic of an air shower to be calculated and studied because of its dependence on the primary's energy E_0. An approximate relation between E_0 and the slant depth X_{max} , at which the maximum shower size occurs, can be described with the Heitler model and the Heitler-Matthews model and is expressed in a simple way with Equation (4) (for a hadron-induced air shower) [38]:

$$X_{max}(E_0) \approx \lambda_{hi} + X_0 \ln\left(\frac{E_0}{2n_{tot}E_c}\right). \tag{4}$$

n_{tot} gives the number of particles produced through the interaction of a hadron. λ_{hi} is the hadronic interaction length, that is the particle's mean free path between two hadronic interactions. X_0 is the radiation length in air, meaning the mean distance that the particle (usually electrons and photons from the electromagnetic sub-shower) travelled through air before losing energy by bremsstrahlung in case of electrons, or by e^+e^- - pair production in case of photons. E_c is the critical energy at which bremsstrahlung and ionization will make up for the same amount of energy loss.
Technically, it is not possible to directly measure the shower size. However, two experimental methods have been developed with the goal to reconstruct the shower size as precise as possible. One method is to observe the air shower during its propagation in the atmosphere before the particle disk hits the ground. This can be achieved by measuring the light emission of the secondary particles with fluorescence and Cherenkov telescopes. Another experimental procedure is based on measuring the lateral distribution of the particles reaching the detector. These lateral distributions are like the footprint of the air shower because they are strongly depending on the shower size and therefore on the primary's energy. A combination of both experimental methods is favorable but not necessary. Detailed simulations of air showers and the detector responses are necessary for the analysis of experimental data. One can compare the reconstructed parameters from experimental data with the simulated air shower parameters, and thereby obtain the properties of the primary particle. For this purpose, it is important to know about the type of particles that form the air shower and are reconstructed in the experiment. An air shower consists of three components: The hadronic, electromagnetic and muonic component, as illustrated in Figure 12. The hadronic component includes protons, neutrons, kaons and pions. Neutral pions π^0 immediately decay into two photons and thereby contribute to the electromagnetic sub-shower (see Equ. (5)). Charged pions $\pi^{\pm}$, having reached the energy threshold for decay, feed the muonic component through the decay in Equation (6).

$$\pi^0 \longrightarrow \gamma + \gamma \tag{5}$$

$$\pi^{\pm} \longrightarrow \mu^{\pm} + \overset{(-)}{\nu}_{\mu} \tag{6}$$

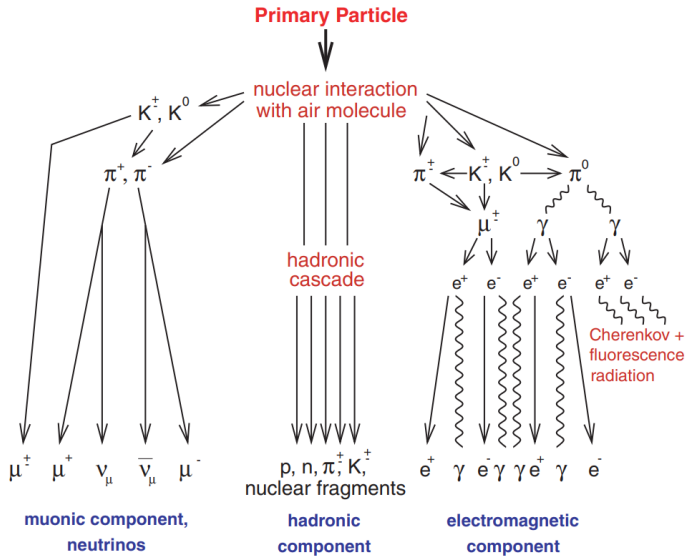

Figure 12: Components of an extensive air shower on the ground level [42].

Also, the decay of kaons K produces more muons and neutrinos as well as pions. The decay processes into muons are the ones on equation (7) and (8):

$$K^{\pm} \longrightarrow \mu^{\pm} + \overset{(-)}{\nu}_{\mu} , \tag{7}$$

$$K^{0}_{L} \longrightarrow \pi^{\pm} + \mu_{\pm} + \overset{(-)}{\nu}_{\mu} . \tag{8}$$

90% of the muons in an air shower are originating from the decay of mesons. Muons have a relative long mean lifetime of 2.197 μs [43] and a small cross-section, so they are unlikely to interact before reaching the ground. However, for low-energy muons a decay into neutrinos is possible. Hence, high-energetic muons are measured in abundance at ground level. So, the number of muons at the shower maximum is approximately the same as at ground, $N_{\mu} \approx N_{\mu,\max}$.
Neutrinos, being quite stable and hardly ever interacting particles, will travel through the atmosphere basically unhindered. They are usually the last type of particle to be detected in an air shower experiment, often in an underground detector to shield the muonic component.
The electromagnetic component contains electrons, positrons and photons which are mainly the products of pair production by photons emitted in the π_0 – decay, and bremsstrahlung (see Figure 11). Most of the shower energy will be transferred to the electromagnetic component and from there to the atmosphere due to ionizing electrons (see Figure 11).

The zenith angle of the air shower influences the particle composition on the ground level. With increasing zenith angle the distance that the air shower propagates through the atmosphere becomes larger. The larger the distance, the more particles will decay or get

absorbed, so that less and less of the hadronic and electromagnetic component make it to the ground. The result is that for very large zenith angles, only muons and the electromagnetic particles from the muonic decay reach the ground and can be detected. This is one reason why muons play an important role in the study and detection of extensive air showers. Another reason is their dependence on the primary's mass. While the number of electrons at the shower maximum $N_{e,max}$ depends on the primary energy (E_0) and is approximately the same for a light and a heavy primary particle (see Equation (9), [38]), the number of muons N_μ depends on the primary energy as well as the mass A (see Equation (10), [38]).

$$N_{e,max}^{proton}(E_0) \approx N_{e,max}^{A}(E_0) \tag{9}$$

$$N_\mu^A(E_0) \approx A^{1-\alpha} \times N_\mu^{proton}(E_0), \qquad \text{with} \quad \alpha = \frac{\ln(n_{ch})}{\ln(n_{tot})} \tag{10}$$

These relations were calculated under the assumption of the superposition model which treats a nucleus with mass A the same way as A independent nucleons (protons and neutrons).
In Equation (10), n_{tot} is the total number of particles and n_{ch} the number of charged particles produced in the interaction of one hadron. It was found that α has a value in the range of 0.82 to 0.94 [38] depending on the primary energy, on the mean threshold of the hadronic interaction and also on the level of observation. Therefore, the factor $A^{1-\alpha}$ is always greater than 1. So, from Equation (10) one can predict the muon number initiated by heavy primaries to be larger than the muon number produced by light primaries at the same energy. Likewise, the depth of the shower maximum X_{max} depends on the mass of the primary particle: For light primaries like protons, the shower maximum occurs deeper in the atmosphere than for heavy primaries like iron nuclei with the same energy [38].
Hence, studying the number of muons in an air shower as well as the ratio of electron and muon numbers at ground level provides very useful information about the mass composition of the incident primary particle.

4. IceCube and IceTop

The analysis in this thesis was performed using data from the IceTop air-shower array which is a part of the IceCube experiment. In this chapter, IceCube will be shortly introduced, yet the focus lies on the experimental setup and data acquisition of IceTop. The last Section explains the way of simulating IceTop data, which is a crucial part of IceTop analysis.

4.1. IceCube

The IceCube Neutrino Observatory [44] is stationed at the geographic South Pole and is an in-ice neutrino telescope with multiple purposes. It can indirectly detect astrophysical neutrinos with energies between 100 TeV and 10 PeV. That makes one of its scientific goals the precision measurements of neutrinos and neutrino oscillations, as well as the search for sterile neutrinos. Other goals are the search for Dark Matter and the studies of cosmic rays. IceCube also takes part in a multimessenger program in collaboration with other observatories.

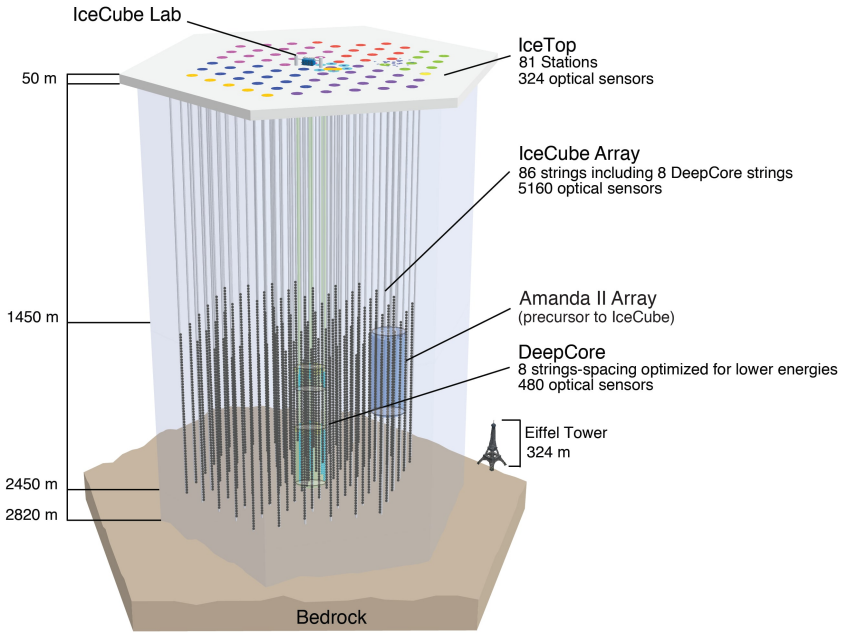

Figure 13: IceCube detector with components DeepCore and IceTop in the final configuration (December 2010) [45].

IceCube is a 1 km³ big detector whose deployment took seven years from 2004 until 2011. The experimental setup is shown in Figure 13. The 86 strings are vertically deployed under the surface in the clear ice of the Antarctic. Each string is approximately 2500 m long and holds 60 DOMs. DOM stands for Digital Optical Module and will be looked at in Section 4.2.1. Each DOM contains a photomultiplier tube for the detection of Cherenkov light produced by high-energetic charged particles, and the associated electronics. The detected light is digitized and sent to the IceCube Lab. There are 8 strings (called the DeepCore) in the center of the string array which are closer to each other than the rest of the strings. The IceTop array is placed exactly on top of the string configuration [45, 44].
IceCube's method to detect particles is based on the detection of Cherenkov light. Figure 14 shows a simple illustration of the Cherenkov effect. Cherenkov light is emitted by a charged particle which travels faster than light through a certain medium, e.g. clear ice in case of IceCube. The charged particle excites the water molecules which return to their ground state by emitting light in form of spherical electromagnetic waves. If the charged particle is faster than those emitted photons, the wavefronts interfere constructively and create the Cherenkov light which moves as a cone in the direction of the charged particle. In case of IceCube, the charged particles are the product of the interaction of Neutrinos with the Antarctic ice. The Cherenkov radiation of those secondary particles spreads through the Antarctic ice and gets detected by a certain amount of DOMs. The radiation is proportional to the particles' track length but not dependent on its identity. Therefore, the identity of the charged particle emitting the Cherenkov light can't be determined directly by the light signal. Yet, the pattern of the DOMs reveals the direction of the secondary particle and thereby the position of the neutrino interaction which can be used for neutrino astronomy. Figure 15 illustrates such a neutrino event measured with the DOMs on IceCube's strings [44].

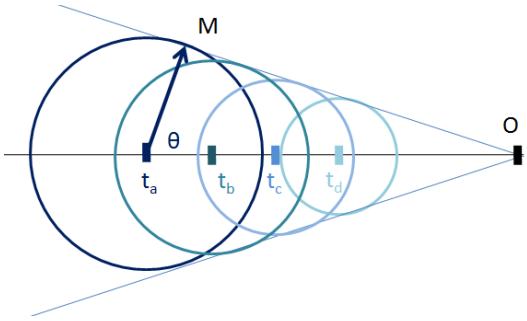

Figure 14: Scheme of a particle (traveling from the left to the right of the picture) emitting Cherenkov light at angle θ [46].

One of IceCube's scientific successes was the detection of the, up to this point of time, two highest neutrino events observed in the year 2011 and 2012. Those famous neutrino events, called Ernie and Bert, are shown in Figure 16. Similar to the illustration in Figure 15, the balls represent the DOMs which detected the Cherenkov light of the same event. The bigger the ball, the more light was measured in the DOM. The color corresponds to the time of the light arrival with blue for early and red for later hits.

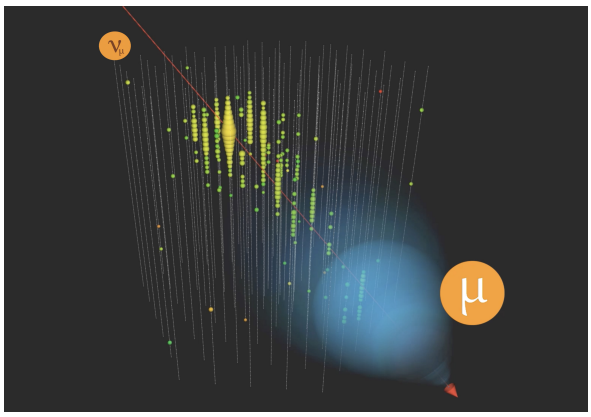

Figure 15: Illustration of a muon neutrino event detected by the IceCube DOMs. A muon from the neutrino interaction emits Cherenkov light (blue) and leaves a trace in the string array. The colorful balls represent the DOMs which detected the Cherenkov light from this particular event. The color scheme shows the response time, the ball size is increasing according to the amount of observed light [47].

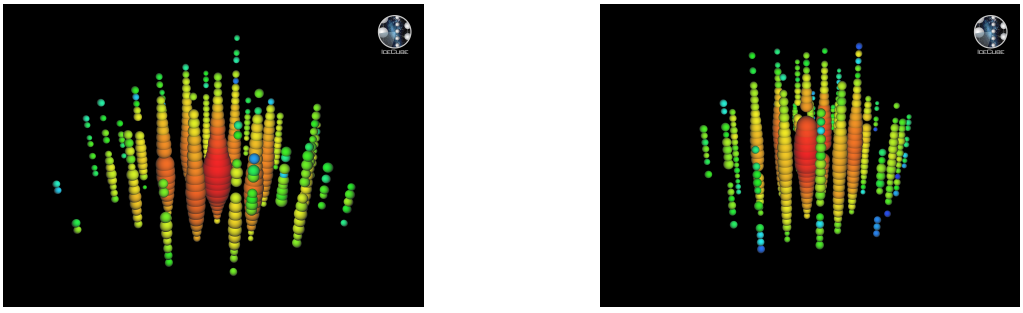

Figure 16: Two neutrino events observed by IceCube which proofed the existence of astrophysical neutrinos. Left: Neutrino event, called Ernie, detected on 3rd January 2012 by IceCube, estimated energy of 1.14 PeV. Right: Second neutrino event, called Bert, detected on the 9th August 2011 by IceCube, estimated energy of 1.04 PeV [48].

4.2. IceTop

The deployment of the IceTop surface array at an altitude of 2835 m started a short time before IceCube's deployment, with a small test setup. The whole surface array was then completed in 2011.
IceTop's scientific goal is to study cosmic rays, mainly their mass composition and origin. IceTop detects extensive air showers produced by cosmic rays with energies between 300 TeV and 1 EeV. Hence, it is sensitive to particles in the range between the knee and the ankle of the cosmic ray energy spectrum. In this energy region it is assumed that the transition from galactic to extragalactic cosmic rays takes place. IceTop is able to measure the shower

core position, direction and shower size and, by comparing those parameters with simulated air showers, obtain the cosmic ray energy spectrum.
IceTop is also used as a veto detector for IceCube when the muons from cosmic-ray air showers are treated as background in IceCube's measurements. Another possibility of combining the in-ice and the surface component of IceCube is the coincident analysis of air shower events, with muons observed in the ice and electromagnetic particles detected by IceTop. This analysis method makes it possible to obtain the cosmic ray composition as well as the energy spectrum and is described in [49]. The analysis of this thesis, however, concentrates only on IceTop events.
The method of particle detection is the same as in IceCube: IceTop uses DOMs installed in ice-filled tanks to measure the Cherenkov light emitted by secondary particles from air showers which traverse the tank with a velocity higher than the speed of light. More details on the signal capture and processing will be given in Section 4.2.2 [45].

4.2.1. Experimental setup

The IceTop surface array consists of 81 stations with each station instrumenting two ice-Cherenkov tanks, called A and B. A scheme of the 1 km² large tank array is given in Figure 17 to the left.

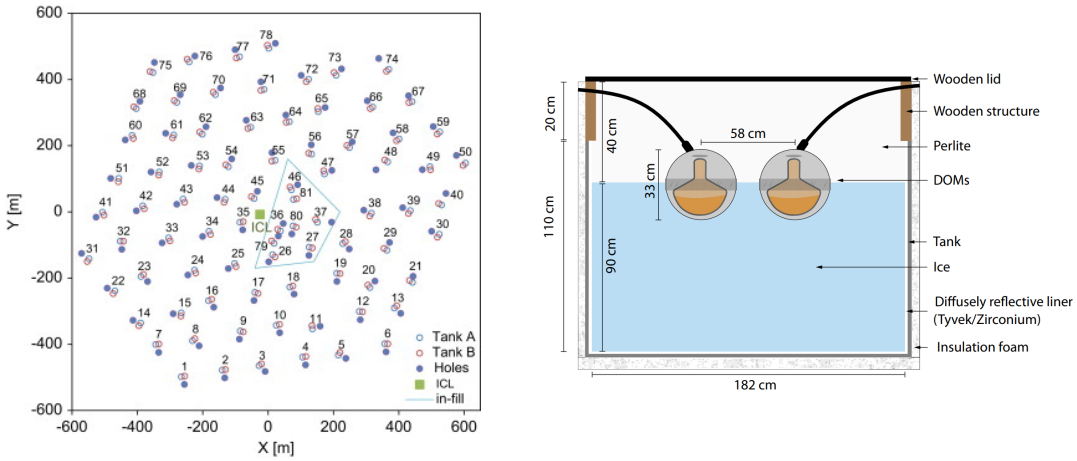

Figure 17: Left: Location of the IceCube strings and IceTop tanks. The IceCube Lab ICL (green square) lies in the middle of the configuration. In the in-fill area (blue line) the tanks have a shorter distance to each other. Right: Cross section of an IceTop tank [45].

The stations are arranged on the triangular grid approx. 125 m apart and thereby they are located very close to the drilling holes of the IceCube strings, except for the stations of the in-fill. The tanks of one station stand 10 m apart, they are cylindrical and featured with a high reflectivity layer on the inside. They are 130 cm high and filled with transparent ice up to 90 cm in which two DOMs are frozen. The photomultiplier tubes (PMTs) inside the DOMs are facing down, as illustrated in Figure 17 to the right. The DOMs inside a tank

and the neighboring tank of the same station are connected to cables via a so-called surface junction box. They are also connected to a cable that sends the digitized signals to the IceCube Lab for further signal processing [45].
To avoid snow drifting and temperature fluctuations (although the seasonal temperature changes can't be fully avoided), the tanks are embedded into the snow. Snow accumulates at a different rate over each IceTop tank at an average of 20 cm per year, which decreases the expected electromagnetic signals. This effect is usually taken into account in any kind of data analysis, for each tank individually [45].
A scheme of a DOM is shown in Figure 18. A DOM is a glass pressure sphere that includes the PMT, a mu-metal grid to shield the PMT from the magnetic field of the Earth, an LED Flasher Board for calibration purposes, and the mainboard of the DOM. The two DOMs inside one tank are operated with a high gain (HG) and a low gain (LG) on the PMT. This increases the dynamic range of the tank, meaning it will be able to detect particles with a wider range of energy. This is necessary for the detection of air showers because the energy of the secondary particles can differ immensely [45].

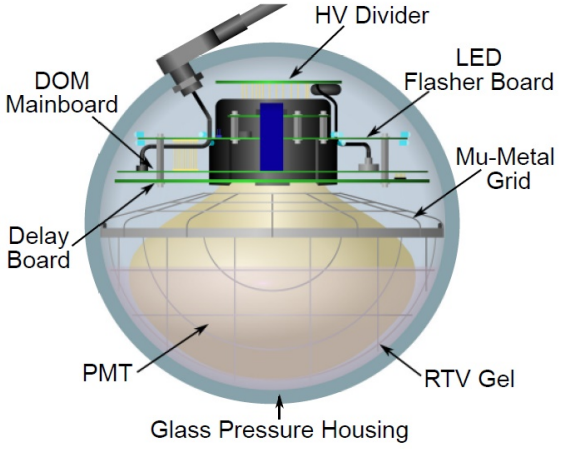

Figure 18: Scheme of an IceTop/IceCube DOM [45]

All the important electronics needed for the operation are built on the mainboard of each DOM. The operations include the communication with the IceCube Lab, setting triggers, capturing and digitizing signals. This is done with the help of an FPGA (Field Programmable Gate Array). Depending on the trigger, the FPGA hinders or allows the recording of captured signals. The way of signal capturing with IceTop DOMs is described in the next Section. Signals are sent to the IceCube Lab via computers called DOMHub. Each DOMHub is connected to 8 IceTop stations. The DOMs transfer their collected signals in regular intervals to the DOMHub where they get time-stamped and sorted for each hit [45].
When passing a trigger for a defined readout time window, the signals are processed further in the IceCube Lab. There, they are either used for calibration and monitoring of the DOMs and tanks, or they are combined with signals from other DOMs to reconstruct air shower events.

Filter algorithms help to select the physically most interesting events which are then sent immediately to other IceTop offices via satellite. All events are stored on tapes. More details on the trigger system of IceTop are given in Section 4.2.4 [45].

4.2.2. Signal capture and processing

This Section will give a short general overview of the signal capture and processing done at IceTop. The arrow diagram in Figure 19 serves as implementation for the understanding of the steps from signal creation to signal capture and transfer at IceTop: Starting point is the arrival of a cosmic-ray particle in the atmosphere where it interacts with atmospheric molecules and thereby creates secondary particles. Further particle interactions lead to the development of an extensive air shower. Some of the secondary particles, mainly muons, electrons and photons, are produced late enough or are persistent enough to reach the Earth's ground.
If one of those particles carries electrical charge and propagates through an IceTop tank it generates Cherenkov radiation, according to the process described in Section 4.1. The photons of the Cherenkov light are reflected inside the tank and eventually hit the PMTs of the two tank DOMs. Having entered the PMT through the light input window, the photons reach a photocathode which releases electrons as a result of the photoelectric effect in vacuum (photons hitting a metal or semiconductor which then emit electrons). Those electrons, also called photoelectrons, are accelerated towards the PMT's electron multiplier because of its applied voltage.
The electron multiplier consists of a certain number of dynodes which emit secondary electrons as they get hit by the photoelectrons. In that way, the electrical current is increased and the light signal amplified. The high-gain DOMs are nominally set to a gain of 5×10^6, while the low-gain DOMs are set to a gain of 10^5. After hitting the last dynode, the current of photoelectrons and secondary electrons reaches the PMT's anode where it initiates an electrical pulse [50, 45].
From this point on the front-end electronics on the DOM mainboard will determine the readout and further proceedings with the measured signal. First, a transformer decouples the signal from the anode's high voltage. Then it is split into three paths. One path digitizes the signal continuously with a fast Analog to Digital Converter (fADC) but those signals have not yet been useful for analysis in IceTop. The second path sends the signal to the discriminator trigger which will cause the DOM launch, i.e. sampling of the signal on the third path, if the discriminator threshold is passed. The discriminator threshold is lower for a low-gain DOM than for a high-gain DOM. The third path is split again into three differently amplified signal paths which are all connected to two Analog Transient Waveform Digitizers (ATWDs) with a built-in delay of 75 ns to give the second path time for a trigger decision. The amplification factors are 16 for the first ATWD input channel, 2 for the second input channel and 0.25 for the third input channel. Two ATWDs are used in turn to decrease the dead-time of the DOM. If the PMT signal passes the discriminator threshold on the second path, the FPGA allows the signal recording for one of the two ATWDs. That means, the ATWD samples the incoming signal of the three input channels

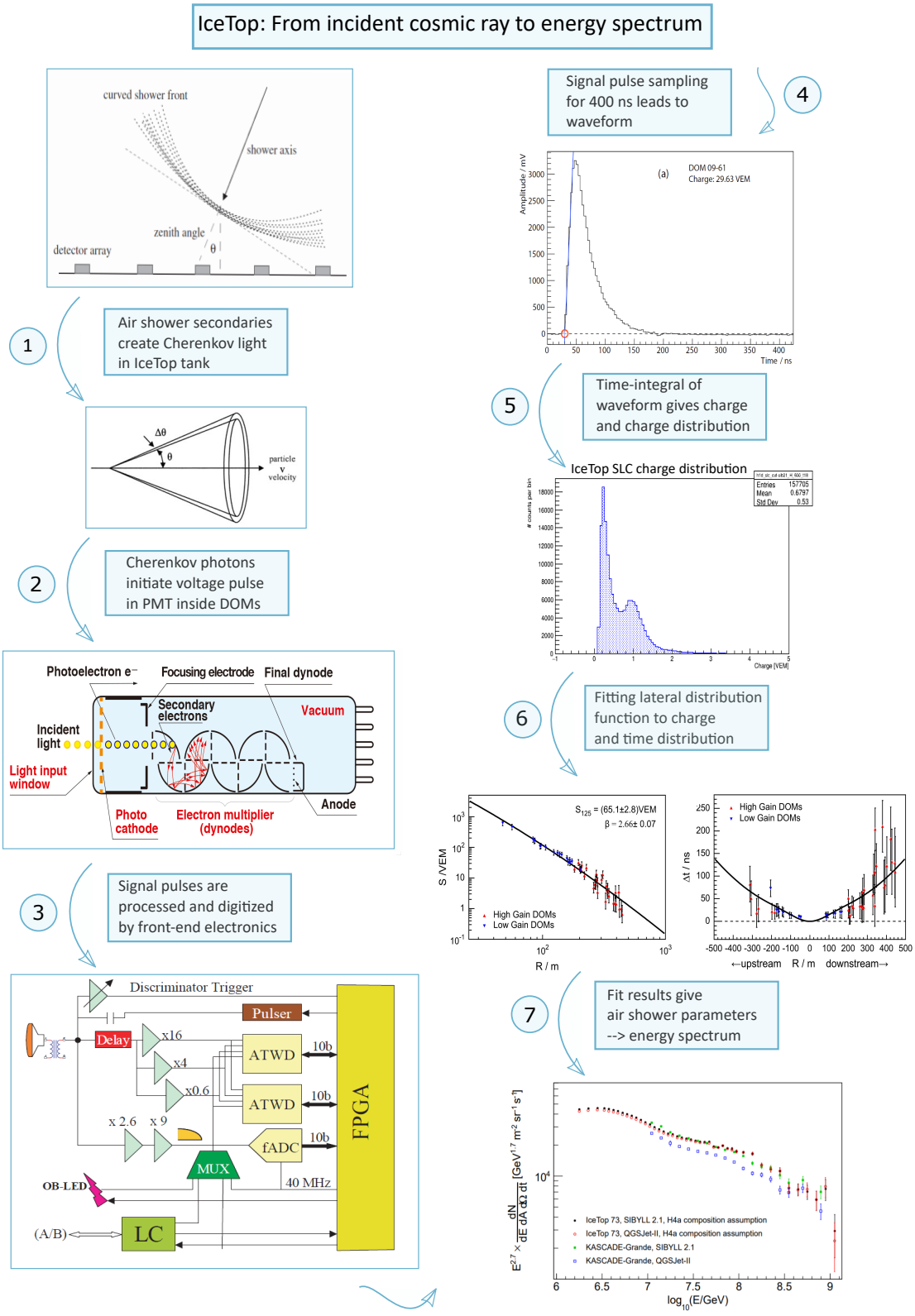

Figure 19: The diagram shows a simplified path of signal capture and data analysis in IceTop.

synchronously in 3.33 ns wide bins. This signal sampling is done for about 427 ns for each input channel which will result in three waveforms with each 128 bins. These analog waveforms, holding information about the amount of voltage created at the PMT's anode over time, are then digitized with 128 Wilkinson ADCs[3]. The digitization starts with the waveform of the highest gain channel and only continues with a lower gain channel if the highest gain channel includes values above a certain threshold which is determined during calibration measurements.
A launched DOM transfers its collected data to the IceCube Lab under specific circumstances, depending on the mode that IceTop is operated in. IceTop's operation modes are explained in Section 4.2.3. In the standard mode (HLC mode) the whole digitized waveform is transferred along with a time stamp. In case of SLC mode, an average ADC calibration of the bins 5 to 60 instead of the whole waveform is sent to the Lab. There, the waveform (or the ADC bins) undergoes some corrections that include the starting time and the droop affected by the transformer decoupling the PMT signal from the high voltage. Then, the corrected waveform is integrated over time to obtain the signal charge S. The shape of the waveform is mainly affected by the shape and reflectivity of the tank and the readout electronics.
A waveform can be interpreted as a superposition of pulses generated by a single muon. To be able to compare the waveforms of different tanks, the signal charges are normalized and expressed in the unit Vertical Equivalent Muon (VEM). This is done in monthly calibration measurements for each DOM with vertical muons hitting the tank. More details about IceTop's calibration procedures can be found in Ref. [45].
The signal charges and times of several DOM hits result in charge and time distributions which can be analyzed. The charges from one single DOM can be used for calibration. For the purpose of air shower reconstruction, a trigger system is used to combine the measured charges of all the IceTop stations associated with the same air shower event. The triggers that are commonly used in IceTop's search for cosmic ray air showers are described in Section 4.2.4.
After combining IceTop stations to an air shower event, the main properties of the observed air shower can be reconstructed from the charge and time distribution. The shower size, S_{ref}, can be obtained by fitting a lateral distribution function to the charge signal distribution. The fit result gives the shower size $S_{ref} = S_{125}$ (the charge signal at a lateral distance of 125 m from the shower axis) and a free parameter β which corresponds to the slope of the fitting graph. S_{125} was specifically chosen for IceTop to be referred to as shower size because at the lateral distance of 125 m the correlation of S_{ref} and β is minimal and the shower size at 125 m is not as mass-dependent as at other distances. As mentioned in Section 3, the primary energy can't be directly derived from the shower size S_{125} because the energy is also related to the primary mass and the zenith angle. Thus, detailed simulations are necessary to gain the primary energy from the measured value for S_{125}. Regarding the fit on the measured time distribution, the shower front can be reconstructed and thereby also the position of

[3]In a Wilkinson ADC, whose process runs linear and therefore more accurate compared to a successive approximation ADC, the analog input signal charges a capacitor which discharges again at a certain constant rate. During the discharge, an oscillator creates pulses at a fixed frequency. The number of pulses is proportional to the input signal [51].

the shower core (x_c, y_c) along with time t_0 at which the shower core reached the ground. In addition, the shower direction defined by the zenith angle θ (in the vertical) and azimuth angle ϕ (in the horizontal) can be determined. In Section 4.2.5 the IceTop reconstruction method is further explained. The reconstructed parameters depend on the primary energy and mass in different ways and have to be compared with the parameters from simulated air showers. This can be performed by either the use of neural network mapping or by two-dimensional unfolding algorithms.
The comparison of experimental data with simulated data yields the expected properties of the primary particle. The experimental results are summarized in a cosmic ray energy spectrum, shown in Figure 4 in Chapter 2 [45].

4.2.3. Detection modes

There are two possible operation modes which are based on the so-called Local Coincidence (LC) condition. A DOM will be tagged with "LC" if one or two other DOMs within the same station are launched in a time window of 1 µs. To achieve the immediate comparison of DOM responses, all the four DOMs within one station are interconnected via cables which sends logical signals as soon as one high-gain DOM is launched. The interconnection is shown in Figure 20.

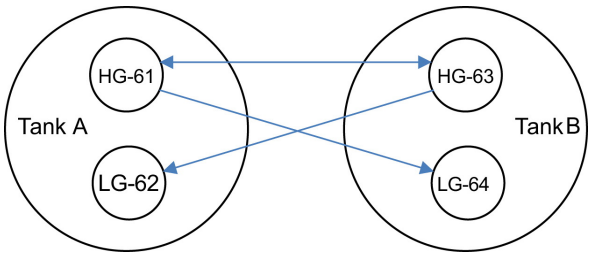

Figure 20: Scheme of the interconnection of the DOMs of one IceTop station for the achievement of a local coincidence. HG = High-gain DOM, LG = Low-gain DOM [45].

If one high-gain DOM is launched because the discriminator threshold was passed, a signal sent to the DOMs of the other tank sets a time window of 1 µs. If in that time window the other high-gain DOM launches (and maybe additionally the low-gain DOM), then all launched DOMs will be read out and tagged with "LC". In case there is no other launched DOM in that time window, the first launched DOM discards its signal and gets back to the ready state.

The standard operation mode of IceTop is the so-called Hard Local Coincidence (HLC) mode. In this mode, the LC condition needs to be fulfilled in order to read out the DOM signals. As mentioned in Section 3.2.2, the HLC signals (or also called HLC hits) include the full digitized waveform information.

The other available operation mode is the Soft Local Coincidence (SLC) mode. If IceTop is running in this mode, there is no LC tag necessary for a launched DOM to transfer data to the IceCube Lab. That means, that every launched DOM will be read out. However, instead of the full waveform only the integrated charge and the timestamp are read out.

The HLC mode was chosen to be the standard mode because it reduces the capture of background signals from single particles. Yet, looking at the lateral distribution of particle densities of the air showers' secondary particles, as plotted in Figure 21, the LC condition can only be fulfilled in dense regions around the shower core. With increasing distance to the shower core, the densities become smaller and the probability of a hard local coincidence decreases. So, one would expect the majority of HLC signals to be gained close to the shower core, while SLC signals would be also expected much further away from the core. This difference in operation mode plays an important role in the studies of muons.

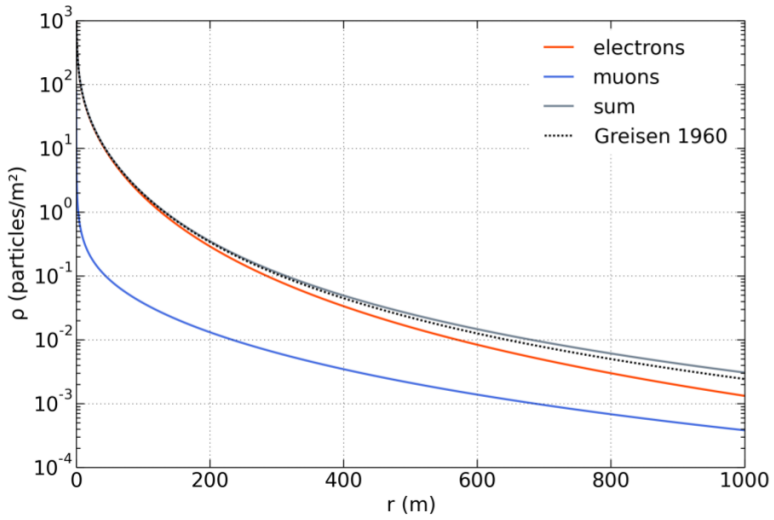

Figure 21: Lateral distribution functions for muons, electrons and their sum, which is equivalent to the classic Greisen curve calculated by K. Greisen [52]. The functions are IceTop specific for an altitude of 2835 m and an air shower with an energy of 300 TeV [53].

Muons, having a wider lateral distribution than the electromagnetic air shower component, occur as single muons at small and large lateral distances. So, the electromagnetic component is dominant in the region close to the shower core, while the muonic component becomes more and more significant further away from the shower core. HLC operated stations are more likely to miss those single muons because the detection of a single muon would need to coincide with that of another particle in the same station, in order to generate a local coincidence. Of course, this coincidence of a muon and another particle is less probable than to detect a single muon in the SLC mode. Having in mind that muons give valuable information about the primary particle initiating the air shower, mainly its mass composition as shown in Equation (10) of Chapter 3, one can conclude that it is of high

interest to include SLC charge signals into IceTops' composition studies. For this reason, SLC signals hold the potential to help differentiate between electromagnetic and muonic signal detected in the tanks and thereby contribute to reveal the mass of the primary particle. This subject will be further discussed in Chapter 5.
SLC signals have been and still are investigated, using different approaches in order to find a way to properly and effectively include them in analytical procedures. To give an example, one approach which is currently studied [54] is to look at the possibility of defining a muon-based mass sensitive parameter which can be applied individually to each detected air shower event with the goal to categorize the primary particles of those showers into different mass groups (from light to heavy). Such a categorization is already done in simulations, but it entails systematic errors from the choice of hadronic interaction models when simulating the initiation and development of the extensive air shower. Therefore, the use of such a mass sensitive parameter would reduce the systematic effects stemming from simulations. For more details on this study see Ref. [54].

4.2.4. Triggers

In this Section, the standard triggers used in IceTop measurements are listed and briefly explained. A trigger system is important for the experiment to find the physically interesting events. A trigger helps to get rid of background events which in case of IceTop are low-energetic air showers and random hits in IceTop [45].

- **Discriminator trigger**: It sets a voltage threshold that the PMT signal pulse needs to pass in order to launch the DOM and start the waveform capture. Each DOM can choose between a SPE (single-photoelectron) and MPE (multiple-photoelectron) discriminator which set the threshold to either about 4 mV (signal charge of approx. 270 PE) or about 20 mV (signal charge of approx. 23 PE), respectively. For air shower detection, the MPE discriminator is used in high-gain DOMs, while the low-gain DOMs operate the SPE discriminator.

- **IceTopSMT** (Simple Multiplicity Trigger): As soon as 6 HLC hits are recorded within 6 µs, the whole IceTop array is read out. The readout happens from 10 µs before the first HLC hit until 10 µs after the 6th HLC hit.

- **IceTopMinBias**: A minimum bias trigger reduces the number of launching HLC hits to a prescale factor of 10^4, which means that only every 10^4th HLC hit passing the discriminator threshold will trigger the IceTopSMT.

- **IceTop Online filter**: A set of triggers used to reduce the data for satellite transmission. The requirement for the filtered data is the passing of the IceTopSMT trigger.
  - **IceTopSTA3**: Only air shower events which triggered at least three stations are transferred via satellite. This leads to an energy threshold of 300 TeV for the primary particle.

  - **IceTopSTA5**: After an event has passed the IceTopSTA3 trigger, this trigger requires 5 or more stations to be hit.
  - **IceTop_InFill_STA3**: After an event has passed the IceTopSTA3 trigger, this trigger requires 3 or more stations of the infill area to be hit. This leads to a lower energy threshold of 100 TeV.
  - **InIceSMT_IceTopCoin**: Without the requirement of the IceTopSMT trigger, this trigger aims to select events which coincide with in-ice events. The trigger requires the in-ice simple multiplicity trigger to be passed and at least one HLC hit in IceTop. The selected events can be used as a veto for high-energetic cosmic ray induced air showers. Additionally, they can be used for tests and calibration of the entire IceCube detector.

- **Local Coincidence**: A local coincidence occurs when two DOMs from two tanks of the same IceTop station are launched within a time window of 1 µs. Then, both (sometimes even three) DOMs receive a "LC" tag. Reading out only LC tagged DOMs, as it is done in HLC mode, reduces the amount of data and background events.

- **Software triggers**: They are used to decide from the IceTop DOM launches collected at the IceCube Lab, if the whole IceCube detector should be read out.

4.2.5. Cleaning and reconstruction

Before events undergo the air shower reconstruction procedure, their tank information has to be cleaned. The cleaning process is necessary because there might be tanks with a missing triggered tank partner which need to be found and removed from the tank selection for shower reconstruction. In the experiment, there are certain technical circumstances where a DOM is not ready to trigger and therefore might miss to capture a signal. These circumstances are not simulated, so that simulated events don't have to be cleaned.
There are two cleaning conditions that a tank needs to pass to survive the cleaning process. First, the signal of tank A in one station should not follow longer than 200 ns after the signal of the other tank B in the same station:

$$|t_A - t_B| < \frac{|\mathbf{x}_A - \mathbf{x}_B|}{c} + 200\text{ns} \, . \tag{11}$$

Second, the group of stations are regarded as belonging to the same air shower event, if their signal times are all not separated for more than 200 ns. This condition needs to be fulfilled for any station i in comparison to station j, as presented by:

$$|t_i - t_j| < \frac{|\mathbf{x}_i - \mathbf{x}_j|}{c} + 200\text{ns} \, . \tag{12}$$

In Equation (11) and (12), $t_{A/B}$ is the signal time in tank A/B, and $t_{i/j}$ is the average time of the signals in both tanks A and B of the one station i/j. $\mathbf{x}_{A/B}$ is the position of tank A and B respectively, and $\mathbf{x}_{i/j}$ is the position of the station i and station j, respectively. The cleaned

events can then be reconstructed [45].
For the air shower reconstruction IceTop is using *Laputop*, a software tool based on the maximum likelihood method. As already mentioned in Section 4.2.2, the charge and time distribution, containing all the tank signals (also from untriggered tanks) from one air shower event, are fitted with a charge lateral distribution function (LDF) as:

$$S(r) = S_{125} \times \left(\frac{r}{125\text{m}}\right)^{-\beta-\kappa \log_{10}(\frac{r}{125\text{m}})} . \tag{13}$$

The fit procedure includes fluctuations of the signal size and the times of arrival, as well as signal corrections due to snow on top of the tanks which is given in Equation (16). The charge LDF in Equation (13) gives the charge expectation value as a function of the lateral distance r. Free parameters are the shower size S_{125}, the slope β, and the curvature κ for a logarithmic formula of Equation (13) at a reference distance of r = 125 m. According to simulation studies the value of κ does not change significantly for different hadronic air showers. Therefore, a constant value of $\kappa = 0.303$ is used [45].
The signal time of a tank is parametrized as:

$$t(\mathbf{x}) = t_0 + \frac{1}{c}(\mathbf{x} - \mathbf{x}_c)\mathbf{n} + \Delta t(r) , \tag{14}$$

$$\Delta t(r) = ar^2 + b\left(1 - \exp\left(\frac{-r^2}{2\sigma^2}\right)\right) . \tag{15}$$

In Equation (14), the free parameters of the time are t_0, $\mathbf{x}_c$ and $\mathbf{n}$. t_0 is the time of arrival of the air shower at ground (the average altitude of the IceTop tanks), and $\mathbf{x}_c$ is the two-dimensional shower core position. $\mathbf{n}$ is the unit vector which points in the direction of the shower propagation. The shape of the curved shower front $\Delta t(r)$ is described by Equation (15). The constants a, b and σ have fixed values as presented in [45].
The fitting procedure of the functions in Eqs. (13), (14) and (15) starts with a first-guess to seed in the likelihood fit. After this first estimate of parameters, the fit with the likelihood function is minimized by several iteration steps. During those steps, certain parameters are held fixed while other parameters are changed until an improvement of the fit occurs.
The snow correction as formulated in Equation (16) is done for each tank i in each iteration step:

$$S_i^{corr} = S_i \times \exp\left(\frac{-h_s^i}{\lambda_s \cos(\theta)}\right) . \tag{16}$$

S_i represents the expected signal value in tank i (derived from the charge LDF) and S_i^{corr} is the snow-corrected value of S_i. The snow height on top of tank i is given by h_s^i, and λ_s corresponds to an effective absorption length of electromagnetic particles, which should be about 2.1 m in snow. The snow height is measured on each tank once a year. θ is the zenith angle of the measured air shower [45].

After the completion of the likelihood fitting procedure in Laputop, the reconstruction results and other important measured data are collected and saved in an IceTop specific

file type, the so-called i3 file. The best-fit results are stored in a structure which is called *I3Particle*, in the rubric *Laputop*. Other fit parameters (e.g. errors of the signal location x and y, fit parameter chi2, etc.) are stored in the same i3 file in a rubric called *Params*. The measured signal charges HLC and SLC and the applied analytical cuts are also saved within this i3 file. Here, there exist several charge rubrics which differ in their state of cleaning. The analytical cuts, called the Quality Cuts, will be further described in Section 4.1.
The simulated parameters are stored in an i3 file as well, with additional information about the true physical values which were used for the simulation. The simulated I3Particle contains e.g. the true energy and mass of the primary particle which are of course not known yet for the experimental I3Particle.

4.3. Monte-Carlo simulation

As described in Section 4.2.2, IceTop as any other air shower experiment relies on detailed simulation data in order to retrieve the relevant air shower parameters to describe experimental data. The simulation of data is performed in two steps: First, the air shower needs to be simulated which builds on the choice of a hadronic interaction model. This matter is subject of Section 4.3.1. Second, the simulated secondaries are fed in the simulation of the detector response. This is described in Section 4.3.2.

4.3.1. Air shower simulation with CORSIKA

IceTop uses the program CORSIKA (COsmic Ray SImulations for KAscade) [55] to simulate extensive air showers through Monte-Carlo calculations. CORSIKA was developed for the purpose of studying air showers initiated by high-energetic cosmic rays and photons (originally for the KASCADE experiment in Karlsruhe). Figure 22 gives an example of how simulated air showers with CORSIKA look like. The simulation of air showers does not only aim to calculate the mean values of the interesting shower characteristics like shower size, particle densities or lateral and longitudinal distributions. But fluctuations and correlations of those parameters are also determined.
When running the program CORSIKA, the first thing to do is choosing the starting parameters which include basically the primary particle type, primary energy, angle of incidence and atmospheric parameters. From here, the initiated air shower is calculated.
Many factors contribute to the evolvement of an air shower, so in detailed simulations all those factors are considered and described as realistically as possible. The first contributing factor is the environment to which belongs the atmosphere and the magnetic field of the Earth. It's assumed that the atmosphere consists of 78.1% N_2 (Nitrogen), 21.0% O_2 (Oxygen) and 0.9% Ar (Argon). There are 7 sets of different atmospheres available, in each set one can choose a certain range of altitude and atmospheric densities for which seasonal changes have been taken into account. The magnetic field influences the track of charged particles due to their deflection in the field [55].

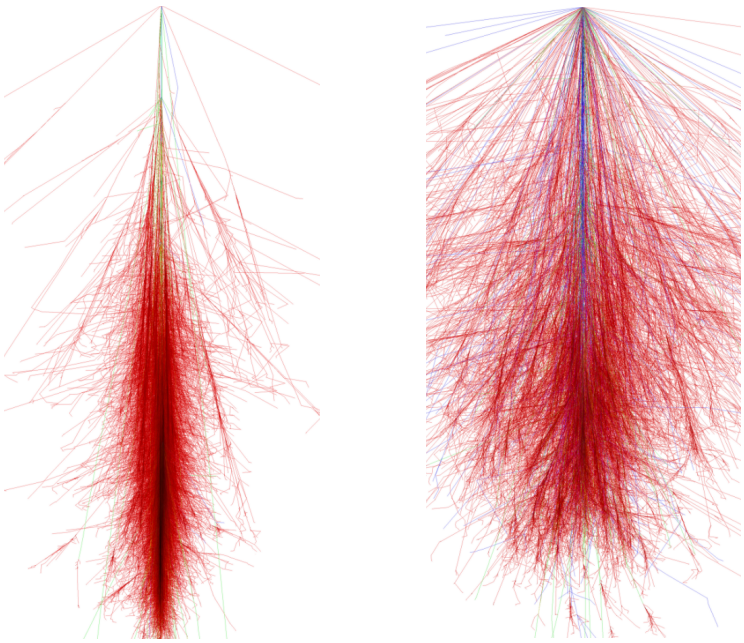

Figure 22: xz-projection of air showers simulated with CORSIKA for primary particles with energy of 1 TeV. Left: Proton induced shower. Right: Iron induced shower. Red lines show the tracks of electrons, positrons and photons. Green lines correspond to muon tracks. Blue lines illustrate the tracks of hadrons [56].

As mentioned in Chapter 3, the trajectories and decay or production of particles depend on certain particle processes listed below which have certain probabilities. Probabilities are handled in CORSIKA by using a Monte-Carlo random number generator which generate 10 independent sequences of uniformly distributed numbers between 0 and 1, with approx. 10^{44} numbers per sequence.

- Ionization energy loss: (see Figure 11 in Chapter 3) a charged particle traversing through matter is losing energy by ionizing an atom. This process is taken into account for all charged particles.
- Coulomb multiple scattering: a charged particle deflects in the electric field of a nucleus. The change of propagation direction without energy loss can happen multiple times. In CORSIKA, this process is only applied on muons.
- Deflection in Earth's magnetic field: A charged particle deflects in the magnetic field of the Earth without energy loss. This is applied to every charged particle in CORSIKA.

Additionally, two important features need to be considered which are the inelastic cross section and the lifetime of a particle: Both features determine how long a particle can travel before it either interacts inelastically with another particle or it decays. The cross sections for inelastic interactions of nuclei, nucleons, pions and kaons (CORSIKA does not

include inelastic hadronic interaction of muons) with air are parametrized differently in each hadronic interaction model, yet they all increase with higher particle mass and energy. The interaction length λ_{int}, meaning the free path between two inelastic interactions, for the above-mentioned particle types is given by Equation (17), with $m_{\text{air}} = 14.54$ g/mol the average atomic weight of air and σ_{air} the cross section for the given inelastic interaction:

$$\lambda_{\text{int}} = m_{\text{air}}/\sigma_{\text{air}} \ . \tag{17}$$

σ_{air} is the cross section of a shower particle with air, more specific the two different cross sections are defined as shown in Equation (18) and (19):

$$\sigma_{\text{n-air}} = \sum_{i=1}^{3} n_i \sigma_{\text{n-N}_i} \quad , \qquad \text{for nucleon n} - \text{air interaction,} \tag{18}$$

$$\sigma_{\text{N-air}} = \sum_{i=1}^{3} n_i \sigma_{\text{N-N}_i} \quad , \qquad \text{for nucleus N} - \text{nucleus interaction.} \tag{19}$$

Here, N_i is the i component of air (N_2, O_2 and Ar) and n_i is the atomic fraction of component i which are $n_1(N_2) = 0.781$, $n_2(O_2) = 0.21$, and $n_3(\text{Ar}) = 0.09$.
Nuclei and nucleons are considered as stable, so that no lifetime or decay process is needed, as opposed to muons. For muons only bremsstrahlung and e^+e^- - pair production are taken as possible muonic interactions. Therefore, in Equation (17) for muons the cross section σ_{air} is replaced by σ_{int} the cross section for the mentioned two processes. In case of decay, the mean free path l_D of a muon is given by:

$$l_D = c \times \tau_\mu \times \gamma_\mu \times \beta_\mu \ . \tag{20}$$

c is the vacuum speed of light, τ_μ is the lifetime of a muon at rest, γ_μ is the Lorentz factor, and β_μ the muons velocity. Equation (20) is applied to pions and kaons also, of course with replacing the lifetime τ_μ with the pion's or kaon's lifetime. Equation (17) is also used for pions and kaons with the corresponding inelastic meson-air interaction cross sections.

Neutrinos are regarded as stable particles and thus do not interact or decay at all.

In CORSIKA, every particle is time tracked and the current energy and position are updated frequently.

The hadronic interactions can be modelled differentially regarding the energy and many other parameters. The variety of theoretical models results from the difficulty of investigating those interactions at collider experiments. Most of the particles produced in hadronic interactions at colliders which carry most of the collision energy propagate in forward direction. Unfortunately, a collider is blind for exactly this direction as the forward direction is pointing right into the pipe but not to the detectors. Therefore, experimental data suffers from great uncertainties and the interactions of interest need to be formulated theoretically.

All models have in common that they describe hadrons as a composition of so-called partons which are quarks (valence quarks, diquarks, sea quarks) and gluons. A hadronic interaction is then defined as the exchange of color charge between some of the partons of the two interacting hadrons. The color charge exchange is symbolized as a string which can fragment depending on the exchanged energy. String fragmentation leads to the production of new hadrons [38]. Depending on the transferred momentum, one differentiates between a soft hadron production process (with low momentum transfer) and a hard process (with high momentum transfer). One part of the hard process, which become very important for very high-energetic interacting particles, is the jet production. A jet is defined as a bulk of color neutral particles which were produced through string fragmentation and propagate in nearly the same direction. They can be observed very well at collider experiments where a cone shape is used to approximate the tracks of the jet particles [57]. Collider experiments provide the data necessary to test the applicability and accuracy of the hadronic interaction models. Especially the LHC (Large Hadron Collider at CERN) measured significant data sets from proton-proton collision that reach energies and phase spaces which are important for the studies of air showers. Hadronic interaction models which have been developed after those higher-energy LHC measurements are called post-LHC models. In this thesis, the three models SIBYLL, QGSJET and EPOS have been used for high energy interactions and compared to one another. For that reason, a short description of each of those three models is given:

- **SIBYLL**, as all models, was designed to give a good description of the general characteristics of the hadronic interactions and particle production in an extensive air shower for primaries with masses up to iron nuclei [58]. It was originally designed to implement the minijet model. A minijet is a jet with a small transverse momentum (2 – 3 GeV [38]). The minijet model regards those minijets as responsible for an increase of the hadronic interaction cross section [38]. In SIBYLL the minijet model is used to describe the hard processes whereas soft processes have been adopted to the model only from version 2.1 onwards with the Dual Parton Model. The performance of the model has been checked by comparing the theoretical results with data from fixed-target and collider experiments. The more experimental data became available, the more adjustments of the model needed to be done. From its first code in 1987 until today, the model SIBYLL has undergone many corrections and improvements of the cross sections, nuclear diffractions and other characteristics. In Ref. [58] one can find a detailed comparison of the models SIBYLL 2.1 and the latest version SIBYLL 2.3 d. Looking at the use of SIBYLL for air showers, it is obvious that the changes made in the model also affected air shower parameters, e.g. the depth of the shower maximum or the muon number at ground level. Even though the latest versions of SIBYLL have been tuned with LHC measurements, there are still some discrepancies noticeable when comparing air shower data with SIBYLL-simulated data. Especially the number of muons is of high importance due to its mass composition sensitivity. In this regard, SIBYLL needs further improvements to decrease the tension between simulation and data [58].

- The **QGSJet** model aims to implement the Quark-Gluon String (QGS) model which describes soft hadronic interactions very well. An extension of the QGS model in QGSJet makes it possible to describe semihard processes. A cut on the transverse momentum separates the nonperturbative soft from the perturbative hard processes [59]. QGSJet is based on the Parton-based Gribov-Regge theory in which multiple hadronic interactions are able to take place in parallel. The elementary interaction is represented by a phenomenological object called Pomeron [60]. The original model QGSJet-01 as well as the following improved versions QGSJet-II and QGSJet-III all produce results which match the experimental data of air shower experiments quite well. But also, for this model, improvements e.g. regarding the forward hadron production are desirable, so the QGSJet-III model has not reached a final state for predicting hadronic interactions yet [61].

- **EPOS** is another model that is based on the Parton-based Gribov-Regge theory. It is a consistent quantum mechanical multiple scattering approach based on Partons and strings. The cross sections and the particle production are calculated consistently, taking into account energy conservation in both cases. A difference to other models is that EPOS goes into much detail in calculating the processes in high string density areas (so-called core) while other models only consider the areas of low string densities. The core is the region for collective hadronization and thus leads to a large multiplicity of hadrons. Again, the original version of EPOS got improved over the years so that the versions EPOS 1.99, EPOS LHC, EPOS 2 and EPOS 3 exist. EPOS-LHC (first post-LHC version of EPOS) is publicly available while EPOS 2 and EPOS 3 are still under development [62].

Figure 23 gives an example of how different the three described hadronic interaction models predict the average number of muons for iron-induced (dashed line) and proton-induced (continuous line) air showers at a zenith angle of 67°. The version SIBYLL 2.1 predicts far less muons than all the other models. This was one important reason to improve the SIBYLL 2.1 code, which led to the version SIBYLL 2.3. In case of muon numbers, the models EPOS-LHC, QGSJetII-04 and SIBYLL 2.3d don't show great differences. Yet, the systematic uncertainties that come with the choice of one specific model have to be taken account of whenever it is used for air shower analysis. The electromagnetic component of an air shower is simulated with EGS4 (Electron Gamma Shower system version 4) which includes the interactions annihilation, bremsstrahlung, Bhabha scattering, Møller scattering and multiple scattering for electrons/positrons and Compton scattering, e^+e^- - pair production and the photoeffect for photons. Another option for analytical calculating the electromagnetic subshowers would be the NKG (Nishimura Kamata Greisen) formula, but even though it's a fast option, the electron densities are only calculated at certain points on the detector plane. This is different in EGS4 and also one reason for its long computing time. EGS4 is modified by barometric information of the air and the magnetic field of the Earth [55].

CORSIKA has implemented an option to include air-Cherenkov radiation in the air shower simulation.

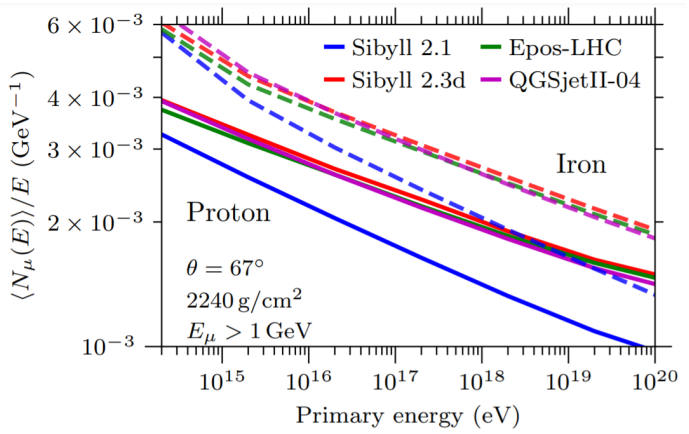

Figure 23: Model comparison of the average muon number as a function of the primary energy, at ground level in proton and iron induced air showers for muon energies above 1 GeV [58].

To reduce CORSIKA's general computing time, the option "thin sampling" selects a group of secondary particles with an energy sum below a certain threshold and from this group discards every particle but one random particle. It is also possible to let more than one particle survive, if the energy of more than one particle is above the thinning energy threshold. The surviving particles are then weighted and further tracked [55].

CORSIKA is a program which is continually being checked, improved, and extended. It relies on further progress in collider experiments and development of theoretical models. Thus, this Section only gave a very short summary of CORSIKA [55]. The so-called CORSIKA 8 project [63] is the latest planned, yet not complete framework which aims to combine modern computing with user-friendly interfaces and a big range of physical processes that can be used for detailed and precise calculations.

4.3.2. Detector simulation

For the simulation of the detector response, IceTop uses the toolkit GEANT4 which was developed to simulate the passage of particles through matter. GEANT4 processes the following aspects [64]:

- the detector geometry (in case of IceTop, the tank geometry and tank positions etc.)
- the materials used in the detector (not only inside the detector, but also the surrounding snow and the accumulated snow on top of the IceTop tanks is considered individually for each tank)
- the particles of interest (these are air shower particles simulated by CORSIKA which are injected into GEANT4 in considerations of the detector altitude of 2835 m)

- tracking particles on their way through the materials and external electromagnetic fields
- interactions of the particles with detector matter
- the response of the detector components (simulation of DOMs and PMTs)
- digitization and storage of events (simulation of front-end electronics)

Additionally, a standalone (single tank simulation) program named Tanktop has been developed for the purpose of determining the exact optical properties of the IceTop tanks. This includes the reflectivity of the tank walls, reflectivity of the ice-air transition, PMT efficiencies (wavelength-dependent) and photon-absorption in ice. Studies with Tanktop showed that it is indeed possible to use the VEM unit for efficient detector descriptions and signal comparison of different tanks. Furthermore, it was verified that the number of generated Cherenkov photons inside a tank is proportional to the number of detected photoelectrons, independently of the trajectory position and angle of the traversing particle [45].
In that way, IceTop gains a simulated dataset in the same format as the measured datasets. The simulated datasets undergo the same reconstruction procedures and are therefore comparable to the experimental results of IceTop.

This Chapter gave a summary of the IceTop surface array, its setup and operation method, and simulations used for IceTop analysis. The next Chapter 5 will be about the SLC and HLC charge related analysis performed in this thesis. The analysis and necessary background information will be explained, so that in the following Chapter 6 the results can be presented and discussed.

5. Analysis

The analysis goal of this thesis is to compare the experimental data of IceTop with simulated data with regards to the charge signals SLC and HLC, in order to separate muons from the electromagnetic shower component and find a better parameter for composition analysis. A lot of comparisons of measured data and Monte-Carlo simulation have been performed in the past, but they are usually focused on the features obtained from the charge signals, and not on the charge signals themselves. These features include the mass composition and energy spectrum [65] or the coordinates and number of tank hits [34]. Another type of study done in the last decade is the comparison of hadronic interaction models, especially the models SIBYLL, QGSJet and EPOS were involved. Again, these studies usually contain the comparison of cross sections or the simulated shower maximum depths X_{max} [58]. This creates the motivation of studying more IceTop specific characteristics. The SLC charge signals are of particular interest as they hold the yet unutilized potential to shed light on the mass composition of the detected cosmic ray particle, as mentioned in Section 3.2.3. While other SLC-inclusive studies concentrate on calculating the muon density in MC simulation and real data [66, 67], this work solely looks at the SLC and HLC charge signal distributions.

The questions investigated in this thesis can be summarized like this:

- Is the simulation describing the real charge signals well enough to be a reliable tool for the development of new analytical methods?
- Do the simulated and measured charges show the same features, mainly the background and muonic peak?
- To what extend differ the charge signals from different hadronic interaction models?
- How does the signal charge varies with a different zenith angle?
- How do the charge signals change with a different lateral distance?
- How do the charge signals change when only using SLC or when using HLC + SLC charges?

This Chapter concentrates on explaining which experimental and simulated datasets have been used in the analysis and what cuts have been applied.

5.1. IceTop data

As mentioned in Section 4.2.4, IceTop data runs through a series of filters which depend on the type of analysis that is wished to be performed. At IceCube/IceTop one speaks of filter levels. The higher the level, the more data filtering is applied. Here, filtering does not only mean event selection but also implies other data processes. The Level 0, which is also called trigger-level, describes the raw data directly after being recorded by the IceTop tanks when passing the discriminator trigger and IceTopSMT (see Section 4.2.4). In Level 1, also called the filter-level, different online filters (as described in Section 4.2.4) are applied to discard background events and therefore reduce the amount of data for satellite transmission. After the transmission the next filter level, Level 2, is used for reconstruction and cleaning processes. Amongst other things, they imply the processes described in Section 4.2.5. Level 0 to 2 are the levels with general filters used in all types of data analysis in IceCube/IceTop. Then, Level 3 is specifically chosen for each working group within the collaboration. In Level 3, specific cuts and filters are used to perform more advanced reconstructions, which are augmented in the following Level 4.
For this analysis, IceTop Level 3 data from the whole year of 2012 (January 2012 to December 2012) has been chosen. Especially the dataset from May 2012 onwards is particularly good for analysis, since there are simulation datasets for four different hadronic interaction models available. The simulated datasets are further explained in Section 5.3.
The experimental data was taken most of the time for 24 hours (sometimes less hours) per day in the year of 2012. The Level 3 processing includes a snow correction, SLC calibration, station cluster cleaning, background simulation and quality cuts as described in Section 5.2. As mentioned in Section 4.2.5 there are several types of charge information saved in an i3 file. They differ in their foregoing filter and cleaning procedure. E.g. the *OfflineIceTopHLCTankPulses* contain the raw HLC pulses in the unit VEM without any cleaning, so they are on Level 2 status. Correspondingly, the *OfflineIceTopSLCTankPulses* comprise the calibrated raw SLC pulses. After cleaning those pulses with a Laputop (reconstruction) seed under the assumption of a plane wave shower front, the resulting HLC and SLC pulses are saved in the objects *IceTopLaputopSeededSelectedHLC* and *IceTopLaputopSeededSelectedSLC*, respectively. The HLC and SLC charges from the pulses of the latter objects have been used for this analysis[4]. The charges have been selected in different ways (i.e. using different cuts) and collected into particular charge signals. The histograms showing those charge distributions are presented in Chapter 6. Comparing the experimentally measured with the simulated charge signals is the main objective of this analysis.

5.2. Quality cuts

To select the high quality events which are interesting for cosmic ray studies, the events have to pass certain cuts before they are used for creating the charge distributions. For this analysis, the applied quality cuts are the following:

[4]Furthermore, the IceCube software *IceTray* was used in this analysis.

- IceTop_StandardFilter == 1: The event passes the IceTop Standard Filter, i.e. the event triggered at least 5 stations

- IceTopMaxSignalAbove6 == 1: The largest tank signal provoked by the event is greater than 6 VEM

- $\log_{10}(S_{125}) > 0.0$: The reconstructed value for S_{125} (see Section 4.2.5) must be at least 1 VEM. This is equivalent to an energy cut as it selects a certain shower size and discards small showers.

- fit_status == 0: The Laputop fit was successful

- IceTop_reco_succeeded == 1: The event was successfully reconstructed (see Section 4.2.5)

- BetaCutPassed == 1: The event passed the cut on the reconstructed parameter beta (see Section 4.2.5)

- $\theta_{min} \leq \theta < \theta_{max}$: The air shower inclination θ (zenith angle) must be smaller than θ_{max} but larger than θ_{min}. Generally, the maximum angle $\theta_{max} = 37°$ is used as quality cut because there the detector reaches its full efficiency. In this analysis, two different cuts on the zenith angle θ were used. The exact values are given in the following text.

- $r < 400$ m: The shower core of the event is located within 400 m of the IceTop array to avoid the inaccuracy of shower core reconstruction at the edge of the array.

Besides the quality cuts an additional cut on the lateral distance r, the shortest distance from any point to the shower axis, was applied. Two distance ranges were chosen: The first range close to the shower core is $400\text{m} \leq r < 500\text{m}$ and the second range is $600\text{m} \leq r < 700\text{m}$, which is far from the shower core axis. As of now, $r_1 = 450\text{m}$ will refer to the first range and $r_2 = 650\text{m}$ to the second range.
Concerning the angle cut, the cuts were chosen in a way that one angle cut would cover the vertical showers while the second cut would include more inclined showers. The first cut θ_1 is using the values $\theta_{min} = 0°$ and $\theta_{max} = 18°$ and the second one θ_2 implies the values $\theta_{min} = 25°$ and $\theta_{max} = 37°$.
Furthermore, for this analysis the events were selected by an energy cut. The true energy cut was chosen to be $10^{6.95}\ \text{GeV} \leq E_{true} \leq 10^{7.45}\ \text{GeV}$. For the experimental data where the true primary energy is not known, the energy cut is equivalent to a cut on the reconstructed parameter S_{125} because S_{125} is linearly dependent on the primary energy. The calculation of the energy cut is described in Section 5.4.
After an event has passed all the mentioned cuts and filters, it was added to the particular charge distribution.

5.3. Simulation

Simulated charge signals were gained by applying the same cuts and filters of Section 5.1 and 5.2 on simulated datasets. These datasets have the same format and structure as the experimental datasets, except that they also contain the true information of the primary particle and of the air shower components which are of course unknown in the experimental datasets. Simulated datasets don't contain as many events as the datasets of one year of measurements at IceTop. But there are for sure enough events simulated to get high enough statistics for a comparison of both dataset types. The exact number of events depends on the used cuts and will be written on some of the histograms in Chapter 6. Roughly speaking, the number of events differs by a factor of 100.
IceTop data from 2012 was simulated with CORSIKA using four hadronic interaction models: SIBYLL 2.1, SIBYLL 2.3, EPOS-LHC and QGSJet-II 04. For the simulation of each dataset, the same cut on the primary energy and on the zenith angle were applied. The primary energies lie between 10^5 GeV and 10^8 GeV. The zenith angle is in the range from 0° to 65°. For each hadronic interaction model there is a dataset for a proton-induced and an iron-induced air shower. Only for SIBYLL 2.1 there exist additional datasets for helium- and oxygen-induced air showers. The datasets of SIBYLL 2.3, EPOS-LHC and QGSJet-II 04 contain 6000 air shower events, while the datasets of SIBYLL 2.1 are composed of 20000 events, each.

5.4. Energy cut

The energy cut mentioned in Section 5.2 can only be directly used for simulated data because here the true primary energy is known. For experimental data, a shower size, S_{125}, cut was derived directly from the energy cut on the simulation. The S_{125} cut was calculated by plotting the common logarithm of true primary energy E_{true} over the common logarithm of the simulated S_{125} parameter and performing a linear regression, as can be seen in Figure 24. The regression line is described by:

$$\log_{10}(E_{true}(S_{125}/\mathrm{VEM})) = p0 + p1 \times \log_{10}(S_{125}) \; . \tag{21}$$

Before the energy and S_{125} were plotted together, the true energy had to be weighted with $E^{-2.7}$. The reason is that in CORSIKA simulations the cosmic ray energy spectrum follows a power law with index $\gamma = 1.0$ while the experimentally observed spectrum reveals an average index of $\gamma = 2.7$. So, to be able to compare simulated with experimental data, the energy spectra need to follow the same power law.

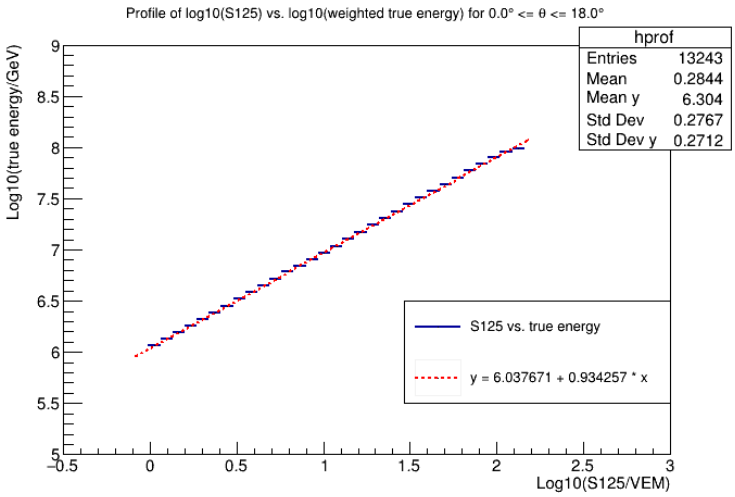

Figure 24: Profile histogram showing the linear dependence (blue) of the logarithmical true energy and S_{125} parameter as obtained from simulations with the model SIBYLL 2.1 with proton primary. The red dashed line is the linear fit function. The zenith angle cut is θ_1 (from 0° to 18°).

The necessary weighting factors w_i for three different energy ranges were calculated with Equation (22), of which the derivation can be found in Ref. [68].

$$w_i = A_i \times \left(\frac{E}{E_0}\right)^{-1.7} \times 2\pi(1 - \cos(\theta_{max})) \ . \tag{22}$$

The energy bins i and the associated resampling radii r_i were chosen as described in Ref. [66] which lead to the resampling areas $A_i = \pi \times r_i^2$. The resampling area is the area on the IceTop array in which the simulated air shower was placed. The values of E_i, r_i and A_i can be found in Table 1. The term E/E_0 states the simulated true primary energy in the unit GeV. The last term $2\pi(1 - \cos(\theta_{max}))$ represents the solid angle of the incident air shower with a maximum zenith angle θ_{max}. This is a simple way of flux weighting because the spectral index changes in the knee and ankle region of the energy spectrum are not considered. However, it was assumed to be sufficient for the calculation of an energy cut. For the comparison of charge signal distributions, the simulated energy was weighted with the H4a model [69] which is explained in Section 5.5.

$\log_{10}(E_i/\text{GeV})$	Resampling radius r_i (km)	Resampling area A_i (km²)
5 - 6	0.8	2.01
6 - 7	1.1	3.80
7 - 8	1.7	9.08

Table 1: Commonly used energy ranges and resampling radii and areas for IceTop simulations [66, 68].

The fitting procedure as shown in Figure 24 was done for both zenith angle ranges and for each simulation model, since the relation of E_{true} and S_{125} is slightly different in each model. After performing the fit, Equation (21) can be used to calculate the maximum and minimum value of S_{125} when setting the energy to its maximum value $10^{7.45}$ GeV or its minimum value $10^{6.95}$ GeV (see Section 5.2). Table 2 contains the fitting parameters that were used for the S_{125} cut in the experimental and simulated datasets as well as the obtained values of the S_{125} cut for each hadronic interaction model.
Since the S_{125} cut is slightly different for each hadronic interaction model, in this analysis the model-specific cut was used for the experimental data when comparing it with the data of that particular simulation model. Even for checks on solely the experimental data (without MC comparison) each cut has been used once. However, in Chapter 6 the "standard-cut" for the presented histograms will be the cut of SIBYLL 2.1 – H.

Hadr. int. model	Primary particle	Zenith angle range (°)	p0	p1	$\log_{10}(S_{125}^{min}/\text{VEM})$	$\log_{10}(S_{125}^{max}/\text{VEM})$
SIBYLL 2.1	H	0 - 18	6.038	0.934	0.98	1.51
		25.185 - 37	6.144	0.905	0.89	1.44
	Fe	0 - 18	6.094	0.889	0.96	1.53
		25.185 - 37	6.271	0.846	0.8	1.39
SIBYLL 2.3	H	0 - 18	6.024	0.930	1.0	1.53
		25.185 - 37	6.123	0.901	0.92	1.47
	Fe	0 - 18	6.073	0.887	0.99	1.55
		25.185 - 37	6.232	0.853	0.84	1.43
EPOS-LHC	H	0 - 18	6.006	0.935	1.01	1.54
		25.185 - 37	6.107	0.908	0.93	1.48
	Fe	0 - 18	6.065	0.880	1.01	1.57
		25.185 - 37	6.235	0.844	0.85	1.41
QGSJet-II 04	H	0 - 18	6.033	0.923	0.99	1.54
		25.185 - 37	6.133	0.901	0.91	1.46
	Fe	0 - 18	6.099	0.866	0.98	1.56
		25.185 - 37	6.258	0.838	0.83	1.42

Table 2: Fit results of the linear regression on the $E_{true} - S_{125}$ - distribution for each hadronic interaction model and both zenith angle ranges. The values of $\log_{10}(S_{125}^{min/max})$ are used for both, experimental and simulated datasets.

5.5. Weighting

The $E^{-2.7}$-flux weighting in Section 5.4 was only done for the calculation of the true energy cut. When looking at the charge signal distributions with the obtained energy cut applied, the simulated particle flux was weighted with the so-called H4a model [69] which returned weighting factors to be multiplied to the simulated charge signals.
The H4a model is one of Hillas' models to describe the flux of cosmic rays. The model consists of a few assumptions regarding the energy-dependent composition of cosmic rays. First, the origin of the particles up to the knee is supposed to be galactic, with supernova remnants being the source of acceleration. Those particles are called population 1. The origin of the particles between the knee and the ankle is unknown and just called 'Component B'. Those higher-energetic particles form the population 2. Population 3 consists of the highest energetic particles occurring above the ankle with extra-galactic origin. More populations could exist, however the Hillas H3a model [70] takes those three populations as the minimal assumption while the H4a model also includes a fourth population of only protons.
Second, each population (except population 4 in the H4a model) is assumed to consist of the five standard mass groups which are H, He, CNO, Mg-Si and Mn-Fe (as mentioned in Section 2.3).
Third, the magnetic rigidity is assumed to be the decisive cause for the features in the cosmic-ray energy spectrum, e.g. the changes of the spectral index. The rigidity $R = pc/Ze$ is defined as the relation of the total energy of a nucleus to its charge. At a fix energy, an increasing nucleus charge leads to a smaller rigidity. This important conclusion can be put in other words: At a fix energy, particles with low charge will reach a fix characteristic rigidity R_c faster than a highly charged particle. So e.g. if a particular acceleration mechanism ends at an energy E_c with a corresponding rigidity R_c, then the resulting change in the energy spectrum will first be seen for protons because they carry the lowest possible charge, followed by helium, and so on. So, the critical energy E_c will increase with the charge of the nucleon N. This is called a Peters cycle and has been observed in the knee region of the energy spectrum as shown in Figure 25. Here, the symbols show experimental results which were fitted with an all-particle spectrum using the H3a model (solid black line). The solid lines represent the nucleon-specific energy spectra, also derived from the H3a model. The Peters cycle is clearly noticeable: The knee first occurs for protons, then for helium nuclei, and last for iron nuclei.

The above-mentioned assumptions in the Hillas model lead to the expression of the all-particle spectrum in Equation (23), which was also used for the fit in Figure 25:

$$\Phi_i(E) = \sum_{j=1}^{3} a_{ij} E^{-\gamma_{ij}} \times \exp\left(\frac{-E}{Z_i R_{c,j}}\right), \tag{23}$$

$$\Phi_i(E) = \frac{dN}{d\ln E}\,. \tag{24}$$

In Equation (23), j is the index of the three populations (or four, then the sum goes up to 4), and i indicates the five mass groups, so $1 \leq i \leq 5$. Φ_i is the energy-dependent cosmic-ray particle flux of the i^{th} mass group, defined by Equation (24) with particle number N. γ_{ij} is the integral spectral index of the spectrum, Z_i is the charge number of mass group i, and R_{cj} is the characteristic rigidity [69, 70].

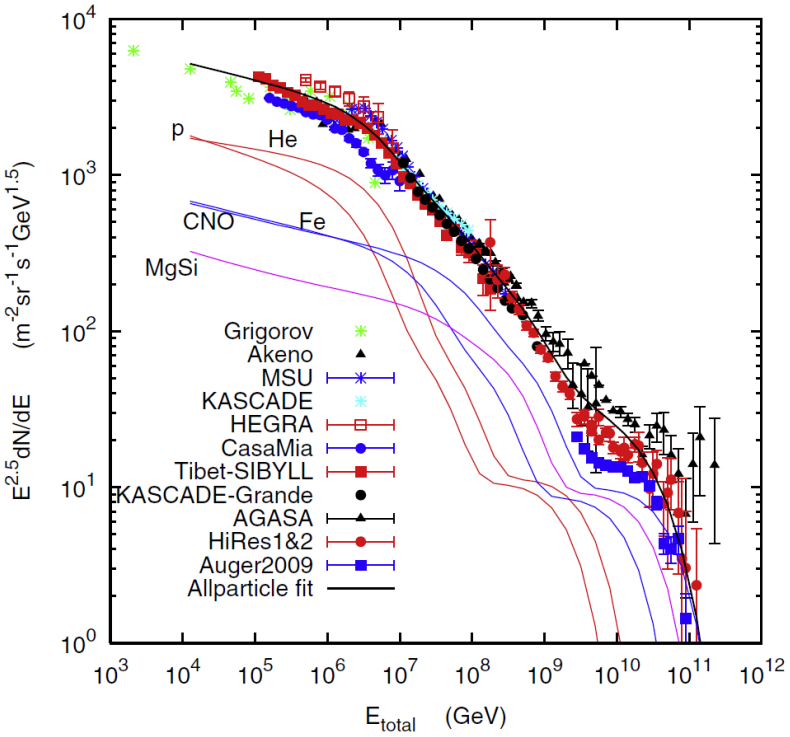

Figure 25: Cosmic-ray energy spectrum as measured with different experiments (symbols) and calculated with the H3a model (solid lines). The colorful lines show individual groups of nuclei from all populations. The black line is global fit of all populations from all nuclei compared to experimental data [70].

The weighting was performed for each simulation model before creating histograms of the SLC and/or HLC charge signals. In that way, the initially simulated sawtooth shaped $\log_{10}(E)$ distribution turned into a more even distribution. This is illustrated in Figure 26 for the simulation model SIBYLL 2.1 - H when weighting the true energy with the H4a model, where the quality cuts mentioned in Section 5.2 are not applied yet. The sawtooth pattern in simulation comes from the use of different resampling radii at higher energy regions, as listed in Table 1. The same weighting factors gained for the energy weighting were then used for the charge weighting.

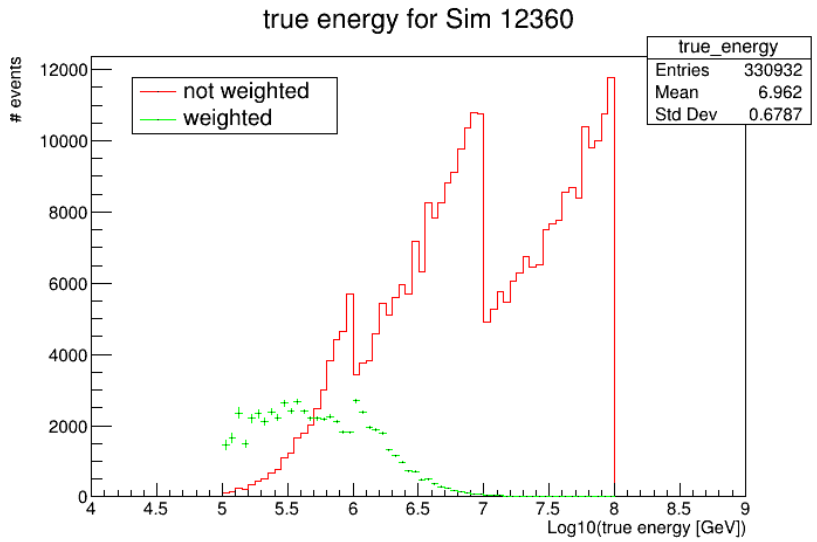

Figure 26: Comparison of the unweighted and weighted (using the H4a model) energy distribution, simulated with the hadronic interaction model SIBYLL 2.1 – H. No quality cuts are applied.

6. Results

In this chapter the charge signal distributions of the 2012 measurements at IceTop and the distributions obtained from Monte-Carlo simulations are presented and discussed. Before looking at the comparison of those two kinds of distributions, the general features of a charge distribution are described. Afterwards, it can be investigated and interpreted how those features change with different lateral distances and different zenith angles. In the last Section, the distributions of the four chosen hadronic interaction models are compared to each other. A final conclusion is drawn in Chapter 7.

6.1. Charge signal distribution

6.1.1. General features

A charge distribution contains the measured charge signals in unit of VEM (as explained in Section 4.2.2) that were gathered over a certain period of time. In case of this analysis, the charge signals from all IceTop tanks within a specific lateral distance range $r_{1,2}$ to the shower core and zenith angle range $\theta_{1,2}$ (defined in Section 5.2) of the air shower were added to the distribution of the whole year of 2012 in which over a million air showers were detected. An example distribution, shown in Figure 27, contains only the SLC charges measured at IceTop tanks at a lateral distance $r_1 = 450$ m and air shower events with zenith angle of θ from 0° to 18° (θ_1).
Looking at Figure 27, two main features stand out: One peak at approximately 0.3 VEM (meaning the center of the peak) and a second peak at approximately 1 VEM. The exact peak positions are given in Section 6.1.3. The first peak contains far more events than the second peak. This relation might change with the application of different cuts as will be observed in the next Section. Considering the definition of the unit of VEM as given in Section 4.2.2, a charge signal of 1 VEM should be detected when a vertical muon hits the tank. Therefore, one can assume that the majority of the charge signals in the second peak stem from muons, which are mainly SLC signals due to lower trigger probability at larger distance from the shower core axis. That is why the second peak is often referred to as the muon peak. From now on, the second peak will be also called muon peak. Furthermore, the first peak with its exponential decline is considered to originate from particles of the electromagnetic component of the air shower. Because the estimation of the muon number is the typical focus of an SLC analysis, the first peak is often called background peak or electromagnetic background peak. As of now, this name will be adopted in this thesis.

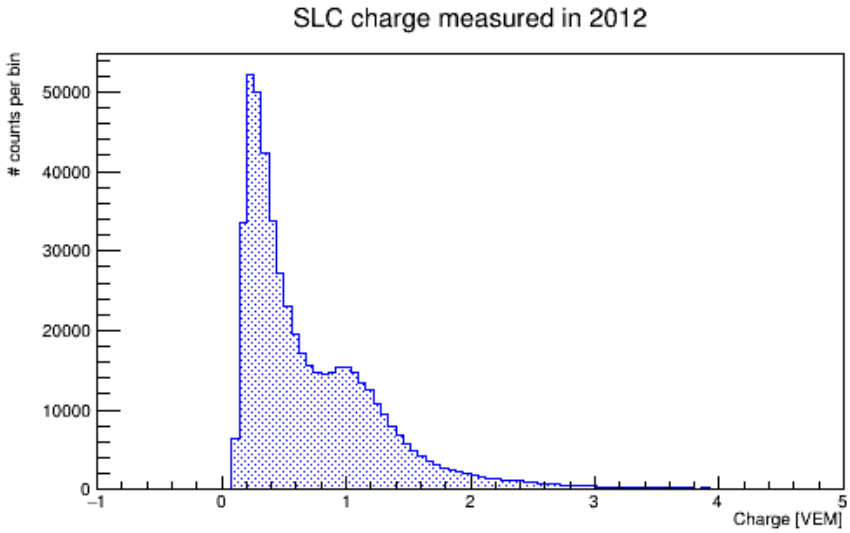

Figure 27: SLC charge signal distribution measured by IceTop in 2012. The S_{125} cut from the SIBYLL 2.1 − H model (see Section 5.4) is used. The cuts r_1 on the lateral distance and θ_1 on the zenith angle were applied.

6.1.2. HLC and SLC charge distributions

The shape of the charge distribution already changes when choosing either SLC or HLC hits only. As shown in Section 4.2.3, the amount of HLC hits decreases with increasing lateral distance, while it is the opposite for SLC hits up to a certain distance. Because the electromagnetic background dominates at small r, the muon peak is usually less apparent in HLC charge distributions as in SLC charge distributions. Figure 28 gives an example for this behavior. At distance r_1 the SLC hits already appear nearly twice as often as HLC hits. The r dependence will be further discussed in Section 6.2.2. The comparison of SLC and HLC charge distributions looks similar in case of simulation, as can be seen in Figure 29. Here, the two peaks are evident, yet the distributions show more fluctuations than the ones in Figure 28 due to low statistics. The reason is the H4a weighting which was described in Section 5.5 which greatly lowers the number of entries. It is still possible to compare distributions from Figure 28 with Figure 29, which the Section 6.2 will be about, because the peaks in the simulated SLC distributions are clear enough. To increase the statistics, also the distributions containing the sum of both, SLC and HLC charges, were added to the analysis. As can be seen in Figure 28, the HLC + SLC distribution (in grey) shows the muon distinctively, quite similar to the SLC distribution. In contrast, the muon peak in the HLC distribution is much broader. So, even though the HLC + SLC distribution implies the most entries, its shape is following the one of the SLC distribution. Therefore, this chapter will only present the results for the SLC distributions, and the sum of HLC and SLC distributions can be looked at in Appendix A.

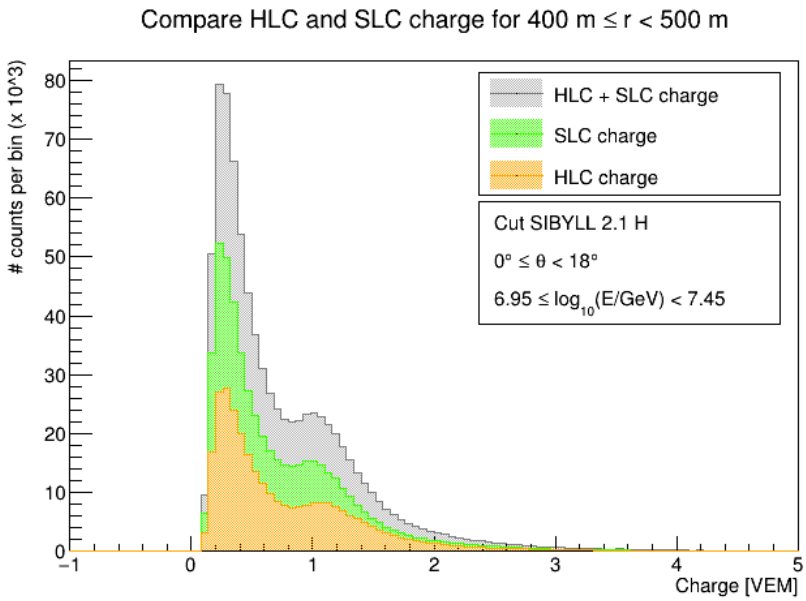

Figure 28: Comparison of SLC and HLC charge distributions measured by IceTop in 2012. The lateral distance r_1, zenith angle θ_1 and the S_{125} cut of the SIBYLL 2.1 (proton primaries) were used.

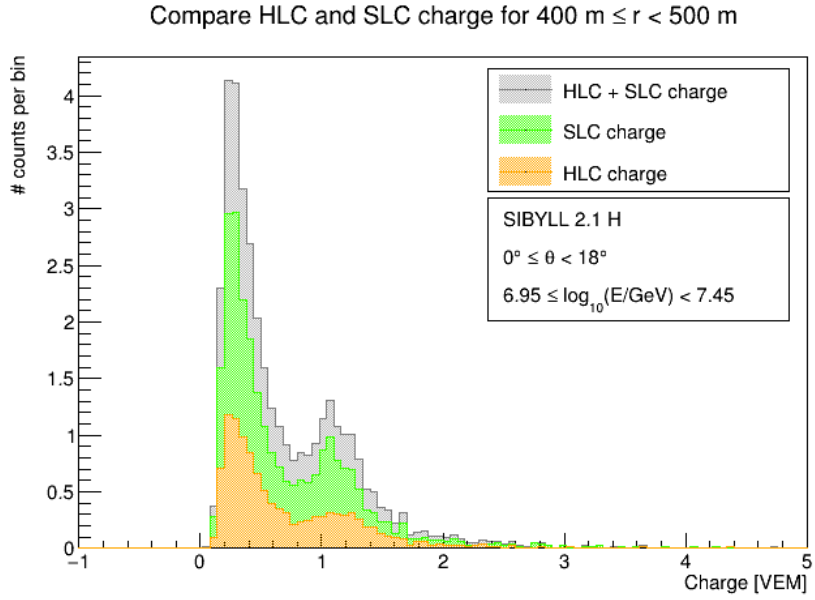

Figure 29: Comparison of simulated SLC and HLC charge distribution at distance r_1 and zenith angle θ_1. The hadronic interaction model SIBYLL 2.1 with proton primary was used. The statistics are much lower than in the measured experimental data because the simulated number of showers is smaller than the experimental data. This results in larger error bars and more fluctuation.

6.1.3. Muon peak position

The exact position of the muon peak can only be derived from fitting the charge distribution. For this purpose the fitting procedure was adapted from Ref. [68] where the fit function for the whole distribution was suggested to be the sum of two exponential functions (electromagnetic background) and a Gaussian function (muon peak). Equation (25) states this global fit function f_{tot}:

$$f_{tot} = \exp(p0 + p1 \times x) + \frac{p2}{p4 \times \sqrt{2\pi}} \times \exp\left(\frac{-(x - p3)^2}{(2 \times p4)^2}\right) + \exp(p5 + p6 \times x) \; . \tag{25}$$

The parameter p3 is equivalent to the center of the peak. All SLC and sum of HLC and SLC distributions for data and simulation were fitted with Equation (25). Figure 30 gives an example of how the fit looked like in case of an SLC distribution of experimental data with r_1 and θ_1 and S_{125} cut.

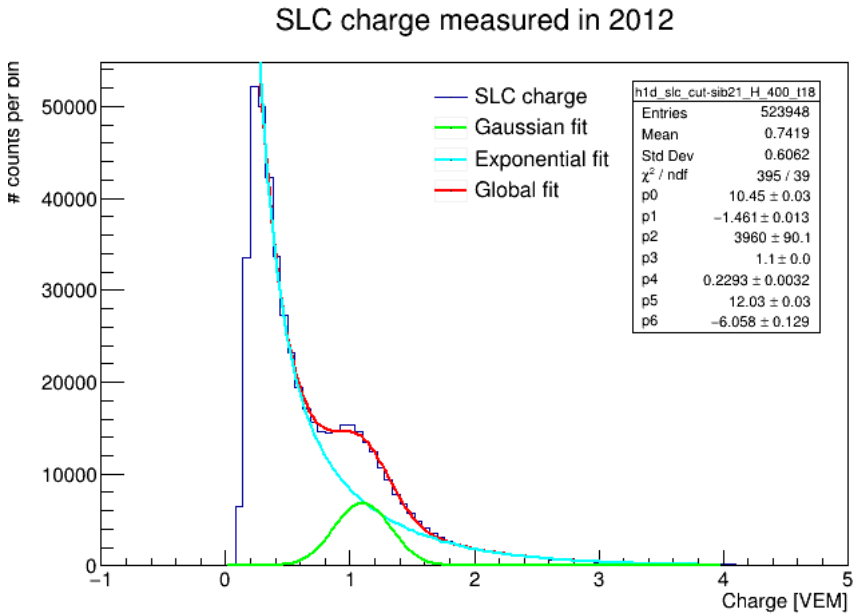

Figure 30: Fit on the SLC distribution from IceTop 2012 data (the same as in Figure 27), using the fit function f_{tot} from Equation (25).

All values of the center of the peak μ are tabulated in Table 3 in Appendix A.1. All plots showing the fit of simulated and experimental charge distributions for different cuts can be also found in Appendix A.1.

6.2. MC - data comparison

The comparison of charge distributions from simulation and from IceTop measurements will start with a view to the two cosmic ray primary particles, proton and iron. Then, the distributions for both lateral distances r_1 and r_2 will be looked at and discussed, followed by a comparison of both zenith angles, θ_1 and θ_2. The last part will concentrate on the comparison of distributions from all four hadronic interaction models.

6.2.1. Proton and iron primaries

First, the charge distribution of proton- and iron-induced showers (short: H-simulation and Fe-simulation) are compared to the experimental data. Figure 31 shows the H-simulation at the top and the Fe-simulation at the bottom, both performed with the SIBYLL 2.1 model. Here, the distance r_1 and zenith angle θ_1 were chosen. Both histograms, the simulated and the measured, were normalized according to Equation (26), so that their shape could be compared directly. In Equation (26), h stands for the analysed histogram and h^{norm} is the normalized histogram h:

$$h^{norm} = \left(\sum_{-1\ \mathrm{VEM}}^{5\ \mathrm{VEM}} h \right)^{-1} \times h \, . \tag{26}$$

The ratio plots on the bottom of the plots in Figure 31 give the ratio of number of entries in the data histogram to the number of entries in the simulated histogram bin by bin. I.e. a ratio value above 1 indicates that the simulations are underestimated. Of course, a ratio of 1 would be the ideal case as it would represent a perfect description of the experimental results by the simulation. Instead, fluctuations are noticeable which are very similar for the top and the bottom plot: While the ratio in the region of the electromagnetic background peak fluctuates slightly around 1, the ratio is clearly above 1 for the region in between the two peaks. The valley between the peaks is underestimated in both simulation histograms, and the muon peak is overestimated in relation to the first peak. In other words, the simulation models yield less electromagnetic background so that the muon peak is more dominant in simulated than in the measured distribution.
Additionally, one remarkable point is that the muon peaks in the simulated histograms are shifted towards higher VEM values. This shift was observed in the histograms of all four simulation models for every primary particle as can be checked up in Table 3. The shift length varies from model to model, and also depends on θ and r. Therefore, it is impractical to find a mean value of the difference between experimental and simulated muon peak center μ. Roughly speaking, the shift is in the order of 10^{-2} VEM. The cause of the shift is not clear, but it might be related with the SLC calibration, and probably needs further investigation.
The difference between proton and iron primaries can be best seen when plotting both distributions on top of each other. In that case, there are two ways to normalize the histograms. One way is to normalize all histograms to 1, which is done with Equation (26). Here, it is assumed that the simulation predicted 100% proton- or 100% iron-induced air showers, respectively. Another way is to assume a 50% H and 50% Fe composition of the

simulated air showers, which leads to the Equation (27) for the simulated histograms h_H and h_{Fe}:

$$h_{H,Fe}^{norm} = \frac{1}{2}\left(\left(\sum_{-1\ \mathrm{VEM}}^{5\ \mathrm{VEM}} h_H\right)^{-1} + \left(\sum_{-1\ \mathrm{VEM}}^{5\ \mathrm{VEM}} h_{Fe}\right)^{-1}\right) \times h_{H,Fe}\ . \tag{27}$$

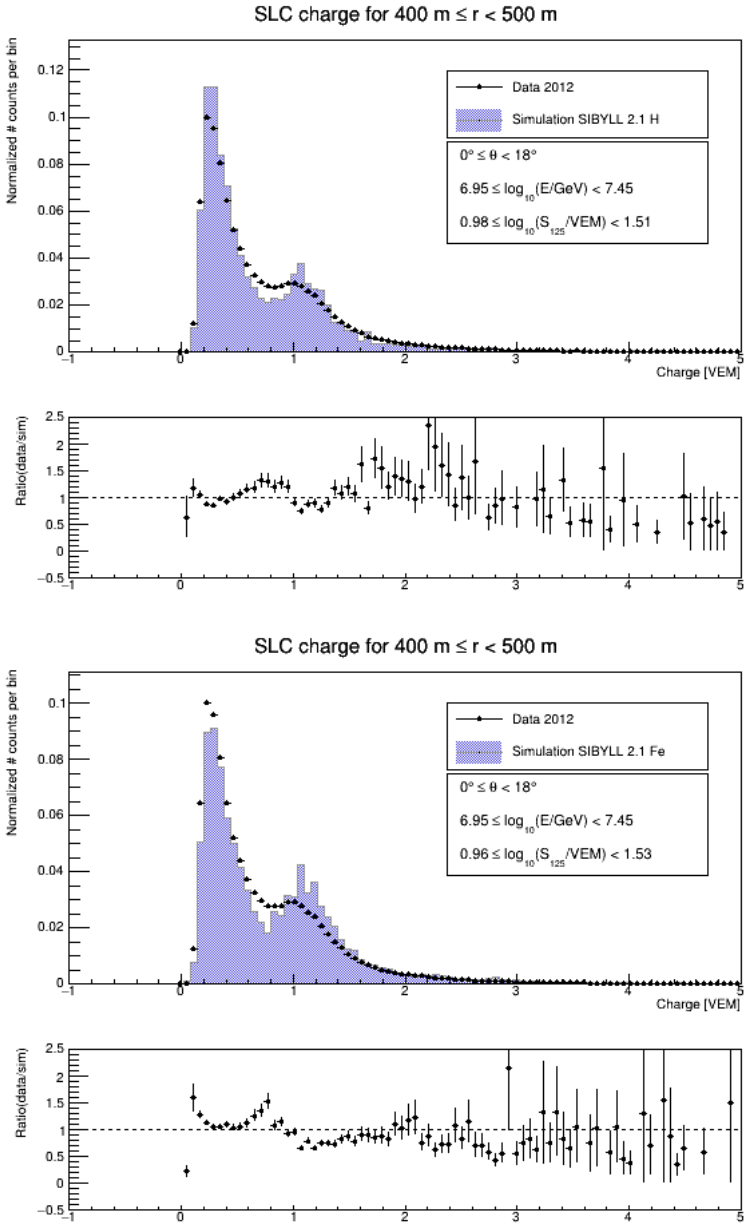

Figure 31: Comparison of experimentally measured SLC charge distribution with the distributions of SIBYLL 2.1 – H (top) and SIBYLL 2.1 – Fe primaries (bottom). The applied cuts/ranges are written in the legend boxes in the histograms.

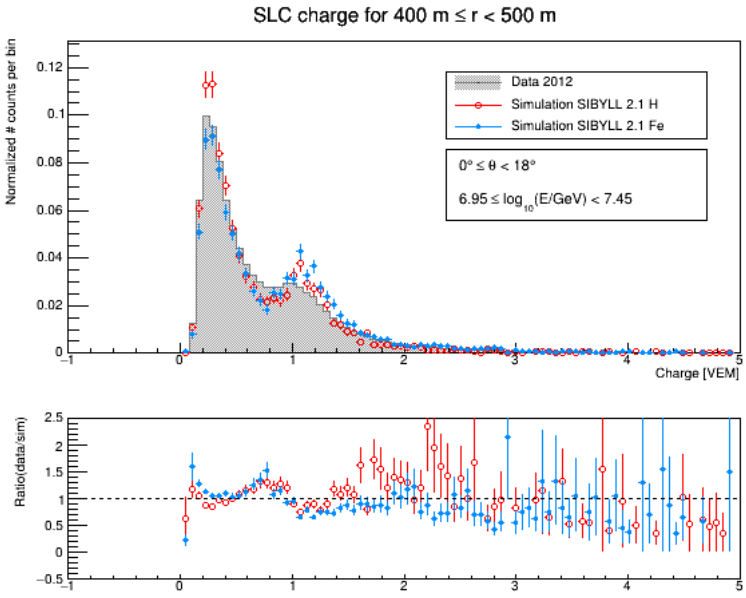

Figure 32: Experimental SLC charge distribution (gray filled histogram) compared to SIBYLL 2.1 simulated SLC charge distributions (red for H, blue for Fe), at a lateral distance r_1 and zenith angle θ_1. For the normalization Equation (26) has been used.

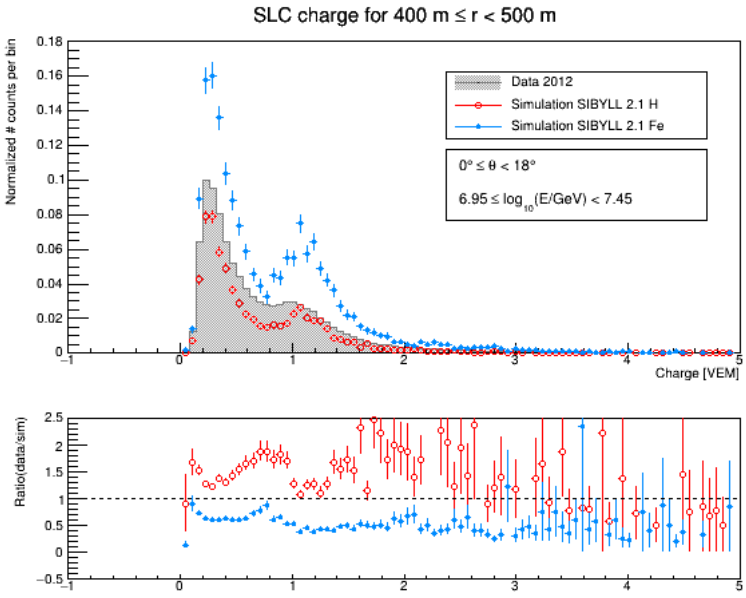

Figure 33: Experimental SLC charge distribution (gray filled histogram) compared to SIBYLL 2.1 simulated SLC charge distributions (red for H, blue for Fe), at a lateral distance r_1 and zenith angle θ_1. For the normalization Equation (27) has been used.

The normalization with Equation (26) is useful to investigate if the simulated distribution's shape and peak positions are in good agreement with the experimental results. However, using Equation (27) gives a more realistic comparison of the relation between simulated and experimental distributions. Both normalization Equations (26) and (27) have been used in this analysis and are presented in the Figures 32 and 33 for the SIBYLL 2.1 model with lateral distance r_1 and zenith angle θ_1.

Looking at Figure 32 and especially the ratio plot, the H- and Fe-simulation show a very similar overall shape. Though the electromagnetic background in the data histogram seems to be described better by the Fe-simulation, while the H-simulation shows a higher background peak. As described before, the muon peak is stronger defined in simulation and shifted to the right. One also notices a small shift of the H-simulation towards higher VEM values compared to the Fe-simulation.
This shift is only slightly noticable in Figure 33 where the H- and Fe-distributions are now clearly separated in consequence of the different normalization. The data distribution lies in the middle of the simulated distributions , and the Fe shower shows smaller deviation to the data. Especially the muon peak of the data in Figure 33 is more in agreement with the H- than the Fe-distributions.

In Appendix A.2.1, all the comparison histograms similar to Figure 31 are collected for each simulation model, lateral distance range, zenith angle range, and SLC as well as HLC + SLC charge distribution. Plots like Figure 32 and 33 for the other three interaction models are illustrated in Appendix A.2.2.

6.2.2. Lateral distance dependence

Now the charge distributions at two different lateral distances, $r_1 = 450$ m and $r_2 = 650$ m, are compared to one another. The distributions of the SIBYLL 2.1 model are shown representative for the rest of the analyzed distributions. The distributions with zenith angle θ_1 were chosen. Figure 34 shows the SLC charge distributions at distance r_1 on the top and at distance r_2 on the bottom. The data shows a good agreement (within ca. 25%) with the Monte-Carlo simulation around the electromagnetic and muonic peaaks. Above the muon peak, a large fluctuation can be seen due to low statistics of simulations.
By comparing the top and the bottom plots from Figure 34 one can see the muon peak being more distinctive at the larger lateral distance r_2. This observation is in accord with our expectations as it was explained in Section 4.2.3 that the electromagnetic shower component detectable on the ground decreases with increasing lateral distance while muon signals are still sufficiently measurable at large lateral distances. In this regard it is interesting to compare the number of detected HLC charges with the detected SLC charges. This comparison is shown in Figure 35. The number of entries of the HLC charge distribution is much lower than of the SLC charge distribution. When comparing Figure 35 with Figure 28, one can clearly notice a much greater reduction of the HLC charge distribution with in-

creasing lateral distance. This observation is again in agreement with the predictions from Section 4.2.3.

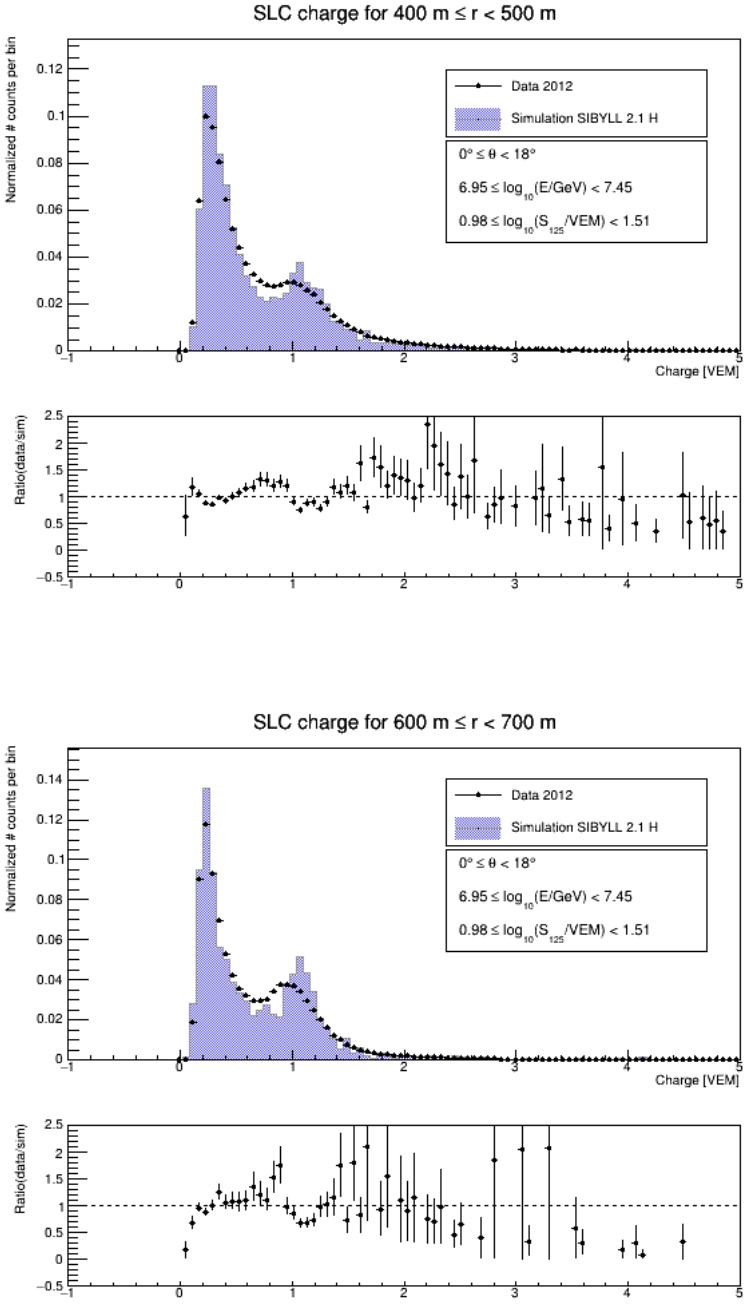

Figure 34: SLC charge signal distributions from IceTop 2012 data (black dots) and SIBYLL 2.1 – H primary (blue filled histogram) for zenith angle θ_1 and lateral distances r_1 (top) and r_2 (bottom).

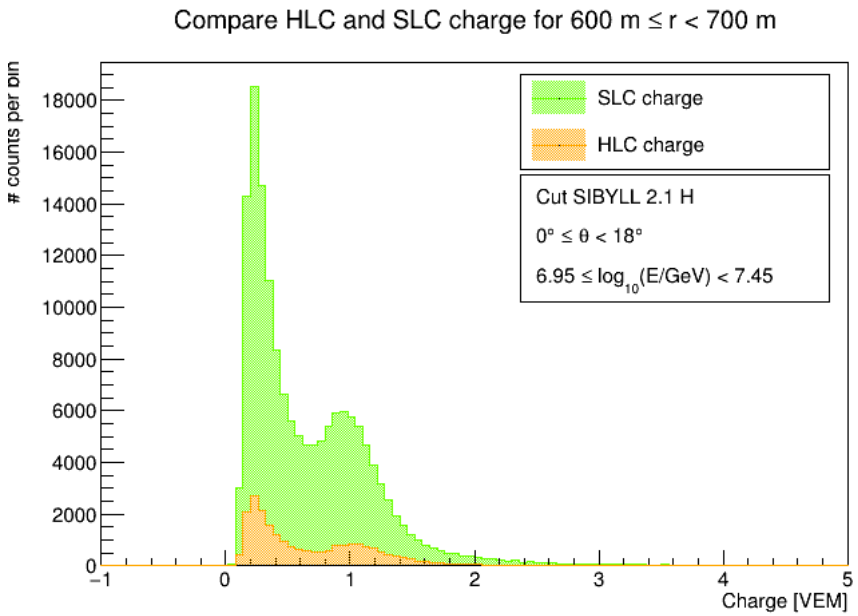

Figure 35: Comparison of the HLC (yellow) and SLC (green) charge distribution measured at IceTop in 2012. The lateral distance chosen is r_2, and the zenith angle is θ_1. The used S_{125} cut is from the SIBYLL 2.1 − H primary.

During the analysis, the charge distributions at lateral distances larger than 700 m have been briefly inspected. It was found that even though the muon peak became more and more distinctive, the statistics (especially in the simulated distributions) became too small for further investigations. Hence, the lateral distance cut was set to 700 m. In the same way, lateral distances below 400 m were looked at, too. They showed a higher number of counts, but the muon peak was hardly apparent, since the muonic components are overwhelmed by electromagnetic components at smaller lateral distance. So, for this analysis the minimal lateral distance was chosen to be 400 m where the muon peak is efficiently evident.

6.2.3. Zenith angular dependence

Next, since the muon content depends on the zenith angle, the two zenith angular ranges are compared. The first angle range θ_1 (from 0° to 18°) includes vertical to nearly vertical showers, whereas θ_2 (from 25° to 37°) contains inclined showers. The first expectation of such a comparison is that the muon peak is supposedly shifted towards higher VEM values as the unit VEM is calculated with vertical muons. Inclined muons can have a longer path when traversing through the IceTop tank (except for edge-clipping muons, i.e. muons which enter the tank through the edge) and therefore are able to produce more Cherenkov photons than vertical muons. This would lead to the emission of more photoelectrons in the PMT and thus to a higher charge.
Figure 36 shows the SLC charge distribution for vertical showers with θ_1 at the top and for

inclined showers with θ_2 at the bottom, both at lateral distance r_1 and for the interaction model SIBYLL 2.1 - H.

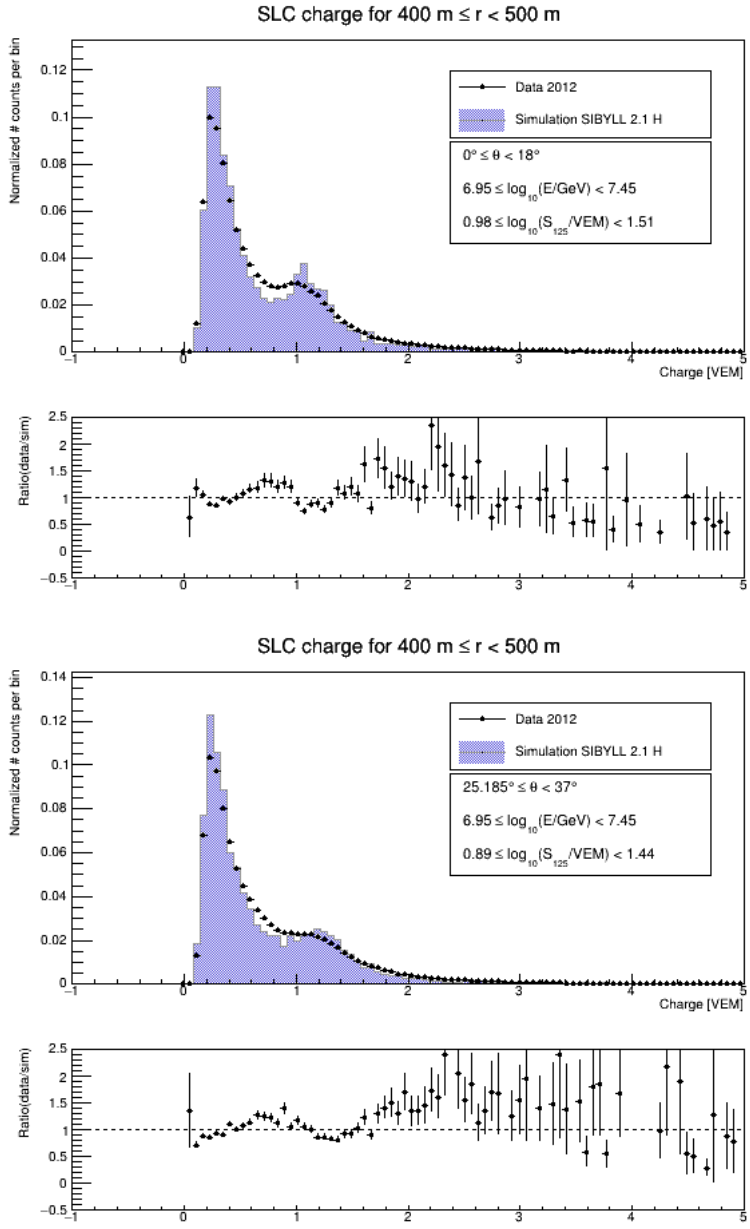

Figure 36: Experimental SLC charge distribution (black dots) compared to the SIBYLL 2.1 – H simulated distribution (blue filled histogram) at distance r_1 for zenith angle θ_1 (top) and θ_2 (bottom). The ratio between data and Monte-Carlo simulation can be seen as well.

Figure 36 confirms the above-mentioned expectation of a shifted muon peak in simulation and experimental data towards higher VEM values. Furthermore, the muon peak at θ_2 is

smoother and broader compared to the muon peak at θ_1. This might have to do with the higher occurrence of edge-clipping muons which yield a smaller charge signal than muons which travel the maximal length through an IceTop tank. This variety of track lengths in the ice of the tanks might smear out the muon peak.
To have a closer look at the shapes of the distributions in Figure 36, the histograms in Figure 37 are now plotted together for experimental data (top) and for simulation (bottom), respectively, for both zenith angle ranges.

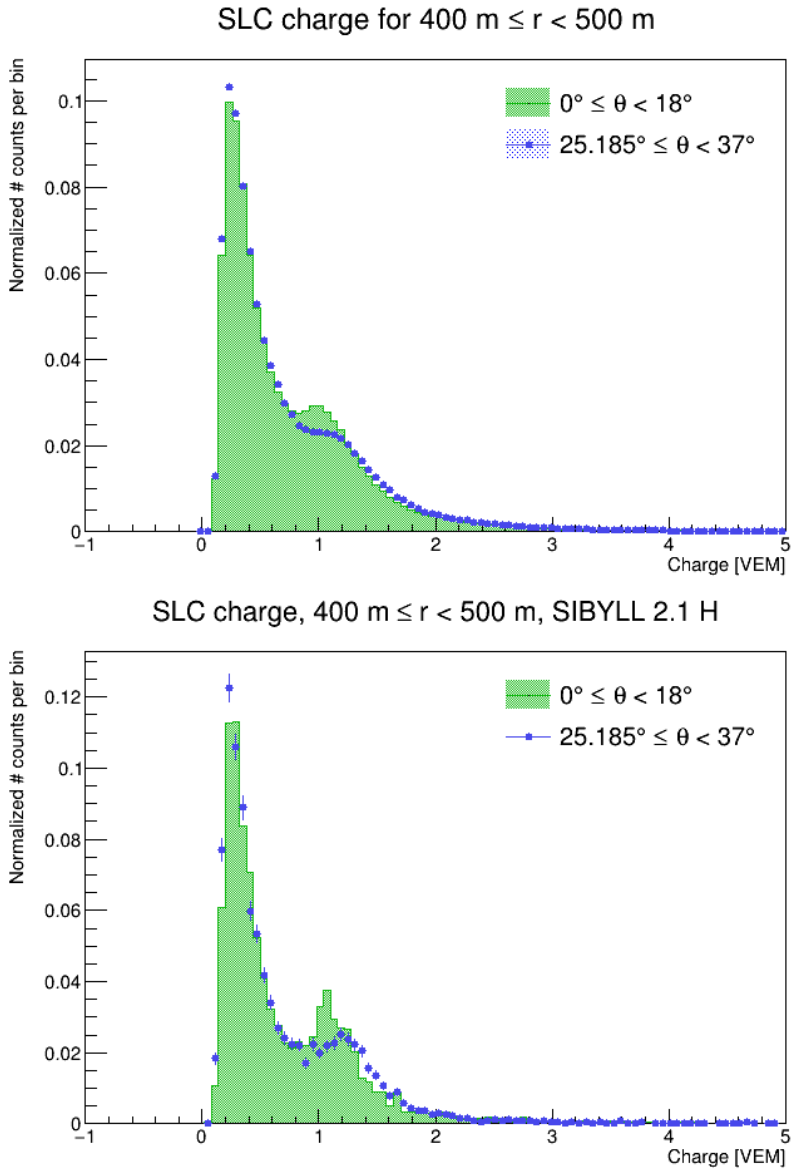

Figure 37: SLC charge distributions for θ_1 (green filled histogram) and θ_2 (blue dots) at a lateral distance r_1 from IceTop 2012 data (top) and SIBYLL 2.1 – H primary (bottom).

The histograms were normalized according to Equation (26). More histograms like the ones in Figure 37 for all interaction models and lateral distances can be found in Appendix A.3.

The shifting and smearing of the muon peak are more obvious in Figure 37 than the previous Figure. The electromagnetic peak has approximately the same shape in both zenith angle ranges. The reason for this behavior might be that electromagnetic particles produced in an extensive air shower are not necessarily propagating parallel to the shower direction but rather get deflected and emitted in various angles. So, independent of the air shower's zenith angle the electromagnetic component already reaches the IceTop tanks from different angles, while muons move nearly parallel to the shower axis and therefore hit the tanks in the direction of the shower.
It should be mentioned that even though it might not be very obvious in the bottom plot of Figure 36, the difference in the muon peak position between experimental and simulated data also exists for the zenith angle θ_2. This can also be checked by looking at the fit results in Table 3.

6.2.4. Hadronic interaction models

The last comparison between data and Monte-Carlo simulation is made with regard to the different hadronic interaction models. Figure 38 shows four different plots, one for each model, with SLC charge distributions for the zenith angle θ_1 and lateral distance r_1, with both primaries H and Fe plotted together. All four simulations are weighted with the H4a model.
The distributions of the models EPOS-LHC, QGSJet-II 04, SIBYLL 2.1 and SIBYLL 2.3 are quite similar, especially regarding the shapes and peak positions of the distributions. There are no major differences noticable, even though the SIBYLL 2.1 model is a pre-LHC model. Figure 39 gives a last direct comparison of the simulation models by plotting the SLC distributions together for two different zenith angular ranges, for proton primaries. Each distribution was normalized with Equation (26). This Figure in general shows the very good agreement of the distributions from the four models SIBYLL 2.1, SIBYLL 2.3, EPOS-LHC and QGSJet-II 04: All models lead to a relatively similar charged particle content in air showers in the energy region of a few PeV. This similarity doesn't only occur for proton primaries but also for iron primaries at both lateral distances r_1 and r_2. Furthermore, the models neither differ greatly at a low zenith angle nor at higher zenith angles. However, the muon peak of the SIBYLL 2.1 model shows slightly lower values than the other models. Plots like Figure 39 for iron primaries can be found in Appendix A.4.

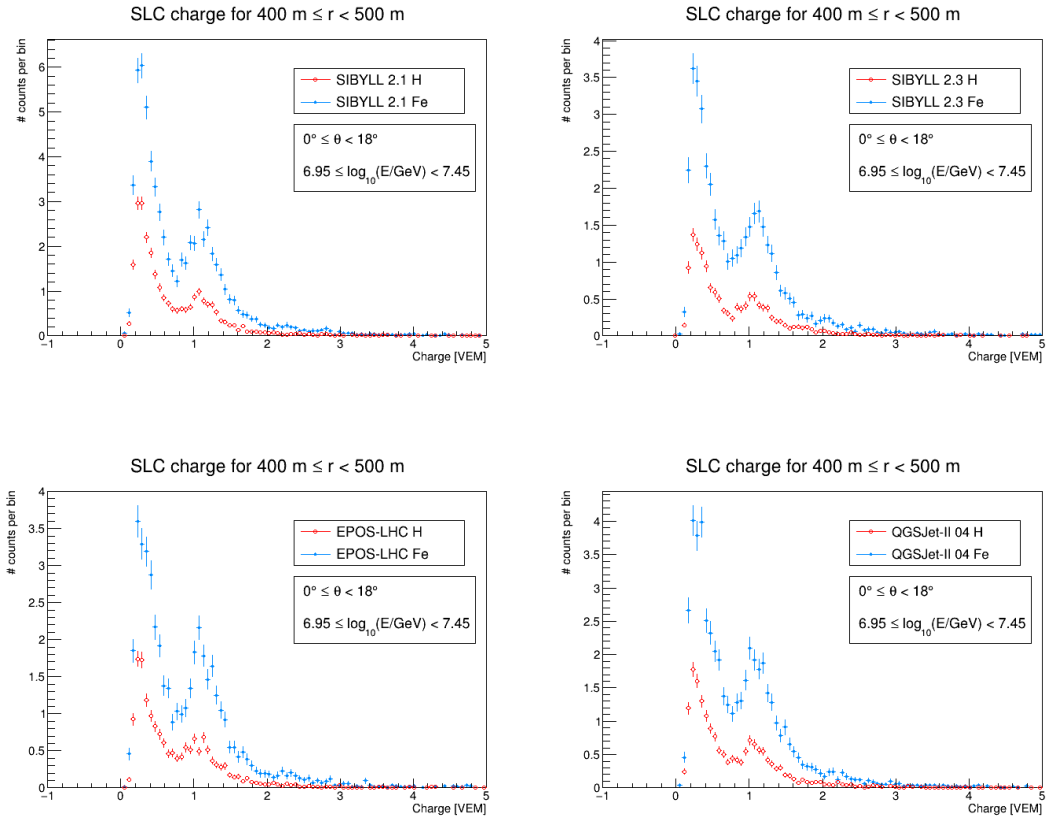

Figure 38: Comparison of the SLC charge distributions from all four different interaction models (SIBYLL 2.1, SIBYLL 2.3, EPOS-LHC and QGSJet-II 04) for zenith angle θ_1 and lateral distance r_1. Both distributions for proton (red) and iron (blue) primaries are plotted.

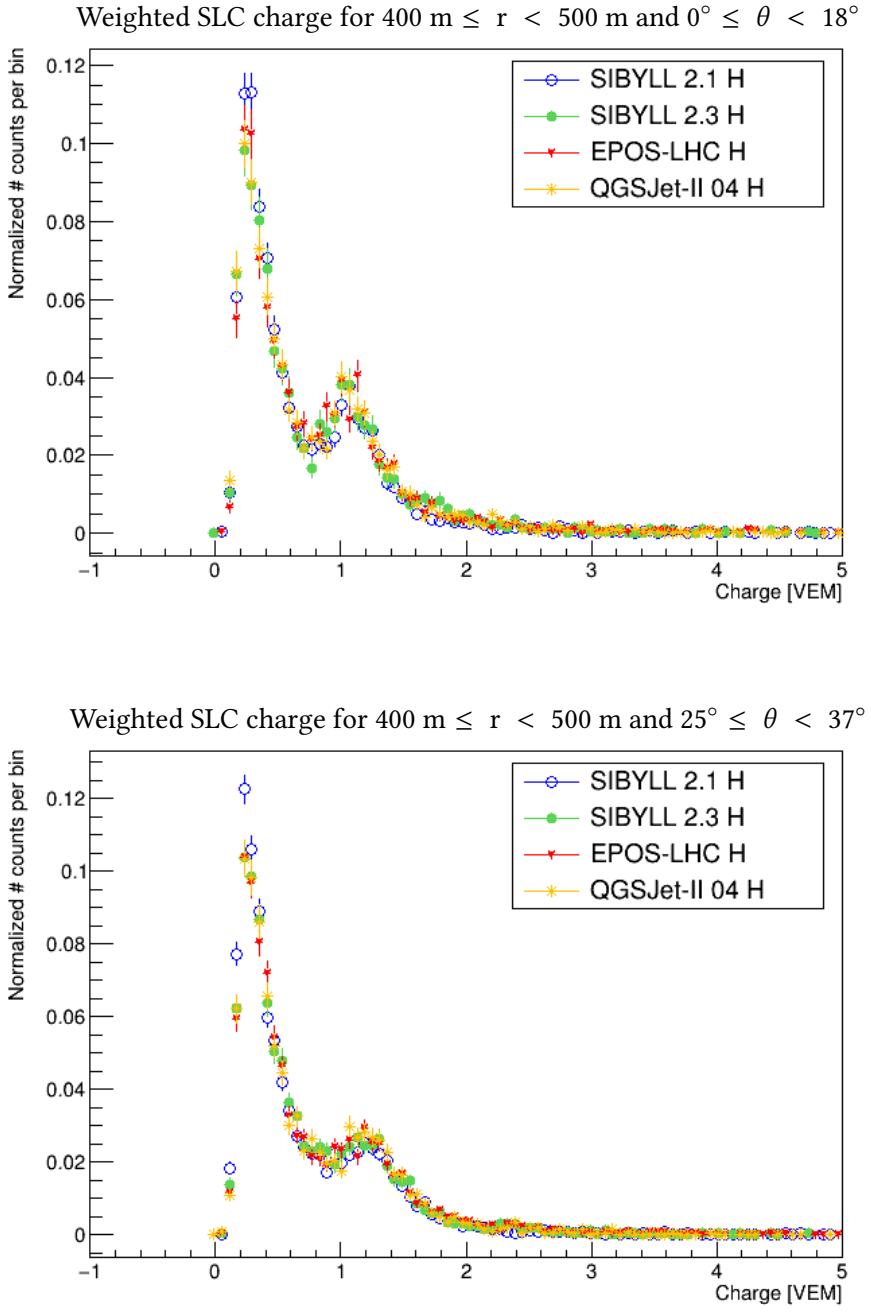

Figure 39: SLC charge distributions of all four interaction models with proton primaries at a lateral distance of r_1 and zenith angle θ_1 (top) and θ_2 (bottom).

6.3. Discussion

In this last Section, the results of this work will be shortly summarized and discussed.
The comparison of simulated with experimental charge signals showed that for primary energies of some PeV the simulations describe the experimental measurements well, with some minor differences, so they can be regarded as reliable tool for the development of new analytical methods. In simulation and experimental data the same features occured in the charge signal distributions, especially the muonic peak and electromagnetic background peak. This is true for small (450 m) and large (650 m) lateral distances, as well as for small (up to 18°) and larger (25° to 37°) zenith angles. A small shift of the muonic peak in experimental data was noticeable, which should be further investigated.
The simulated charge signals of the four different hadronic interaction models didn't show any significant differences for any of the lateral distance and zenith angular cuts.
Furthermore, the SLC charge signal distributions revealed the muonic and background peak just as clearly as the distributions which contain the sum of HLC and SLC charge signals (presented in the Appendix A).
These results show that the IceTop surface array is sensitive to detect single muons in the presumed energy, lateral distance and zenith angular range. IceTop gathers enough statistics over the period of one year to use SLC charge signals in mass composition analysis.

7. Conclusion and Outlook

In this analysis, the charge signals measured by the IceTop experiment were studied. In particular, the SLC charge distributions were of high interest because they hold relevant information about the muon content of extensive air showers measured at IceTop. The muon content is important in air-shower physics because of its direct dependency on the mass of the primary particle.
The standalone SLC and additionally both, HLC and SLC, charge signal distributions from measurements in 2012 were compared to the simulated distributions. Here, four different simulation models, discriminable by their modeling of hadronic interactions, have been included in the comparison: SIBYLL 2.1, SIBYLL 2.3, EPOS-LHC and QGSJet-II 04. All simulations were weighted with the H4a model. The comparison was done for data at two different lateral distances, r_1 = 450 m and r_2 = 650 m, as well as for air showers with zenith angles in two different ranges, $0° \leq \theta_1 < 18°$ and $25° \leq \theta_2 < 37°$.
The comparison of experimental data with Monte-Carlo simulation showed a good agreement of both. The electromagnetic background peak as well as the muon peak from the experimental data are described well by each interaction model which in general estimate the background peak at little bit smaller but the muon peak a little bit higher compared to the experimental distributions. However, there is one minor difference with yet unknown origin: the shift of the muon peak to higher charges in the simulated distributions whose investigation would exceed the capacity of this thesis. Assuming that the cause for this peak shift is traceable, one can conclude that the simulations based on four different interaction models describe the experimental SLC and HLC + SLC charge distributions well enough to be used for IceTop analysis. Not only the simulated distributions but SLC charge distributions in general were found to be very useful for further composition studies. The muon peak in SLC distributions was clearly evident at large lateral distances where HLC charge distributions didn't show a clear muon peak anymore. Therefore, it is recommended to include SLC signals in the analysis of the mass composition of cosmic rays detected at IceTop.
Such an attempt has already started as it was mentioned in Section 4.2.3: The analysis from Ref. [54] aims to derive a muon-based mass sensitive parameter which can be applied to experimental IceTop data for an estimation of the cosmic ray mass composition. This analysis, as others do as well, relies on the accuracy of the simulated charge signals because the newly developed parameters need to be tested and evaluated on simulated datasets before they can be used on real experimental datasets.
In this way and other attempts to gain more information about the mass composition from simulation, it might be possible in the near future to develop new reliable methods for the

more precise calculation of the mass composition of cosmic rays. This would bring IceTop one step closer to tapping its full potential in the investigation of cosmic rays.

References

[1] M. Walter. "Early Cosmic Ray Research with Balloons". In: *Nuclear Physics B (Proc. Suppl.) 239-240 (2013) 11-18* (2013).

[2] C. Grupen. "The History of Cosmic Ray Studies after Hess". In: *Nuclear Physics B (Proc. Suppl.) 239-240 (2013) 19-25* (2013).

[3] T.K. Gaisser, R. Engel, and E. Resconi. *Cosmic Rays and Particle Physics*. Cambridge University Press, 2016.

[4] S. Gabici et al. "The Origin of Galactic Cosmic Rays: challenges to the standard paradigm". In: *arXiv:1903.11584v2 [astro-ph.HE]* (2019).

[5] R.A. Batista et al. "Open Questions in Cosmic-Ray Research at Ultrahigh Energies". In: *Journal Frontiers in Astronomy and Space Science* (2019).

[6] M.G. Aartsen et al. "Neutrinos and Cosmic Rays Observed by IceCube". In: *arXiv: 1701.03731v1 [astro-ph.HE]* (2017).

[7] C. Patrignani. "Review of Particle Physics". In: *Chinese Phys. C 40 100001* (2016).

[8] A. Aab et al. "combined fit of spectrum and composition data as measured by the Pierre Auger Observatory". In: *JCAP04(2017)038* (2017).

[9] S. Mollerach and E. Roulet. "Progress in high-energy cosmic ray physics". In: *arXiv: 1710.11155v1 [astro-ph.He]* (2017).

[10] NASA. *NASA Super-Tiger Balloon Shatters Flight Record*. `https://www.nasa.gov/centers/wallops/news/supertiger-record.html`. 2013.

[11] A.W. Labrador et al. "Galactic Cosmic Ray Energy Spectra for Heavy Elements (Ne to Zn) from 0.8 to 10 GeV/nuc with the SuperTIGER Instrument". In: *Proceeding of the 36th International Cosmic Ray Conference (ICRC)*. PoS(ICRC2019)095. 2019.

[12] T. Hams et al. "Elemental Abundances of Ultra-Heavy GCRs measured by SuperTIGER and ACE-CRIS and the Origin of Galactic Cosmic Rays". In: *Proceeding of the 34th International Cosmic Ray Conference (ICRC)*. PoS(ICRC2015)038. 2015.

[13] NASA. *NASA's Super-Tiger Balloon Breaks Records While Collecting Data*. `https://www.nasa.gov/home/hqnews/2013/feb/HQ_13-037_Balloon_Records.html`. 2013.

[14] W.R. Binns et al. "The SuperTIGER Instrument: Measurement of elemental abundances of ultra-heavy galactic cosmic rays". In: *The Astrophysical Journal 788 18* (2014). DOI: `10.1088/0004-637X/788/1/18`.

[15] NASA. *Scientific Balloons*. `https://sites.wff.nasa.gov/balloons/`. Accessed: August 2021.

[16] S. Torii and Y. Asaoka. “Extended Measurement of Comsic-Ray Electron and Positron Spectrum from CALET on the ISS”. In: *Proceeding of the 36th International Cosmic Ray Conference (ICRC)*. PoS(ICRC2019)142. 2019.

[17] B.F. Rauch. “Predicted CALET Measurements of Heavy and Ultra-Heavy Cosmic Ray Nuclei”. In: *Proceeding of the 34th International Cosmic Ray Conference (ICRC)*. PoS(ICRC2915)627. 2015.

[18] E.S. Seo. “Cosmic Ray Energetics And Mass: from balloons to the ISS”. In: *Proceeding of the 34th International Cosmic Ray Conference (ICRC)*. PoS(ICRC2015)574. 2015.

[19] M. Israel et al. *NASA Stratospheric Balloons, Report of the Scientific Ballooning Assessment Group*. 2012.

[20] P. Maestro. “Cosmic rays: direct measurements”. In: *Proceeding of the 34th International Cosmic Ray Conference (ICRC)*. PoS(ICRC2015)016. 2015.

[21] Telescope Array Project at the University of Utah. `www.telescopearray.org/index.php/about/fluorescence-detection`. Accessed: August 2021.

[22] R.U. Abbasi et al. “Surface detector of the TAx4 experiment”. In: *arXiv:2103.01086v1 [astro-ph.IM]* (2021).

[23] H. Tokuno et al. “New air fluorescence detectors employed in the Telescope array experiment”. In: *arXiv:1201.0002v1 [astro-ph.IM]* (2011).

[24] Telescope Array Project at the University of Utah. `www.telescopearray.org`. Accessed: August 2021.

[25] Telescope Array Project at the University of Utah. *History of the Air Fluorescence Technique*. `http://www.telescopearray.org/index.php/history/history-of-the-air-fluorescence-technique`. Accesssed: August 2021.

[26] Telescope Array Project at the University of Utah. *Surface Detection*. `http://www.telescopearray.org/index.php/about/surface-detection`. Accessed: August 2021.

[27] D. Ivanov. “Energy Spectrum Measured by the Telescope Array Experiment”. In: *Proceeding of the 36th International Cosmic Ray Conference (ICRC)*. PoS(ICRC2019)298. 2019.

[28] R.U. Abbasi et al. “Indications of Intermediate-Scale Anisotropy of Cosmic Rays with Energy Greater Than 57 Eev in the Northern Sky Measured with the Surface Detector of the Telescope Array Experiment”. In: *The Astrophysical Journal Letters 790 L21* (2014). DOI: `10.1088/2041-8205/790/2/L21`.

[29] J.C. Arteaga-Velázquez and J.D. Àlvarez. “The spectrum of the light component of TeV cosmic rays measured with HAWC”. In: *Proceeding of the 36th International Cosmic Ray Conference (ICRC)*. PoS(ICRC2019)176. 2019.

[30] M. Amenomori et al. “"Primary cosmic-ray spectra and composition in the energy range from 50 TeV to 10^{16} eV observed with the new Tibet hybrid experiment”. In: *Proceeding of the 36th International Cosmic Ray Conference (ICRC)*. PoS(ICRC2019)288. 2019.

[31] T. Antoni et al. “KASCADE measurements of energy spectra for elemental groups of cosmic rays: Results and open problems”. In: *Astroparticle Physics 24(1-2), 1 -25* (2005). DOI: 10.1016/j.astroparticle.2005.04.001.

[32] F.G. Schröder. “Science Case of a Scintillator and Radio Surface Array at IceCube”. In: *arXiv:1908.11469v1 [astro-ph.HE]* (2019).

[33] R. Koirala and T.K. Gaisser. “Low Energy Cosmic Ray Spectrum from 250 TeV to 10 PeV using IceTop”. In: *Proceeding of the 36th International Cosmic Ray Conference (ICRC)*. PoS(ICRC2019)318. 2019.

[34] M.G. Aartsen et al. “Cosmic Ray Spectrum from 250 TeV to 10 PeV using IceTop”. In: *arXiv:2006.05215v1 [astro-ph.HE]* (2020).

[35] C. Evoli. *The Cosmic Ray Spectrum*. https://zenodo.org/record/4396125#.YIA97dJR02w. Accessed: August 2021. 2020.

[36] CORSIKA. *CORSIKA shower Images: Proton Showers*. https://www-zeuthen.desy.de/~jknapp/fs/proton-showers.html. Accessed: August 2021.

[37] Z. Hampel-Arias. *Cosmic-Rays*. https://zhampel.github.io/research/. Accessed: August 2021.

[38] R. Engel, D. Heck, and T. Pierog. “Extensive Air Showers and Hadronic Interactions at High Energy”. In: *Annu. Rev. Nucl. Part. Sci. 2011. 61:467-89* (2011).

[39] Georg-August-Universität Göttingen. *Bremsstrahlung*. https://lp.uni-goettingen.de/get/text/6632. Accessed: August 2021.

[40] S.R. Tornga. “A Prototype Compton Imager - Simulations, Measurements and Algorithm Development”. MA thesis. Albuquerque, New Mexiko: The University of New Mexiko, 2005.

[41] Georg-August-Universität Göttingen. *Charakteristische Strahlung*. https://lp.uni-goettingen.de/get/text/6634. Accessed: August 2021.

[42] A. Haungs et al. “Energy spectrum and mass composition of high-energy cosmic rays”. In: *Rep. Prog. Phys. 66 1145* (2003).

[43] P.A. Zyla et al. (Particle Data Group). “Review of Particle Physics”. In: *Prog. Theor. Exp. Phys. 2020, 083C01 (2020)* (2020). DOI: 10.1093/ptep/ptaa104.

[44] IceCube South Pole Neutrino Observatory. *Research Highlights*. https://icecube.wisc.edu/science/. Accessed: August 2021.

[45] R. Abbasi et al. “IceTop: The surface component of IceCube”. In: *arXiv:1207.6326v2 [astro-ph.IM]* (2012).

[46] Hamamatsu. *RICH - Ring Imaging Cherenkov Detector*. https://hep.hamamatsu.com/eu/en/dt/ccr.html. Accessed: August 2021.

[47] IceCube South Pole Neutrino Observatory. *Measuring the Neutrino Cross Section with Earth Absorption*. https://icecube.wisc.edu/gallery/measuring-the-neutrino-cross-section-with-earth-absorption/. Accessed: August 2021.

[48] IceCube South Pole Neutrino Observatory. *28 very high energy events, published in Science (November 2013)*. https://icecube.wisc.edu/gallery/28-very-high-energy-events-published-in-science-november-2013/. Accessed: August 2021.

[49] M.G. Aartsen et al. "The IceCube Neutrino Observatory Part III: Cosmic Rays". In: *arXiv:1309.7006v2* (2013).

[50] Hamamatsu. https://www.hamamatsu.com/eu/en/product/optical-sensors/pmt/about_pmts/index.html. Accessed: August 2021.

[51] W. R. Leo. *Techniques for Nuclear and Particle Physics Experiments: A How-To Approach*. Springer-Verlag Berlin-Heidelberg 1987, 1994.

[52] K. Greisen. "Cosmic Ray Showers". In: *Annu. Rev. Nucl. Sci. 1960.10:63-108* (1960).

[53] S. Euler, J. Gonzalez, and B. Roberts. "Simulation studies for a Surface Veto array to Identify astrophysical Neutrinos at the South Pole". In: *Proceeding of the 34th International Cosmic Ray Conference (ICRC)*. PoS(ICRC2015)1070. 2015.

[54] D. Kang, S.-A. Browne, and A. Haungs. "Studies of a muon-based mass sensitive parameter for the IceTop surface array". In: *arXiv:2109.02506v1 [astro-ph.HE], Proceeding of the 37th International Cosmic Ray Conference (ICRC)*. PoS(ICRC2021)312. 2021.

[55] D. Heck et al. *CORSIKA: A Monte Carlo Code to Simulate Extensive Air Showers*. FZKA-6019. 1998.

[56] F. Schmidt and J. Knapp. *CORSIKA shower images*. https://www-zeuthen.desy.de/~jknapp/fs/showerimages.html. Accessed: August 2021.

[57] R. Engel et al. "The hadronic interaction model Sibyll - past, present and future". In: *EPJ Web Conf. 145 (2017) 08001* (2017). DOI: 10.1051/epjconf/2017/14508001.

[58] F. Riehn et al. "Hadronic interaction model Sibyll 2.3d and extensive air showers". In: *arXiv:1912.03300v3 [hep-ph]* (2020).

[59] S. Ostapchenko. "Hadronic Interactions at Cosmic Ray Energies". In: *Nuclear Physics B - Proceedings Supplements 175-176 (2008), 73-80* (2007). DOI: 10.1016/j.nuclphysbps.2007.10.011.

[60] H.J. Drescher et al. "Parton-based Gribov-Regge Theory". In: *arXiv:hep-ph/0007198v1* (2000).

[61] S. Ostapchenko. "QGSJET-III model: physics and preliminary results". In: *EPJ Web Conf. 208 (2019) 11001, ISVHECRI 2018* (2018).

[62] T. Pierog et al. "EPOS LHC: test of collective hadronization with LHC data". In: *arXiv:1306.0121v2* (2013).

[63] A. A. Alves Jr. “Status of the novel CORSIKA 8 air shower simulation framework”. In: *Proceeding of the 37th International Cosmic Ray Conference (ICRC)*. PoS(ICRC2021)284. 2021.

[64] S. Agostinelli et al. “GEANT4 - a simulation toolkit”. In: *Nuclear Instruments and Methods in Physics Research A 506 (2003) 250-303* (2003). DOI: 10.1016/S0168-9002(03)01368-8.

[65] M.G. Aartsen et al. “Cosmic Ray Spectrum and Composition from PeV to EeV Using 3 Years of Data From IceTop and IceCube”. In: *arXiv:1906.04317v2* (2019).

[66] D. Bindig. “Muon density in extensive air showers measured with IceTop”. PhD thesis. Universität Wuppertal, Germany, 2018.

[67] J.G. Gonzalez. “Measuring the muon content of air showers with IceTop”. In: *EPJ Web Conf. 99 (2015) 06002* (2015). DOI: 10.1051/epjconf/20159906002.

[68] M. Vraeghe. “Muon counting with the IceTop Detector as a Probe of Cosmic Ray Composition”. MA thesis. Universität Ghent, Belgium, 2012.

[69] T.K. Gaisser, T. Stanev, and S. Tilav. “Cosmic Ray Energy Spectrum from Measurementents of Air Showers”. In: *arXiv:1303.3565v1* (2013).

[70] T.K. Gaisser. “Spectrum of cosmic-ray nucleons, kaon production, and the atmospheric muon charge ratio”. In: *Astroparticle Physics 35 (2012) 801-806* (2012).

A. Appendix

A.1. Fitting charge distributions

Dataset (S_{125} cut for exp.)	θ range (°)	r (m)	charge	μ Simulation	μ Experiment
SIBYLL 2.1 H	0 - 18	400	SLC	1.054 ± 0.0	1.1 ± 0.0
			HLC + SLC	1.223 ± 0.025	1.135 ± 0.002
		600	SLC	1.06 ± 0.02	1.01 ± 0.00
			HLC + SLC	1.064 ± 0.008	1.02 ± 0.00
	25.185 - 37	400	SLC	1.18 ± 0.06	1.212 ± 0.003
			HLC + SLC	1.138 ± 0.154	1.238 ± 0.002
		600	SLC	1.172 ± 0.025	1.131 ± 0.004
			HLC + SLC	1.157 ± 0.0	1.137 ± 0.004
SIBYLL 2.1 Fe	0 - 18	400	SLC	1.18 ± 0.02	1.099 ± 0.002
			HLC + SLC	1.163 ± 0.024	1.134 ± 0.002
		600	SLC	1.079 ± 0.054	1.009 ± 0.003
			HLC + SLC	1.049 ± 0.046	1.019 ± 0.003
	25.185 - 37	400	SLC	1.334 ± 0.025	1.2 ± 0.0
			HLC + SLC	1.321 ± 0.022	1.221 ± 0.002
		600	SLC	1.205 ± 0.021	1.129 ± 0.003
			HLC + SLC	1.103 ± 0.081	1.135 ± 0.003
SIBYLL 2.3 H	0 - 18	400	SLC	1.116 ± 0.016	1.104 ± 0.003
			HLC + SLC	1.118 ± 0.014	1.141 ± 0.002
		600	SLC	1.063 ± 0.015	1.011 ± 0.003
			HLC + SLC	1.06 ± 0.02	1.021 ± 0.003
	25.185 - 37	400	SLC	1.24 ± 0.02	1.217 ± 0.004
			HLC + SLC	1.237 ± 0.016	1.245 ± 0.003
		600	SLC	1.161 ± 0.017	1.132 ± 0.004
			HLC + SLC	1.156 ± 0.023	1.139 ± 0.004

Table 3: Results of fitting the charge histograms in simulation and experiment. μ is the fitted x-position of the center of the muon peak in unit VEM.

Dataset (S_{125} cut for exp.)	θ range (°)	r (m)	charge	μ Simulation	μ Experiment
SIBYLL 2.3 Fe	0 - 18	400	SLC	1.141 ± 0.012	1.104 ± 0.003
			HLC + SLC	1.155 ± 0.01	1.141 ± 0.002
		600	SLC	1.086 ± 0.011	1.011 ± 0.003
			HLC + SLC	1.087 ± 0.01	1.022 ± 0.003
	25.185 - 37	400	SLC	1.247 ± 0.011	1.206 ± 0.003
			HLC + SLC	1.264 ± 0.01	1.229 ± 0.002
		600	SLC	1.174 ± 0.014	1.131 ± 0.004
			HLC + SLC	1.178 ± 0.013	1.137 ± 0.003
EPOS-LHC H	0 - 18	400	SLC	1.118 ± 0.019	1.108 ± 0.003
			HLC + SLC	1.14 ± 0.01	1.145 ± 0.002
		600	SLC	1.053 ± 0.016	1.011 ± 0.003
			HLC + SLC	1.029 ± 0.019	1.022 ± 0.003
	25.185 - 37	400	SLC	1.253 ± 0.015	1.219 ± 0.004
			HLC + SLC	1.253 ± 0.013	1.247 ± 0.003
		600	SLC	1.17 ± 0.02	1.133 ± 0.004
			HLC + SLC	1.165 ± 0.021	1.14 ± 0.00
EPOS-LHC Fe	0 - 18	400	SLC	1.167 ± 0.011	1.109 ± 0.003
			HLC + SLC	1.172 ± 0.010	1.147 ± 0.002
		600	SLC	1.079 ± 0.011	1.012 ± 0.003
			HLC + SLC	1.081 ± 0.011	1.023 ± 0.003
	25.185 - 37	400	SLC	1.248 ± 0.014	1.207 ± 0.003
			HLC + SLC	1.245 ± 0.012	1.231 ± 0.003
		600	SLC	1.162 ± 0.019	1.131 ± 0.004
			HLC + SLC	1.172 ± 0.016	1.138 ± 0.003
QGSJet-II 04 H	0 - 18	400	SLC	1.133 ± 0.15	1.104 ± 0.003
			HLC + SLC	1.142 ± 0.015	1.141 ± 0.002
		600	SLC	1.07 ± 0.02	1.011 ± 0.003
			HLC + SLC	1.05 ± 0.02	1.021 ± 0.003
	25.185 - 37	400	SLC	1.265 ± 0.017	1.215 ± 0.004
			HLC + SLC	1.262 ± 0.015	1.242 ± 0.003
		600	SLC	1.132 ± 0.025	1.132 ± 0.004
			HLC + SLC	1.138 ± 0.031	1.139 ± 0.004

Table 3: Results of fitting the charge histograms in simulation and experiment. μ is the fitted x-position of the center of the muon peak in unit VEM.

Dataset ($\mathbf{S_{125}}$ **cut for exp.**)	θ **range (°)**	**r (m)**	**charge**	μ **Simulation**	μ **Experiment**
QGSJet-II 04 Fe	0 - 18	400	SLC	1.15 ± 0.01	1.103 ± 0.003
			HLC + SLC	1.159 ± 0.011	1.14 ± 0.00
		600	SLC	1.065 ± 0.011	1.011 ± 0.003
			HLC + SLC	1.063 ± 0.011	1.022 ± 0.003
	25.185 - 37	400	SLC	1.241 ± 0.013	1.203 ± 0.003
			HLC + SLC	1.246 ± 0.012	1.225 ± 0.002
		600	SLC	1.179 ± 0.019	1.13 ± 0.0
			HLC + SLC	1.183 ± 0.016	1.137 ± 0.003

Table 3: Continuation of the results of fitting the charge histograms in simulation and experiment. μ is the fitted x-position of the center of the muon peak in unit VEM.

Fit on experimental data

HLC + SLC charge for r_1 and θ_1

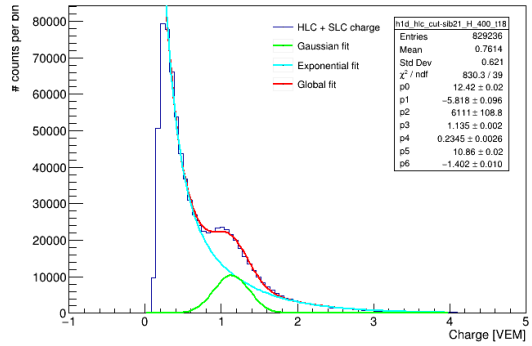

HLC + SLC charge for r_1 and θ_2

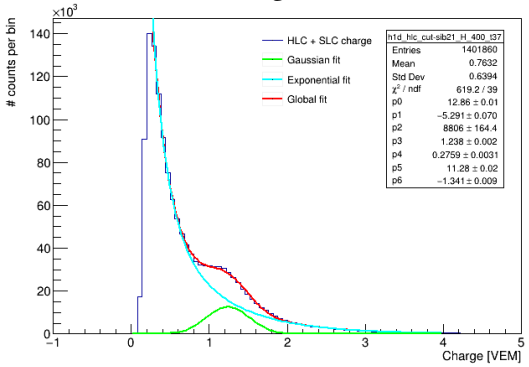

HLC + SLC charge for r_2 and θ_1

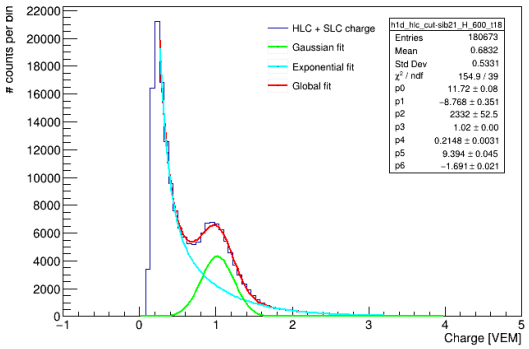

HLC + SLC charge for r_2 and θ_2

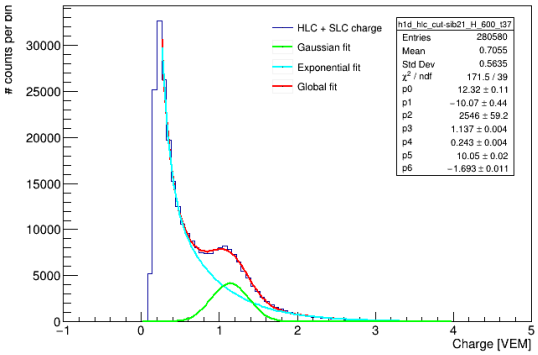

SLC charge for r_1 and θ_1

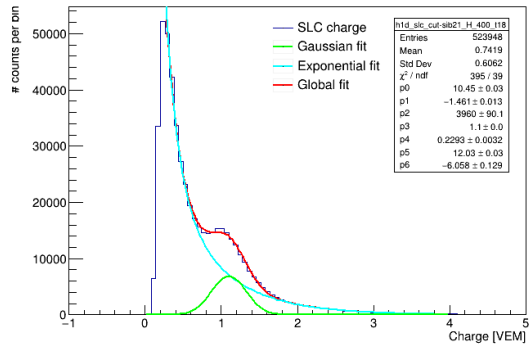

SLC charge for r_1 and θ_2

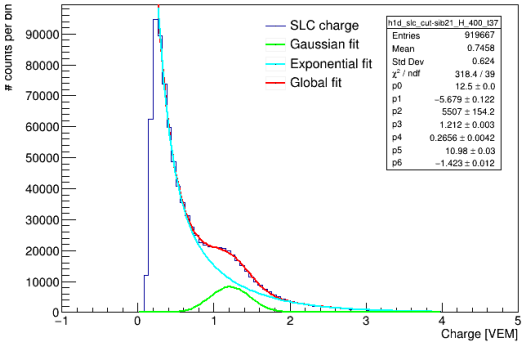

SLC charge for r_2 and θ_1

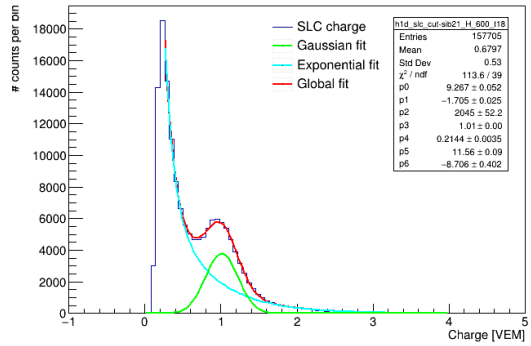

SLC charge for r_2 and θ_2

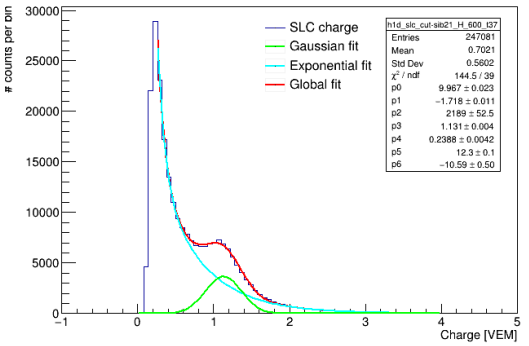

Fit on simulation - SIBYLL 2.1 H

HLC + SLC charge for r_1 and θ_1

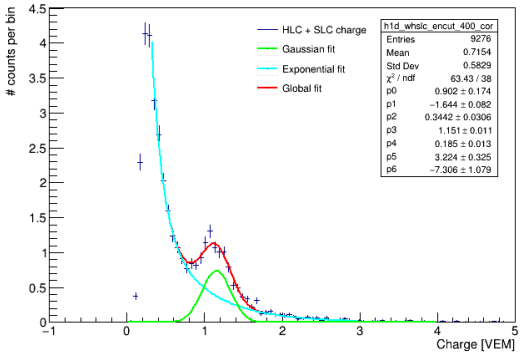

HLC + SLC charge for r_1 and θ_2

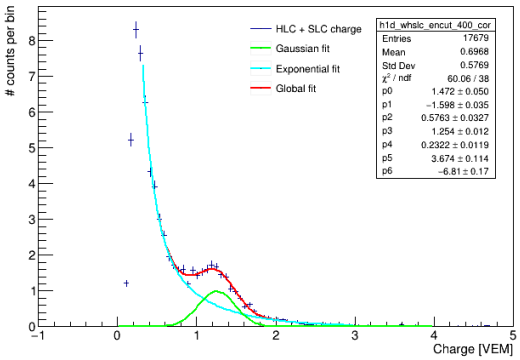

HLC + SLC charge for r_2 and θ_1

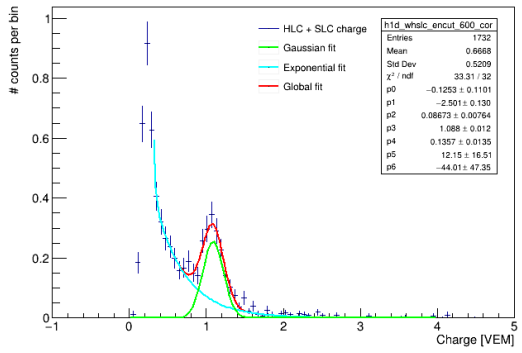

HLC + SLC charge for r_2 and θ_2

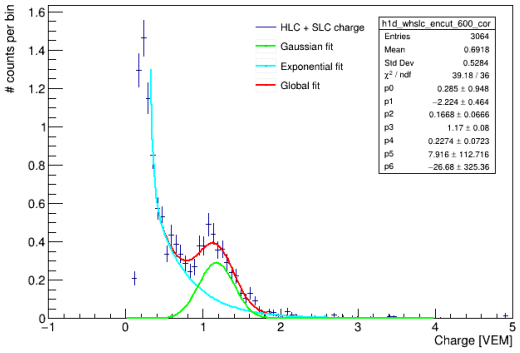

SLC charge for r_1 and θ_1

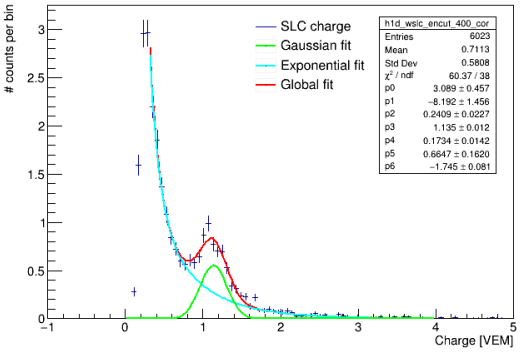

SLC charge for r_1 and θ_2

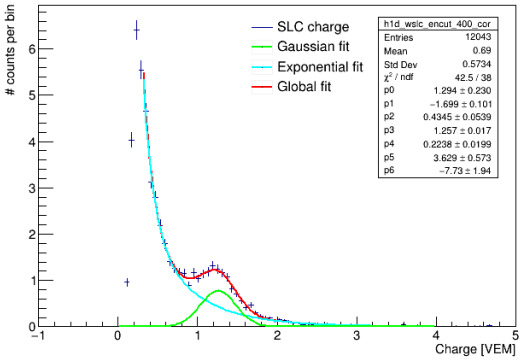

SLC charge for r_2 and θ_1

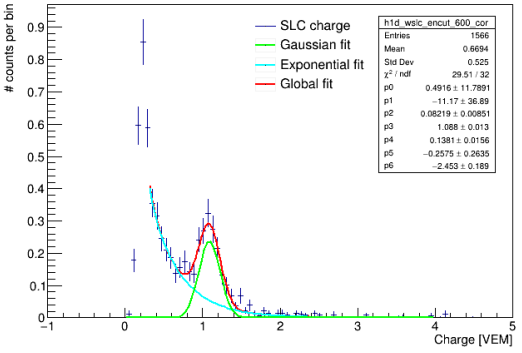

SLC charge for r_2 and θ_2

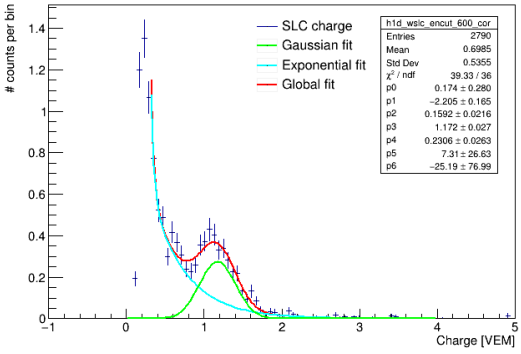

Fit on simulation - SIBYLL 2.1 Fe

HLC + SLC charge for r_1 and θ_1

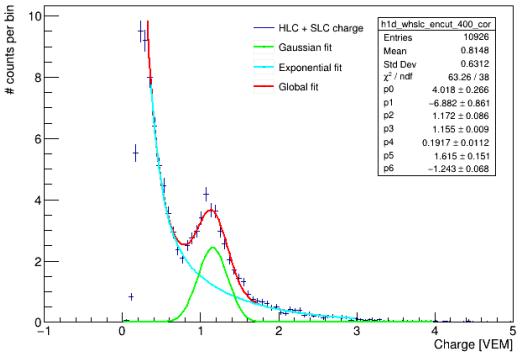

HLC + SLC charge for r_1 and θ_2

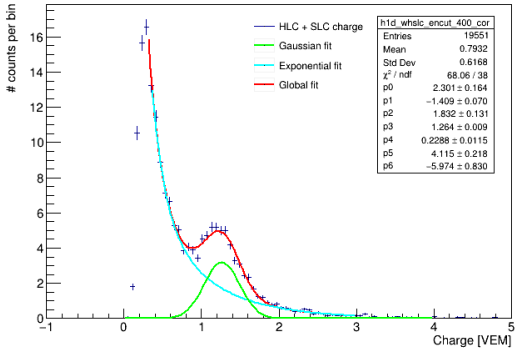

HLC + SLC charge for r_2 and θ_1

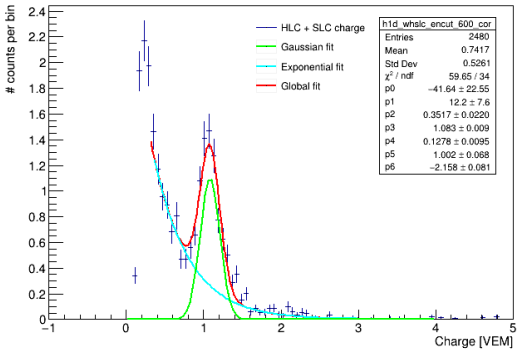

HLC + SLC charge for r_2 and θ_2

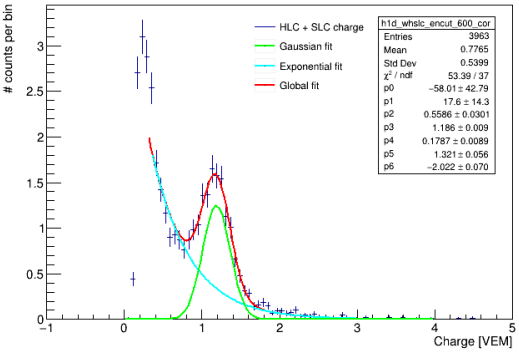

SLC charge for r_1 and θ_1

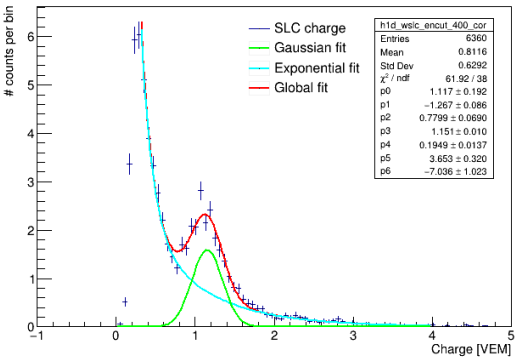

SLC charge for r_1 and θ_2

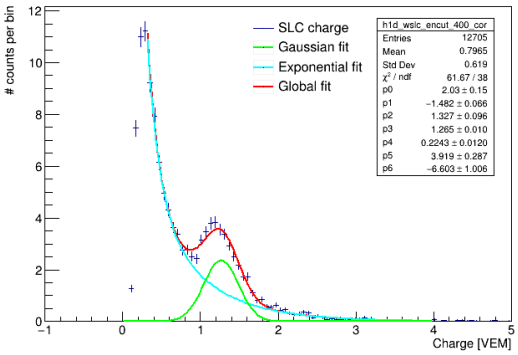

SLC charge for r_2 and θ_1

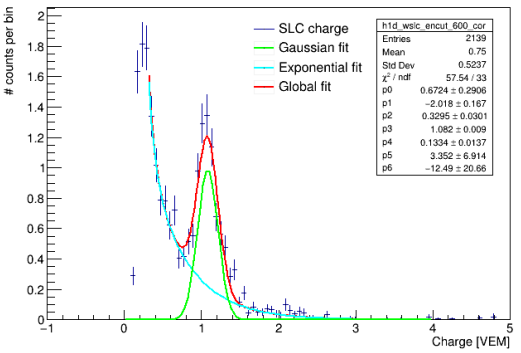

SLC charge for r_2 and θ_2

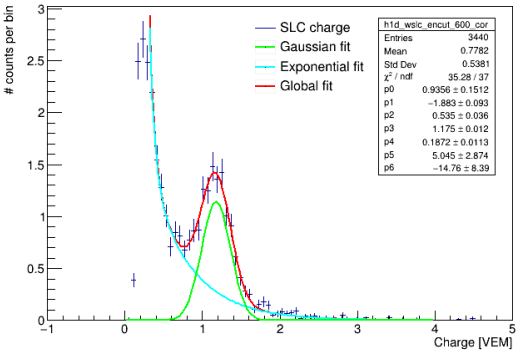

Fit on simulation - SIBYLL 2.3 H

HLC + SLC charge for r_1 and θ_1

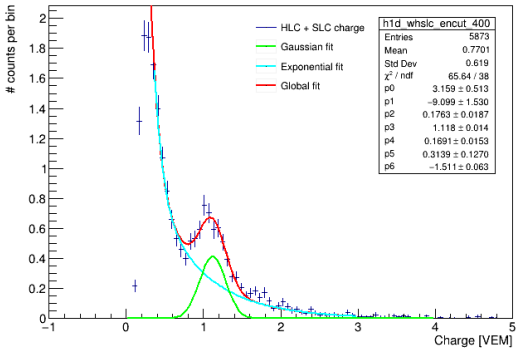

HLC + SLC charge for r_1 and θ_2

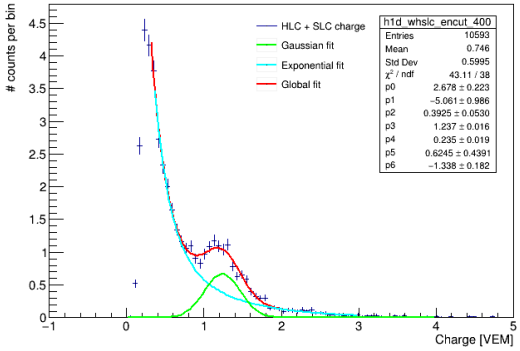

HLC + SLC charge for r_2 and θ_1

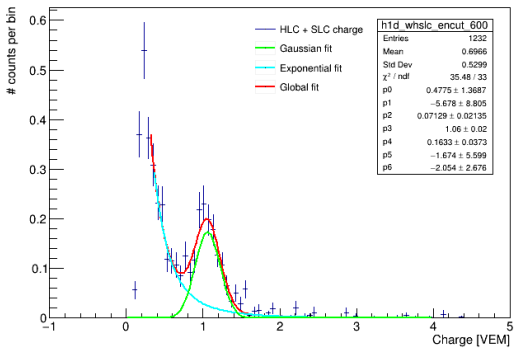

HLC + SLC charge for r_2 and θ_2

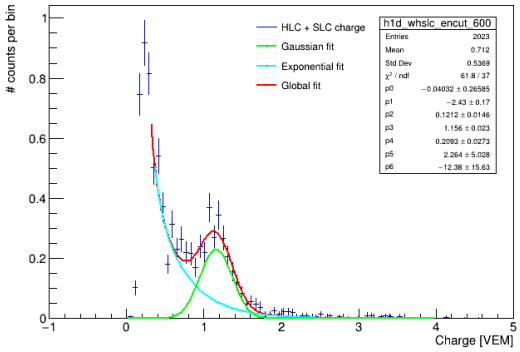

SLC charge for r_1 and θ_1

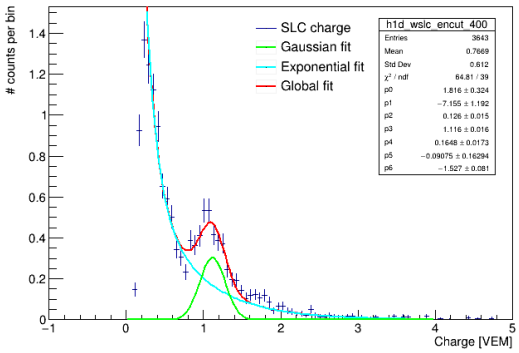

SLC charge for r_1 and θ_2

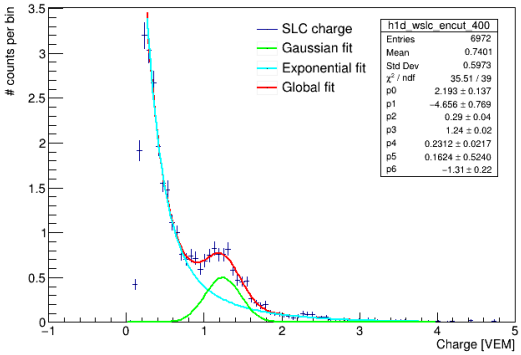

SLC charge for r_2 and θ_1

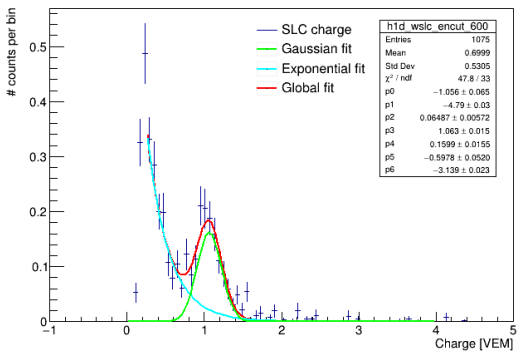

SLC charge for r_2 and θ_2

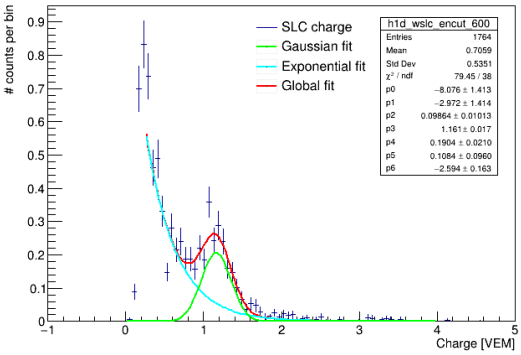

Fit on simulation - SIBYLL 2.3 Fe

HLC + SLC charge for r_1 and θ_1

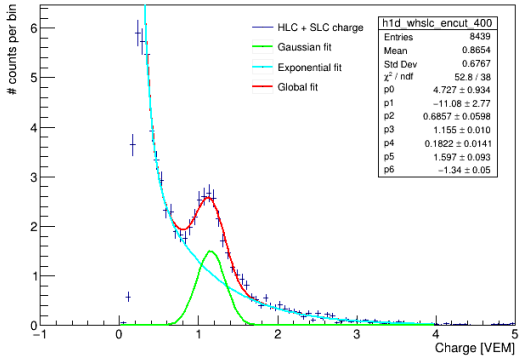

HLC + SLC charge for r_1 and θ_2

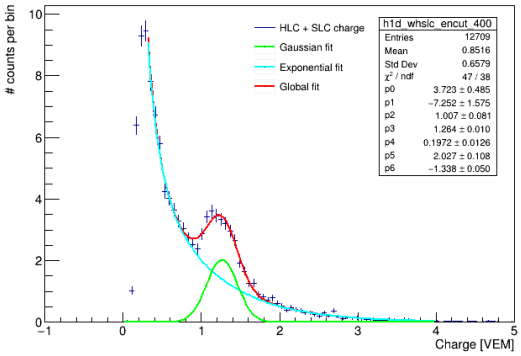

HLC + SLC charge for r_2 and θ_1

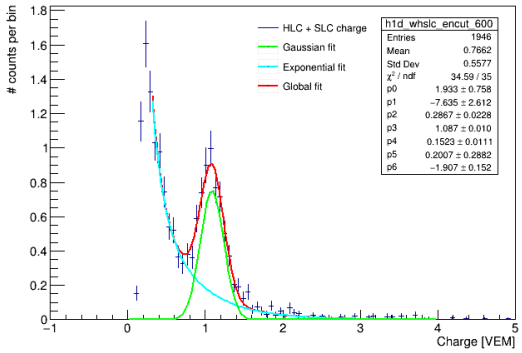

HLC + SLC charge for r_2 and θ_2

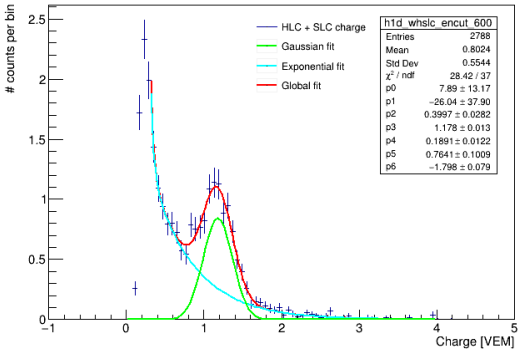

SLC charge for r_1 and θ_1

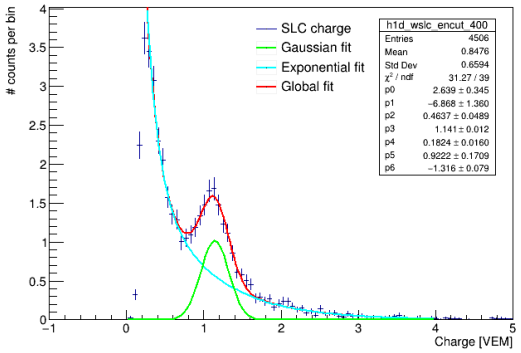

SLC charge for r_1 and θ_2

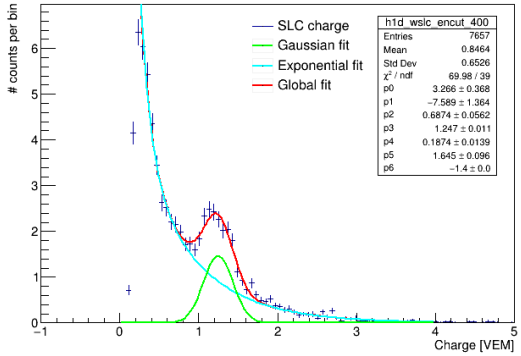

SLC charge for r_2 and θ_1

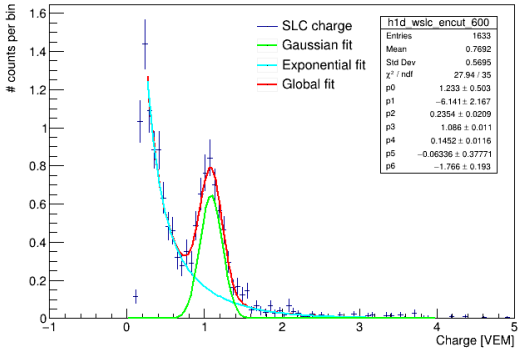

SLC charge for r_2 and θ_2

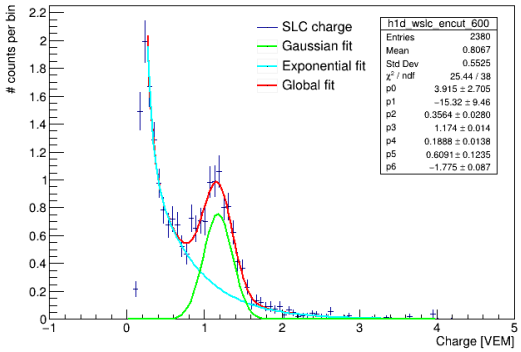

Fit on simulation - EPOS-LHC H

HLC + SLC charge for r_1 and θ_1

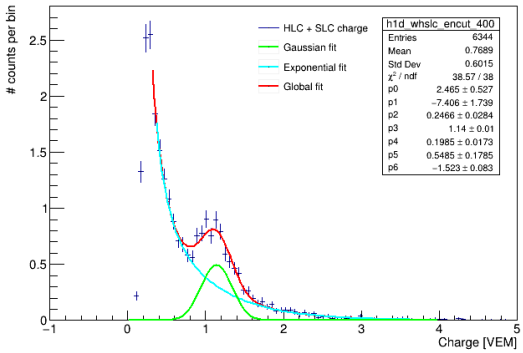

HLC + SLC charge for r_1 and θ_2

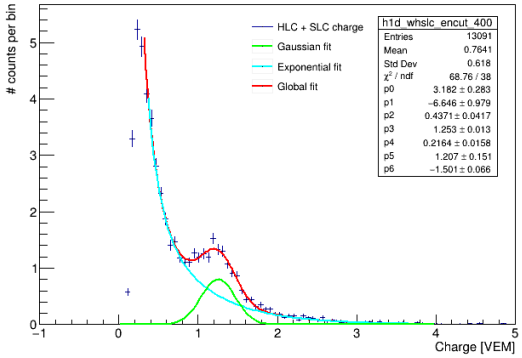

HLC + SLC charge for r_2 and θ_1

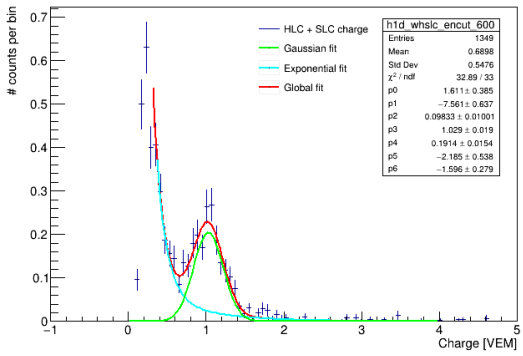

HLC + SLC charge for r_2 and θ_2

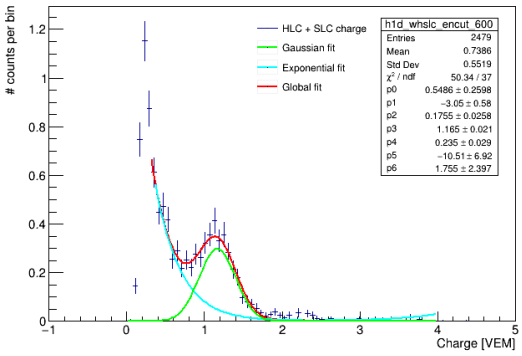

SLC charge for r_1 and θ_1

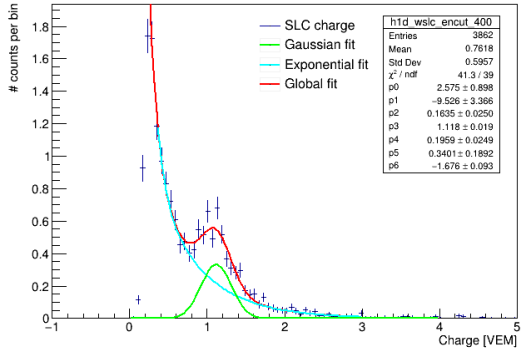

SLC charge for r_1 and θ_2

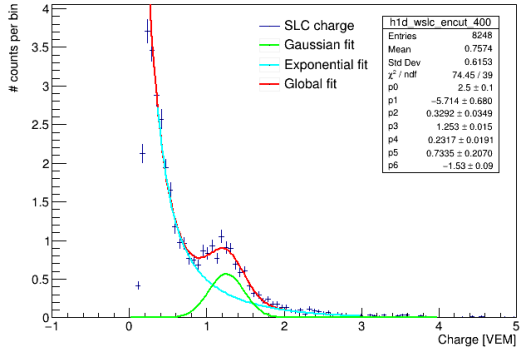

SLC charge for r_2 and θ_1

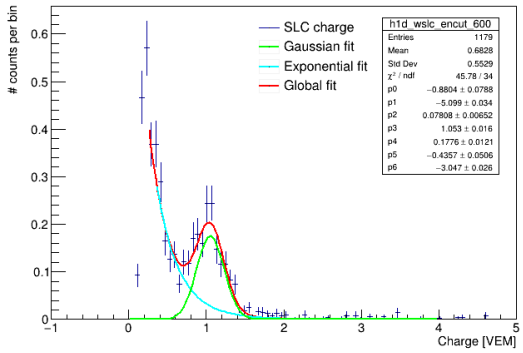

SLC charge for r_2 and θ_2

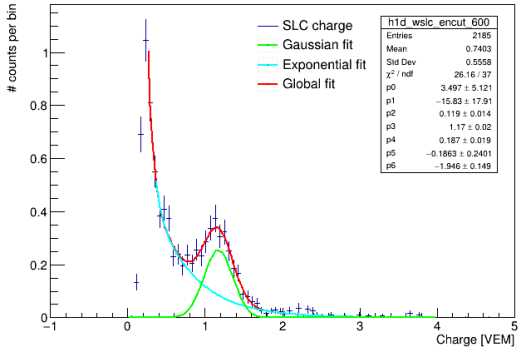

Fit on simulation - EPOS-LHC Fe

HLC + SLC charge for r_1 and θ_1

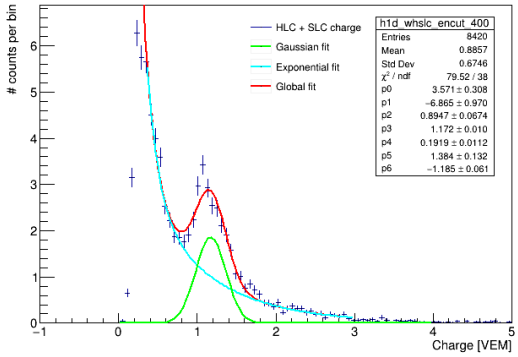

HLC + SLC charge for r_1 and θ_2

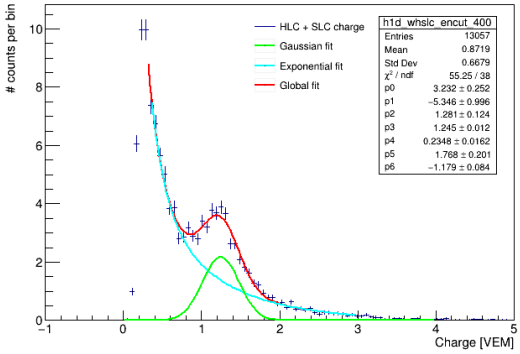

HLC + SLC charge for r_2 and θ_1

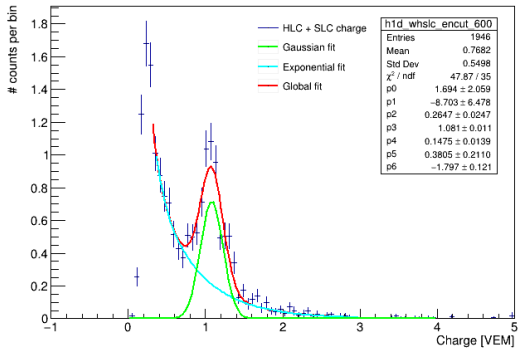

HLC + SLC charge for r_2 and θ_2

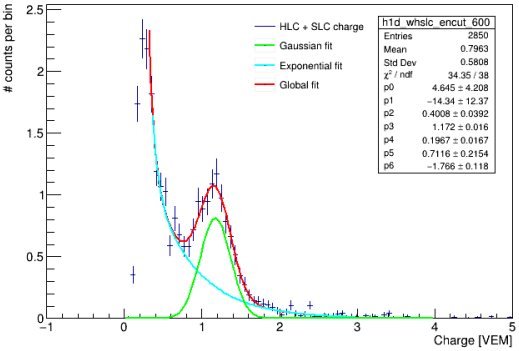

SLC charge for r_1 and θ_1

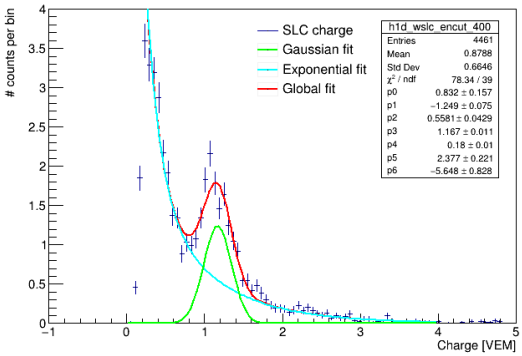

SLC charge for r_1 and θ_2

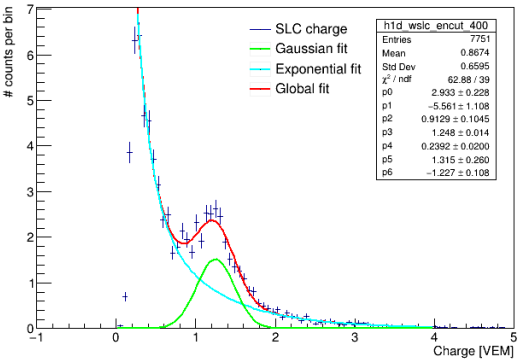

SLC charge for r_2 and θ_1

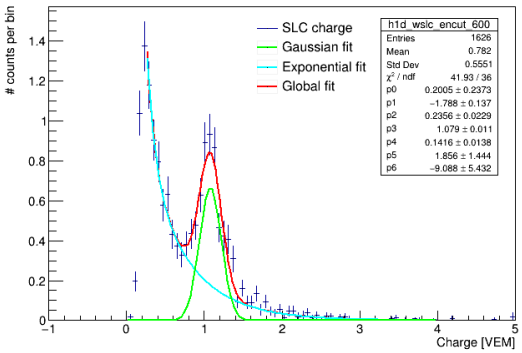

SLC charge for r_2 and θ_2

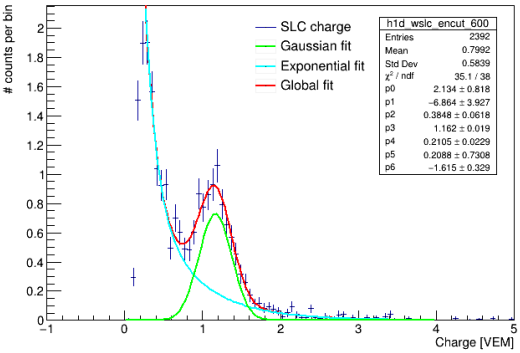

Fit on simulation - QGSJet-II 04 H

HLC + SLC charge for r_1 and θ_1

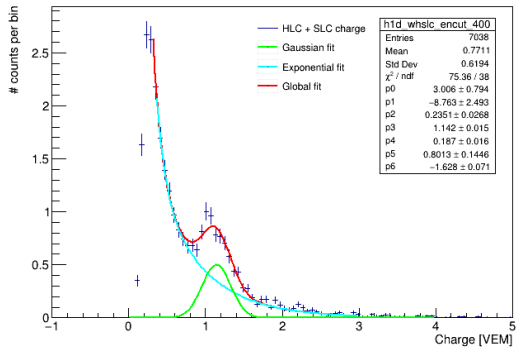

HLC + SLC charge for r_1 and θ_2

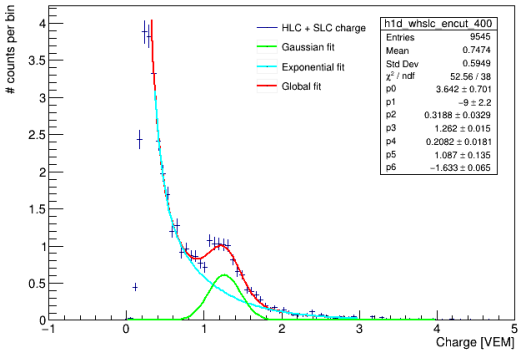

HLC + SLC charge for r_2 and θ_1

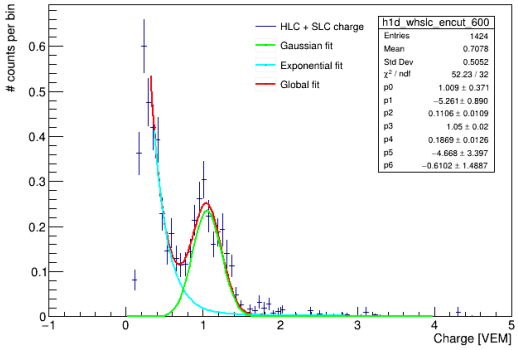

HLC + SLC charge for r_2 and θ_2

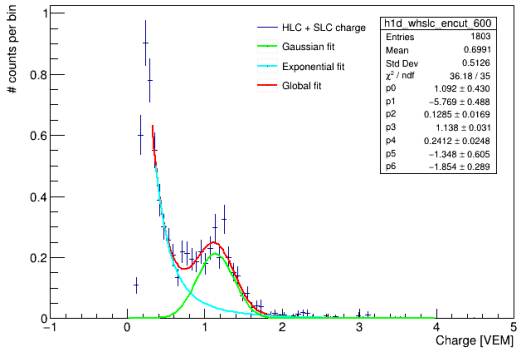

SLC charge for r_1 and θ_1

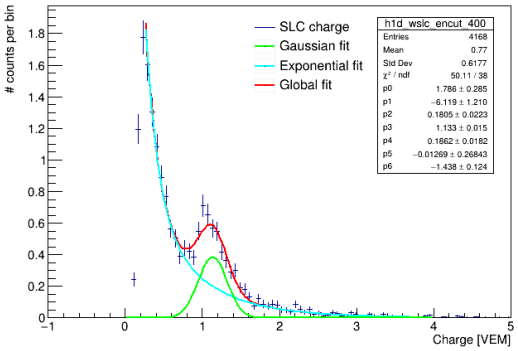

SLC charge for r_1 and θ_2

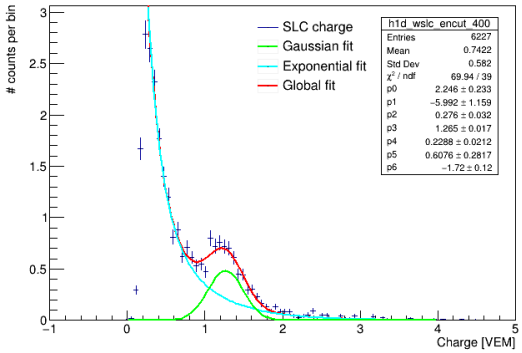

SLC charge for r_2 and θ_1

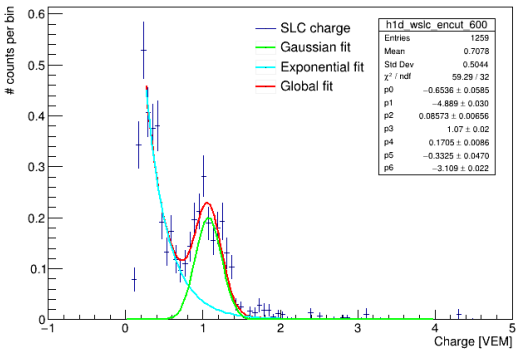

SLC charge for r_2 and θ_2

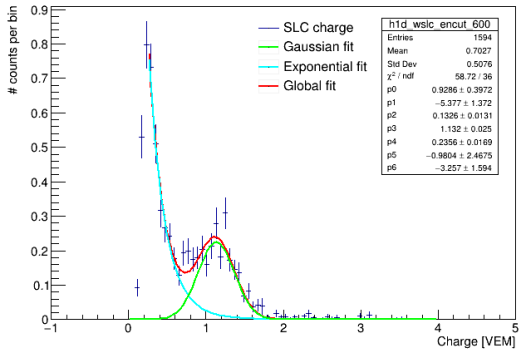

Fit on simulation - QGSJet-II 04 Fe

HLC + SLC charge for r_1 and θ_1

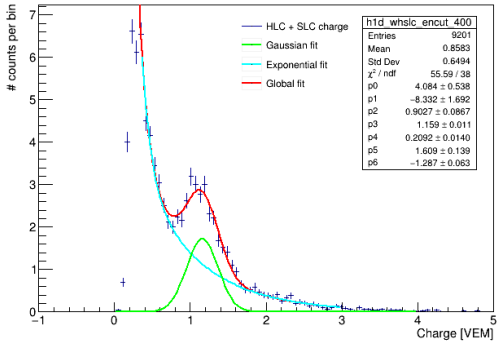

HLC + SLC charge for r_1 and θ_2

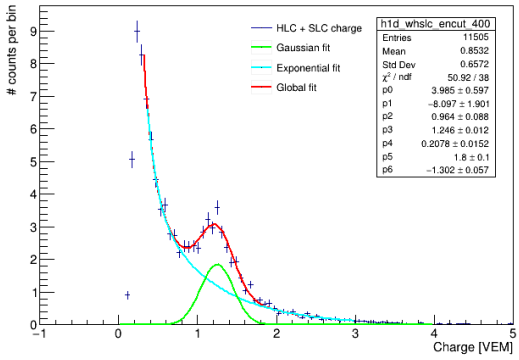

HLC + SLC charge for r_2 and θ_1

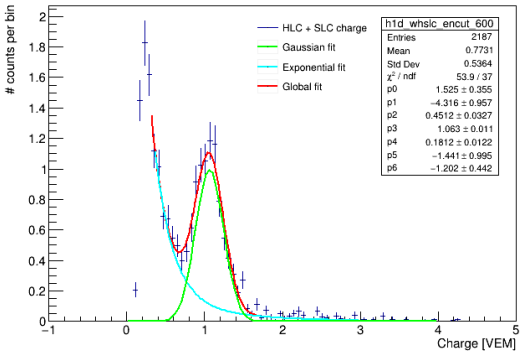

HLC + SLC charge for r_2 and θ_2

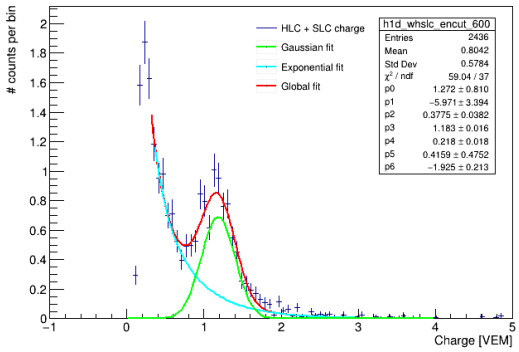

SLC charge for r_1 and θ_1

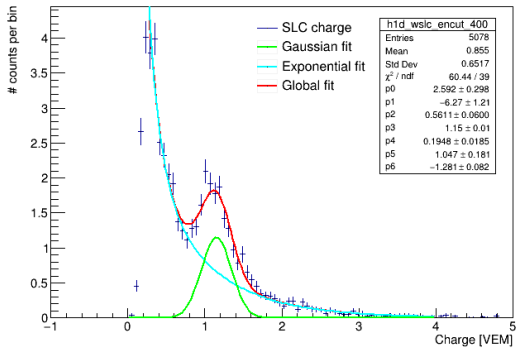

SLC charge for r_1 and θ_2

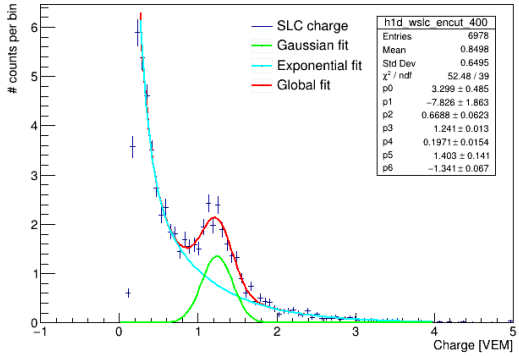

SLC charge for r_2 and θ_1

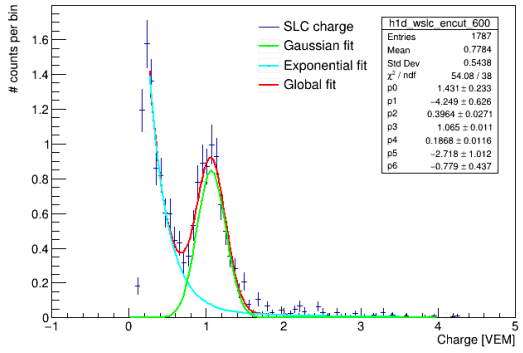

SLC charge for r_2 and θ_2

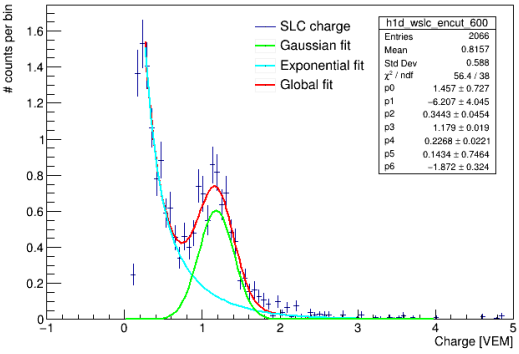

A.2. Comparing experimental with simulated distributions

A.2.1. Ratio plots with either H or Fe primary

This chapter shows the distributions and ratio plots of the comparison of simulated charge distributions with the experimental charge distributions from 2012 for both, SLC and HLC + SLC charge. The simulated distribution is either using H or Fe primaries. The r- and θ-cuts as well as the simulation model are written on top of the histograms or in their information boxes.
The ratio plots containing H- and Fe-distributions are plotted in the next Subsection A.2.2.

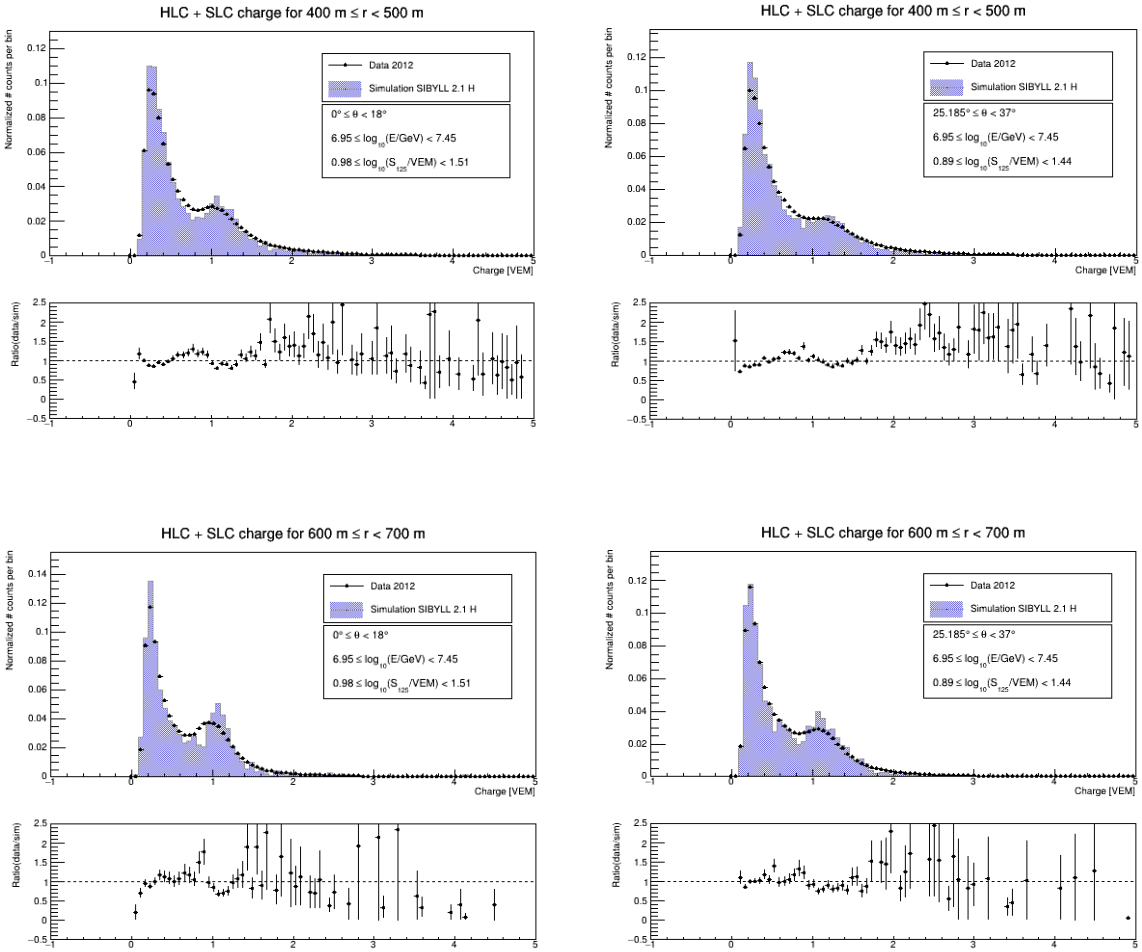

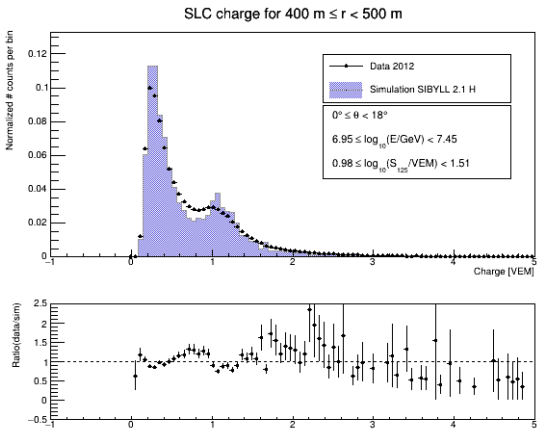
SLC charge for 400 m ≤ r < 500 m
Data 2012
Simulation SIBYLL 2.1 H
0° ≤ θ < 18°
6.95 ≤ log10(E/GeV) < 7.45
0.98 ≤ log10(S125/VEM) < 1.51
Normalized # counts per bin
Charge [VEM]
Ratio(data/sim)

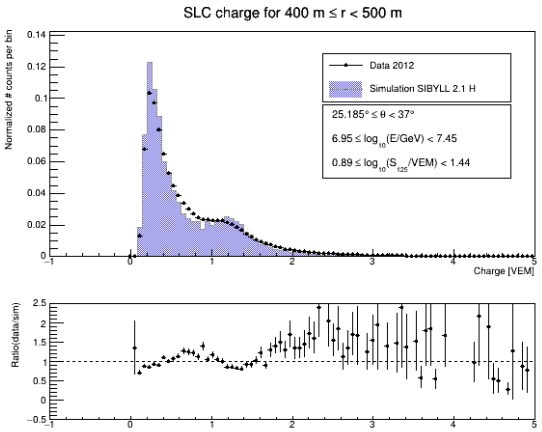
SLC charge for 400 m ≤ r < 500 m
Data 2012
Simulation SIBYLL 2.1 H
25.185° ≤ θ < 37°
6.95 ≤ log10(E/GeV) < 7.45
0.89 ≤ log10(S125/VEM) < 1.44
Normalized # counts per bin
Charge [VEM]
Ratio(data/sim)

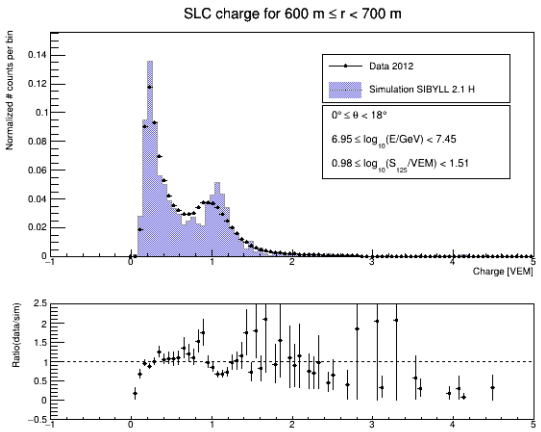
SLC charge for 600 m ≤ r < 700 m
Data 2012
Simulation SIBYLL 2.1 H
0° ≤ θ < 18°
6.95 ≤ log10(E/GeV) < 7.45
0.98 ≤ log10(S125/VEM) < 1.51
Normalized # counts per bin
Charge [VEM]
Ratio(data/sim)

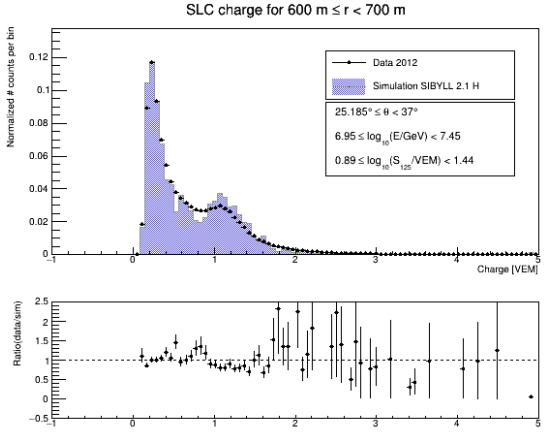
SLC charge for 600 m ≤ r < 700 m
Data 2012
Simulation SIBYLL 2.1 H
25.185° ≤ θ < 37°
6.95 ≤ log10(E/GeV) < 7.45
0.89 ≤ log10(S125/VEM) < 1.44
Normalized # counts per bin
Charge [VEM]
Ratio(data/sim)

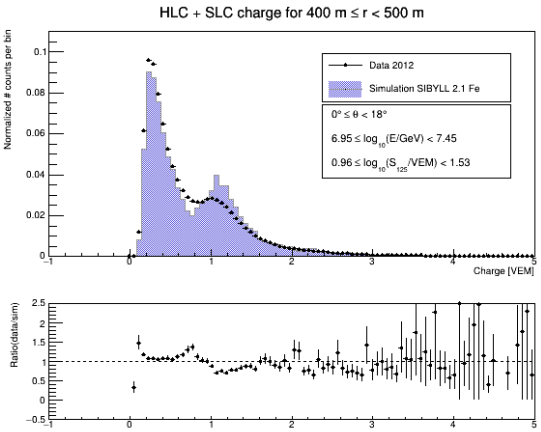
HLC + SLC charge for 400 m ≤ r < 500 m
Data 2012
Simulation SIBYLL 2.1 Fe
0° ≤ θ < 18°
6.95 ≤ log10(E/GeV) < 7.45
0.96 ≤ log10(S125/VEM) < 1.53
Normalized # counts per bin
Charge [VEM]
Ratio(data/sim)

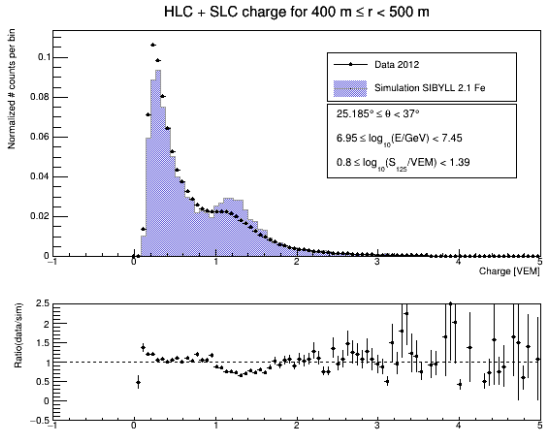
HLC + SLC charge for 400 m ≤ r < 500 m
Data 2012
Simulation SIBYLL 2.1 Fe
25.185° ≤ θ < 37°
6.95 ≤ log10(E/GeV) < 7.45
0.8 ≤ log10(S125/VEM) < 1.39
Normalized # counts per bin
Charge [VEM]
Ratio(data/sim)

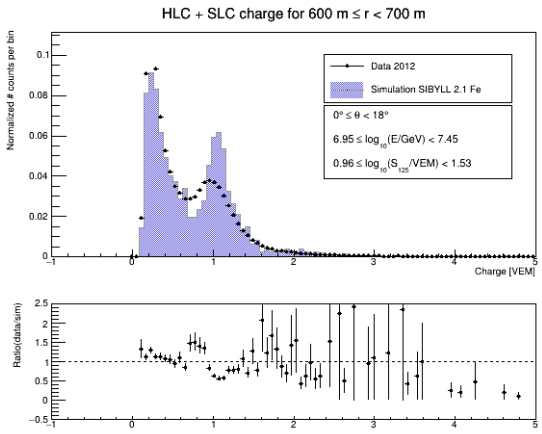
HLC + SLC charge for 600 m ≤ r < 700 m
Data 2012
Simulation SIBYLL 2.1 Fe
0° ≤ θ < 18°
6.95 ≤ log10(E/GeV) < 7.45
0.96 ≤ log10(S125/VEM) < 1.53
Normalized # counts per bin
Charge [VEM]
Ratio(data/sim)

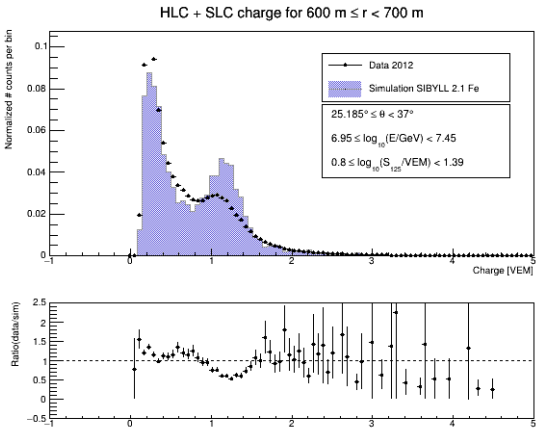
HLC + SLC charge for 600 m ≤ r < 700 m
Data 2012
Simulation SIBYLL 2.1 Fe
25.185° ≤ θ < 37°
6.95 ≤ log10(E/GeV) < 7.45
0.8 ≤ log10(S125/VEM) < 1.39
Normalized # counts per bin
Charge [VEM]
Ratio(data/sim)

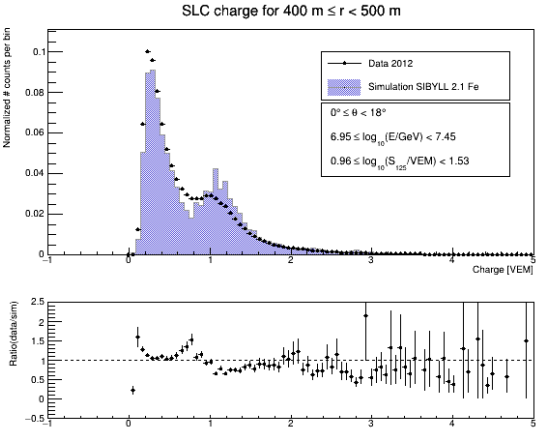
SLC charge for 400 m ≤ r < 500 m
Data 2012
Simulation SIBYLL 2.1 Fe
0° ≤ θ < 18°
6.95 ≤ log10(E/GeV) < 7.45
0.96 ≤ log10(S125/VEM) < 1.53
Normalized # counts per bin
Charge [VEM]
Ratio(data/sim)

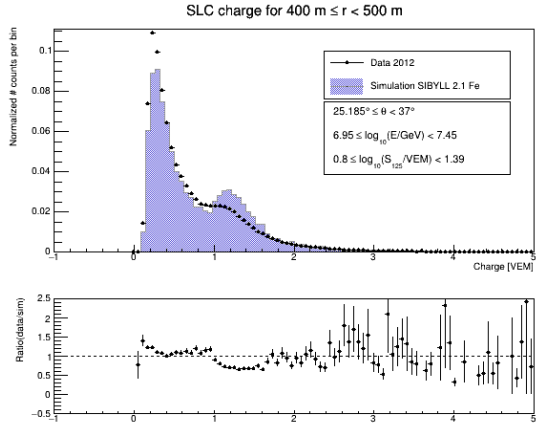
SLC charge for 400 m ≤ r < 500 m
Data 2012
Simulation SIBYLL 2.1 Fe
25.185° ≤ θ < 37°
6.95 ≤ log10(E/GeV) < 7.45
0.8 ≤ log10(S125/VEM) < 1.39
Normalized # counts per bin
Charge [VEM]
Ratio(data/sim)

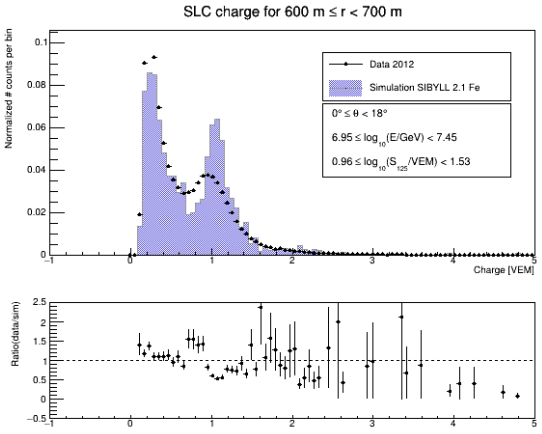
SLC charge for 600 m ≤ r < 700 m
Data 2012
Simulation SIBYLL 2.1 Fe
0° ≤ θ < 18°
6.95 ≤ log10(E/GeV) < 7.45
0.96 ≤ log10(S125/VEM) < 1.53
Normalized # counts per bin
Charge [VEM]
Ratio(data/sim)

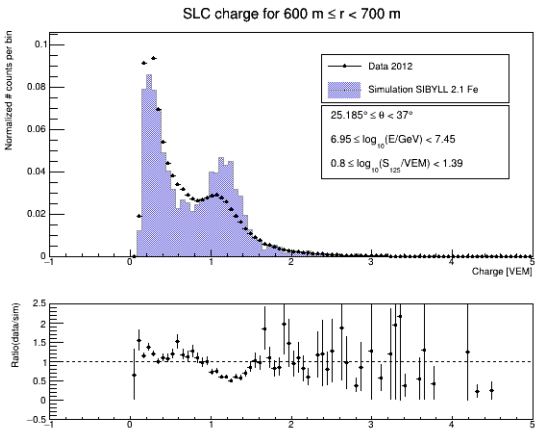
SLC charge for 600 m ≤ r < 700 m
Data 2012
Simulation SIBYLL 2.1 Fe
25.185° ≤ θ < 37°
6.95 ≤ log10(E/GeV) < 7.45
0.8 ≤ log10(S125/VEM) < 1.39
Normalized # counts per bin
Charge [VEM]
Ratio(data/sim)

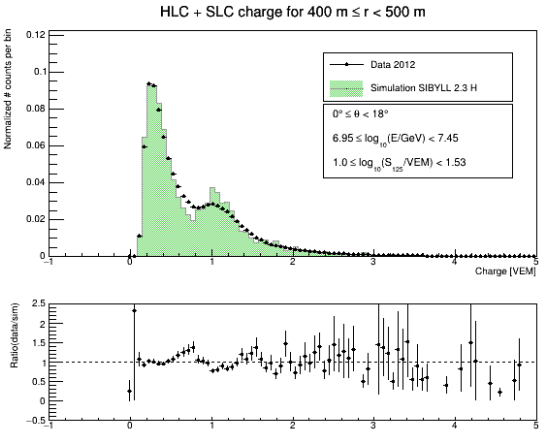
HLC + SLC charge for 400 m ≤ r < 500 m
Data 2012
Simulation SIBYLL 2.3 H
0° ≤ θ < 18°
6.95 ≤ log10(E/GeV) < 7.45
1.0 ≤ log10(S125/VEM) < 1.53
Normalized # counts per bin
Charge [VEM]
Ratio(data/sim)

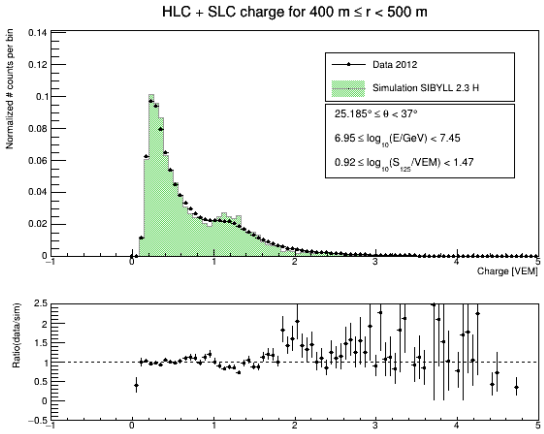
HLC + SLC charge for 400 m ≤ r < 500 m
Data 2012
Simulation SIBYLL 2.3 H
25.185° ≤ θ < 37°
6.95 ≤ log10(E/GeV) < 7.45
0.92 ≤ log10(S125/VEM) < 1.47
Normalized # counts per bin
Charge [VEM]
Ratio(data/sim)

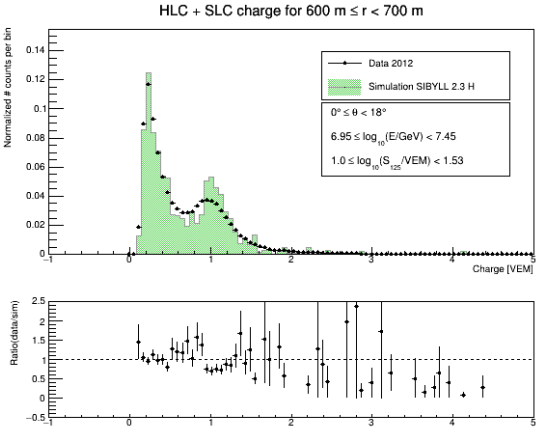
HLC + SLC charge for 600 m ≤ r < 700 m
Data 2012
Simulation SIBYLL 2.3 H
0° ≤ θ < 18°
6.95 ≤ log10(E/GeV) < 7.45
1.0 ≤ log10(S125/VEM) < 1.53
Normalized # counts per bin
Charge [VEM]
Ratio(data/sim)

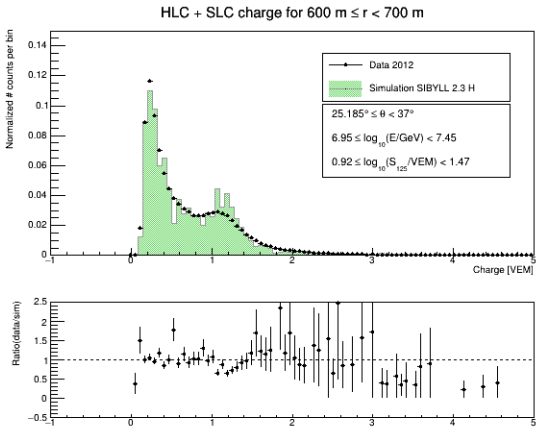
HLC + SLC charge for 600 m ≤ r < 700 m
Data 2012
Simulation SIBYLL 2.3 H
25.185° ≤ θ < 37°
6.95 ≤ log10(E/GeV) < 7.45
0.92 ≤ log10(S125/VEM) < 1.47
Normalized # counts per bin
Charge [VEM]
Ratio(data/sim)

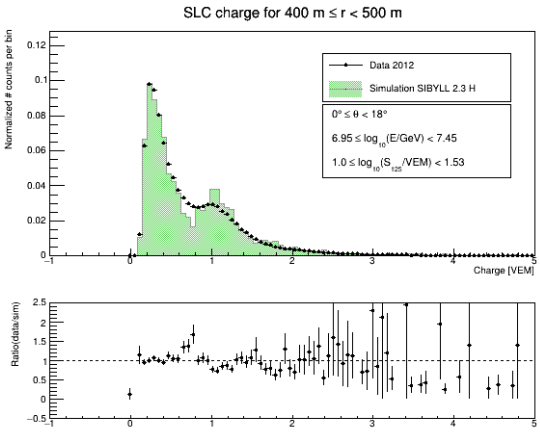
SLC charge for 400 m ≤ r < 500 m
Data 2012
Simulation SIBYLL 2.3 H
0° ≤ θ < 18°
6.95 ≤ log10(E/GeV) < 7.45
1.0 ≤ log10(S125/VEM) < 1.53
Normalized # counts per bin
Charge [VEM]
Ratio(data/sim)

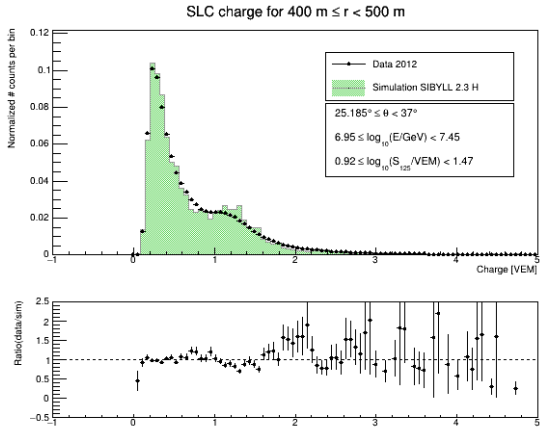
SLC charge for 400 m ≤ r < 500 m
Data 2012
Simulation SIBYLL 2.3 H
25.185° ≤ θ < 37°
6.95 ≤ log10(E/GeV) < 7.45
0.92 ≤ log10(S125/VEM) < 1.47
Normalized # counts per bin
Charge [VEM]
Ratio(data/sim)

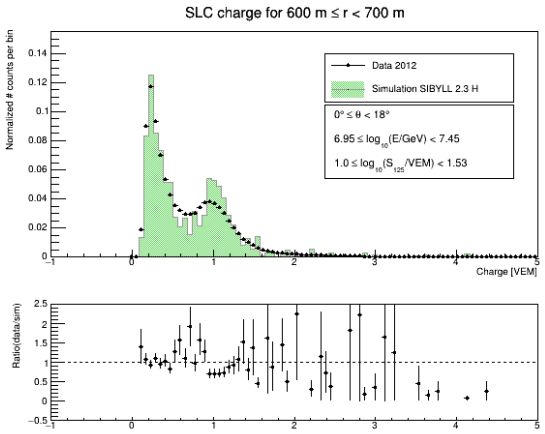
SLC charge for 600 m ≤ r < 700 m
Normalized # counts per bin
Data 2012
Simulation SIBYLL 2.3 H
0° ≤ θ < 18°
6.95 ≤ log10(E/GeV) < 7.45
1.0 ≤ log10(S125/VEM) < 1.53
Charge [VEM]
Ratio(data/sim)

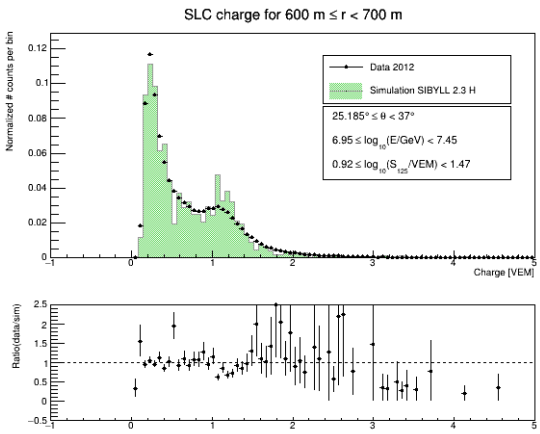
SLC charge for 600 m ≤ r < 700 m
Normalized # counts per bin
Data 2012
Simulation SIBYLL 2.3 H
25.185° ≤ θ < 37°
6.95 ≤ log10(E/GeV) < 7.45
0.92 ≤ log10(S125/VEM) < 1.47
Charge [VEM]
Ratio(data/sim)

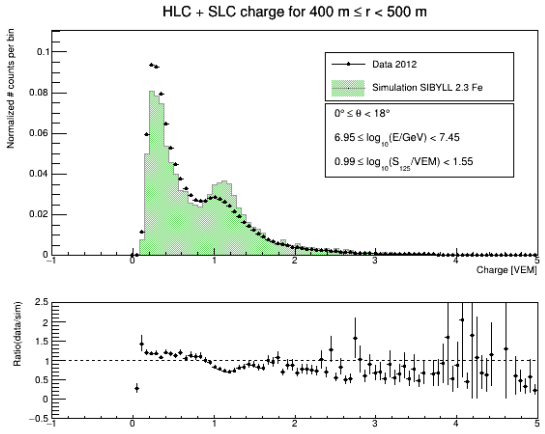
HLC + SLC charge for 400 m ≤ r < 500 m
Normalized # counts per bin
Data 2012
Simulation SIBYLL 2.3 Fe
0° ≤ θ < 18°
6.95 ≤ log10(E/GeV) < 7.45
0.99 ≤ log10(S125/VEM) < 1.55
Charge [VEM]
Ratio(data/sim)

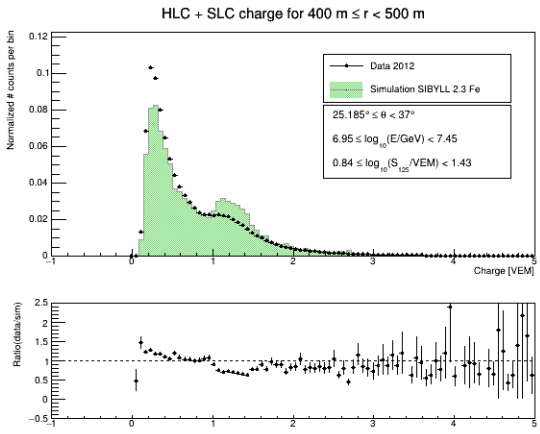
HLC + SLC charge for 400 m ≤ r < 500 m
Normalized # counts per bin
Data 2012
Simulation SIBYLL 2.3 Fe
25.185° ≤ θ < 37°
6.95 ≤ log10(E/GeV) < 7.45
0.84 ≤ log10(S125/VEM) < 1.43
Charge [VEM]
Ratio(data/sim)

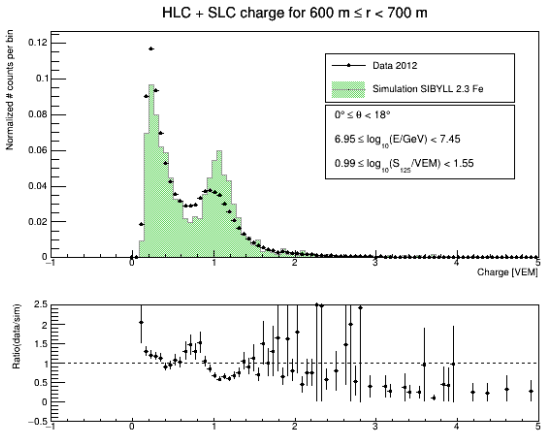
HLC + SLC charge for 600 m ≤ r < 700 m
Normalized # counts per bin
Data 2012
Simulation SIBYLL 2.3 Fe
0° ≤ θ < 18°
6.95 ≤ log10(E/GeV) < 7.45
0.99 ≤ log10(S125/VEM) < 1.55
Charge [VEM]
Ratio(data/sim)

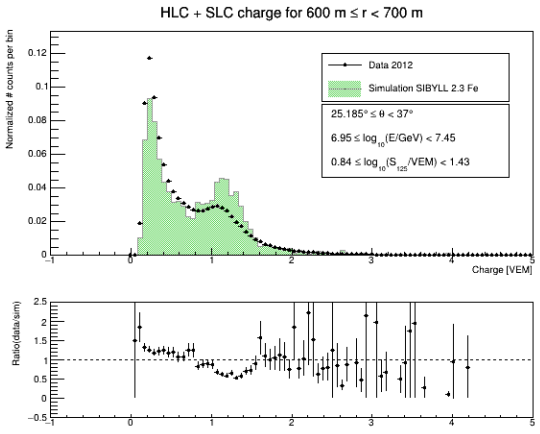
HLC + SLC charge for 600 m ≤ r < 700 m
Normalized # counts per bin
Data 2012
Simulation SIBYLL 2.3 Fe
25.185° ≤ θ < 37°
6.95 ≤ log10(E/GeV) < 7.45
0.84 ≤ log10(S125/VEM) < 1.43
Charge [VEM]
Ratio(data/sim)

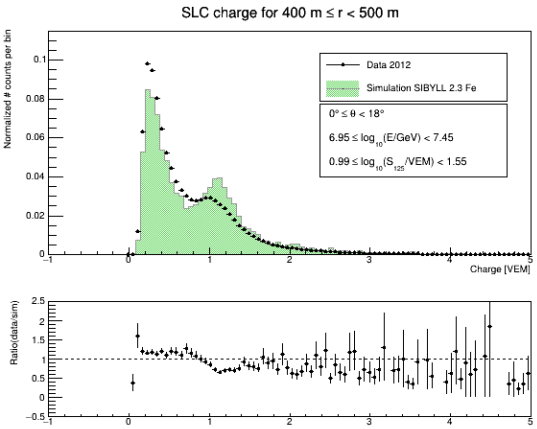
SLC charge for 400 m ≤ r < 500 m
Data 2012
Simulation SIBYLL 2.3 Fe
0° ≤ θ < 18°
6.95 ≤ log10(E/GeV) < 7.45
0.99 ≤ log10(S125/VEM) < 1.55
Normalized # counts per bin
Charge [VEM]
Ratio(data/sim)

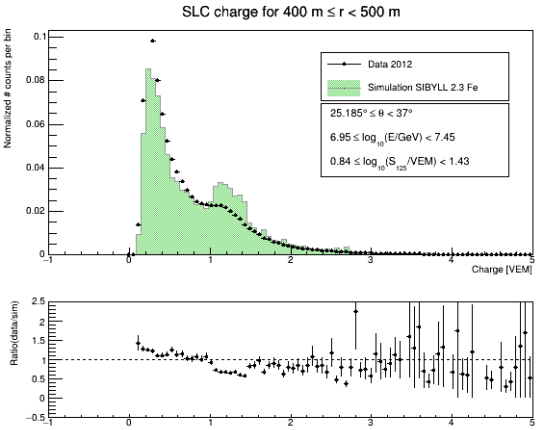
SLC charge for 400 m ≤ r < 500 m
Data 2012
Simulation SIBYLL 2.3 Fe
25.185° ≤ θ < 37°
6.95 ≤ log10(E/GeV) < 7.45
0.84 ≤ log10(S125/VEM) < 1.43
Normalized # counts per bin
Charge [VEM]
Ratio(data/sim)

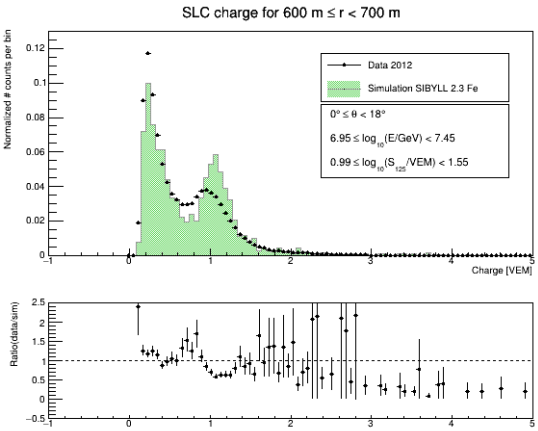
SLC charge for 600 m ≤ r < 700 m
Data 2012
Simulation SIBYLL 2.3 Fe
0° ≤ θ < 18°
6.95 ≤ log10(E/GeV) < 7.45
0.99 ≤ log10(S125/VEM) < 1.55
Normalized # counts per bin
Charge [VEM]
Ratio(data/sim)

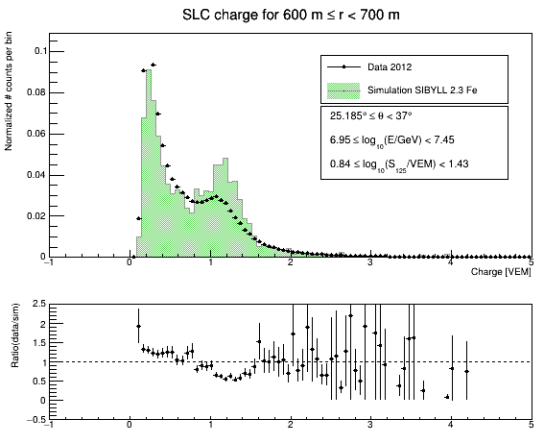
SLC charge for 600 m ≤ r < 700 m
Data 2012
Simulation SIBYLL 2.3 Fe
25.185° ≤ θ < 37°
6.95 ≤ log10(E/GeV) < 7.45
0.84 ≤ log10(S125/VEM) < 1.43
Normalized # counts per bin
Charge [VEM]
Ratio(data/sim)

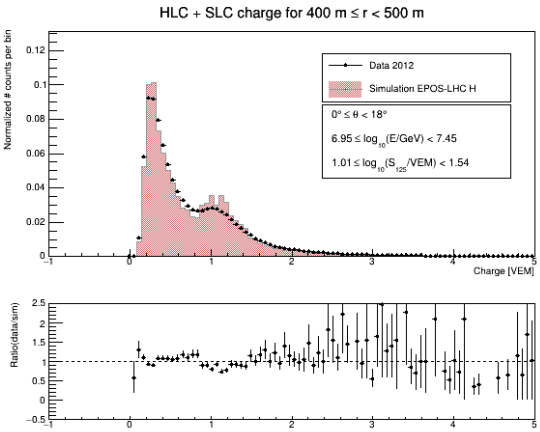
HLC + SLC charge for 400 m ≤ r < 500 m
Data 2012
Simulation EPOS-LHC H
0° ≤ θ < 18°
6.95 ≤ log10(E/GeV) < 7.45
1.01 ≤ log10(S125/VEM) < 1.54
Normalized # counts per bin
Charge [VEM]
Ratio(data/sim)

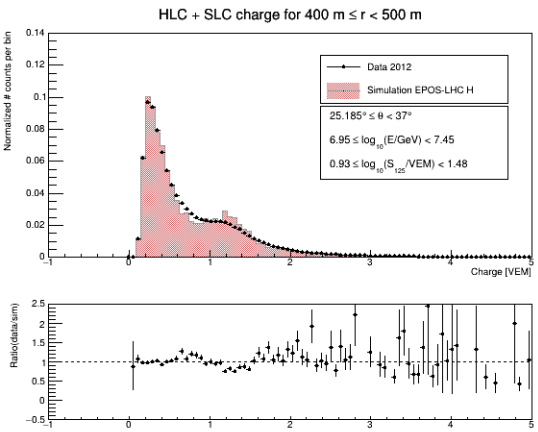
HLC + SLC charge for 400 m ≤ r < 500 m
Data 2012
Simulation EPOS-LHC H
25.185° ≤ θ < 37°
6.95 ≤ log10(E/GeV) < 7.45
0.93 ≤ log10(S125/VEM) < 1.48
Normalized # counts per bin
Charge [VEM]
Ratio(data/sim)

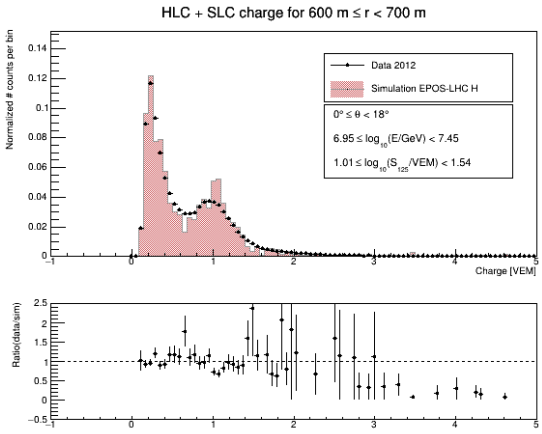
HLC + SLC charge for 600 m ≤ r < 700 m
Normalized # counts per bin
Data 2012
Simulation EPOS-LHC H
0° ≤ θ < 18°
6.95 ≤ log10(E/GeV) < 7.45
1.01 ≤ log10(S125/VEM) < 1.54
Charge [VEM]
Ratio(data/sim)

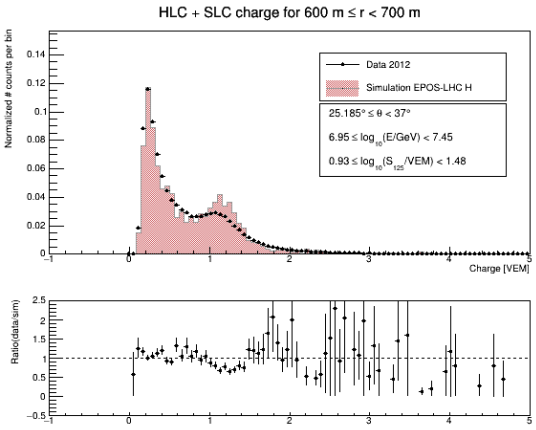
HLC + SLC charge for 600 m ≤ r < 700 m
Normalized # counts per bin
Data 2012
Simulation EPOS-LHC H
25.185° ≤ θ < 37°
6.95 ≤ log10(E/GeV) < 7.45
0.93 ≤ log10(S125/VEM) < 1.48
Charge [VEM]
Ratio(data/sim)

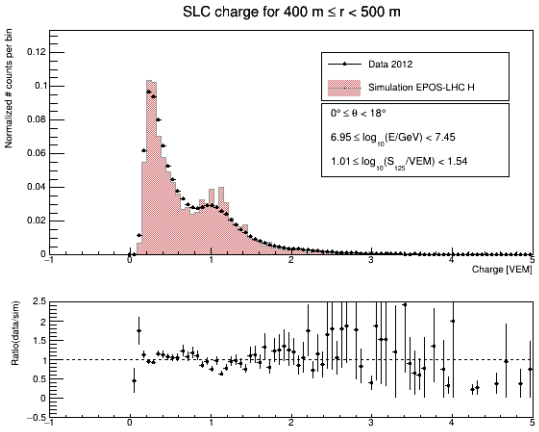
SLC charge for 400 m ≤ r < 500 m
Normalized # counts per bin
Data 2012
Simulation EPOS-LHC H
0° ≤ θ < 18°
6.95 ≤ log10(E/GeV) < 7.45
1.01 ≤ log10(S125/VEM) < 1.54
Charge [VEM]
Ratio(data/sim)

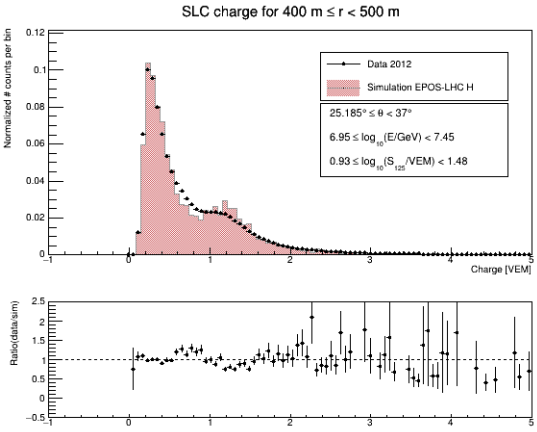
SLC charge for 400 m ≤ r < 500 m
Normalized # counts per bin
Data 2012
Simulation EPOS-LHC H
25.185° ≤ θ < 37°
6.95 ≤ log10(E/GeV) < 7.45
0.93 ≤ log10(S125/VEM) < 1.48
Charge [VEM]
Ratio(data/sim)

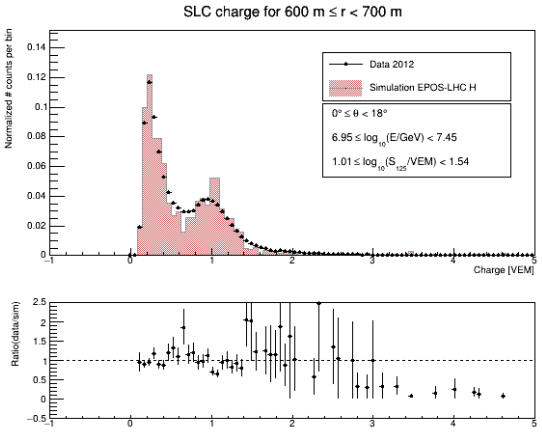
SLC charge for 600 m ≤ r < 700 m
Normalized # counts per bin
Data 2012
Simulation EPOS-LHC H
0° ≤ θ < 18°
6.95 ≤ log10(E/GeV) < 7.45
1.01 ≤ log10(S125/VEM) < 1.54
Charge [VEM]
Ratio(data/sim)

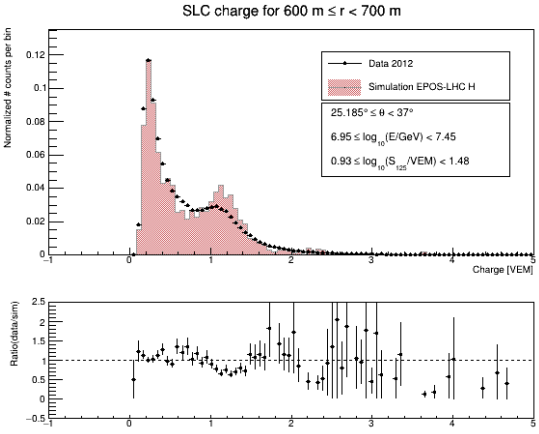
SLC charge for 600 m ≤ r < 700 m
Normalized # counts per bin
Data 2012
Simulation EPOS-LHC H
25.185° ≤ θ < 37°
6.95 ≤ log10(E/GeV) < 7.45
0.93 ≤ log10(S125/VEM) < 1.48
Charge [VEM]
Ratio(data/sim)

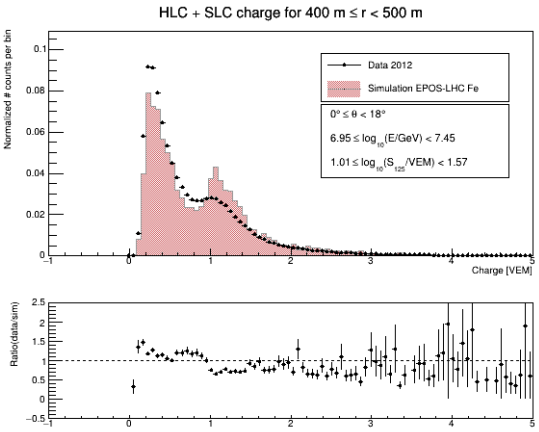
HLC + SLC charge for 400 m ≤ r < 500 m
Data 2012
Simulation EPOS-LHC Fe
0° ≤ θ < 18°
6.95 ≤ log10(E/GeV) < 7.45
1.01 ≤ log10(S125/VEM) < 1.57
Normalized # counts per bin
Charge [VEM]
Ratio(data/sim)

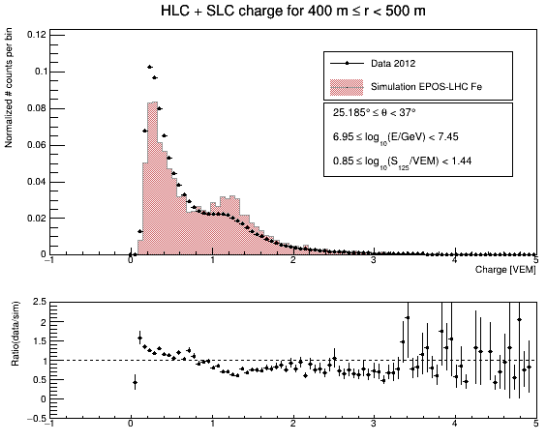
HLC + SLC charge for 400 m ≤ r < 500 m
Data 2012
Simulation EPOS-LHC Fe
25.185° ≤ θ < 37°
6.95 ≤ log10(E/GeV) < 7.45
0.85 ≤ log10(S125/VEM) < 1.44
Normalized # counts per bin
Charge [VEM]
Ratio(data/sim)

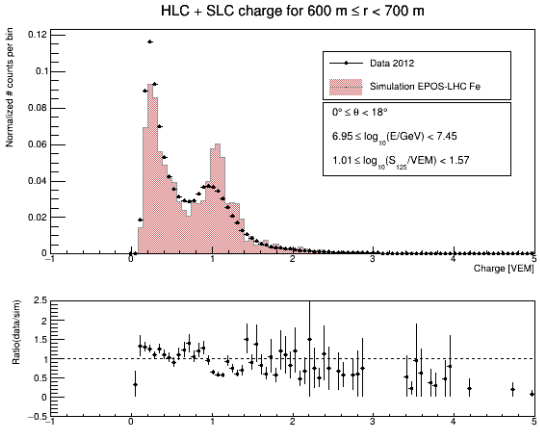
HLC + SLC charge for 600 m ≤ r < 700 m
Data 2012
Simulation EPOS-LHC Fe
0° ≤ θ < 18°
6.95 ≤ log10(E/GeV) < 7.45
1.01 ≤ log10(S125/VEM) < 1.57
Normalized # counts per bin
Charge [VEM]
Ratio(data/sim)

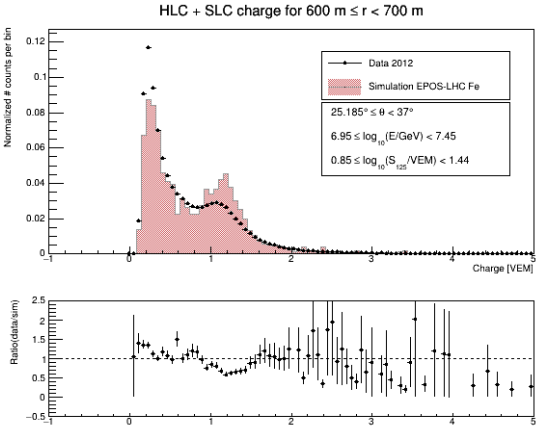
HLC + SLC charge for 600 m ≤ r < 700 m
Data 2012
Simulation EPOS-LHC Fe
25.185° ≤ θ < 37°
6.95 ≤ log10(E/GeV) < 7.45
0.85 ≤ log10(S125/VEM) < 1.44
Normalized # counts per bin
Charge [VEM]
Ratio(data/sim)

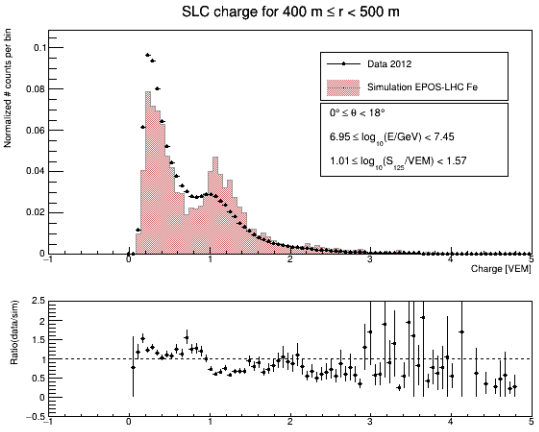
SLC charge for 400 m ≤ r < 500 m
Data 2012
Simulation EPOS-LHC Fe
0° ≤ θ < 18°
6.95 ≤ log10(E/GeV) < 7.45
1.01 ≤ log10(S125/VEM) < 1.57
Normalized # counts per bin
Charge [VEM]
Ratio(data/sim)

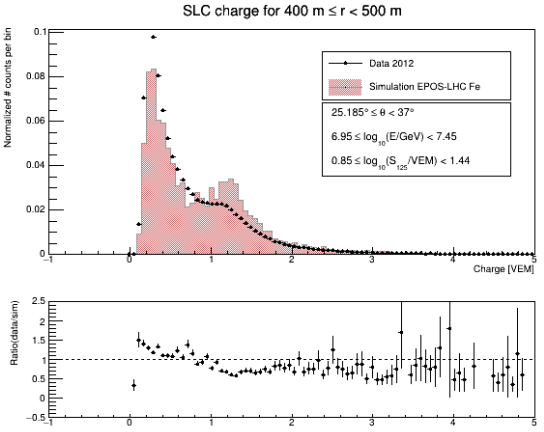
SLC charge for 400 m ≤ r < 500 m
Data 2012
Simulation EPOS-LHC Fe
25.185° ≤ θ < 37°
6.95 ≤ log10(E/GeV) < 7.45
0.85 ≤ log10(S125/VEM) < 1.44
Normalized # counts per bin
Charge [VEM]
Ratio(data/sim)

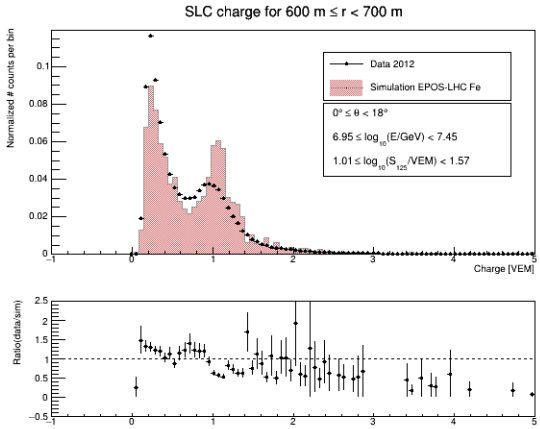
SLC charge for 600 m ≤ r < 700 m
Data 2012
Simulation EPOS-LHC Fe
0° ≤ θ < 18°
6.95 ≤ log10(E/GeV) < 7.45
1.01 ≤ log10(S125/VEM) < 1.57
Normalized # counts per bin
Charge [VEM]
Ratio(data/sim)

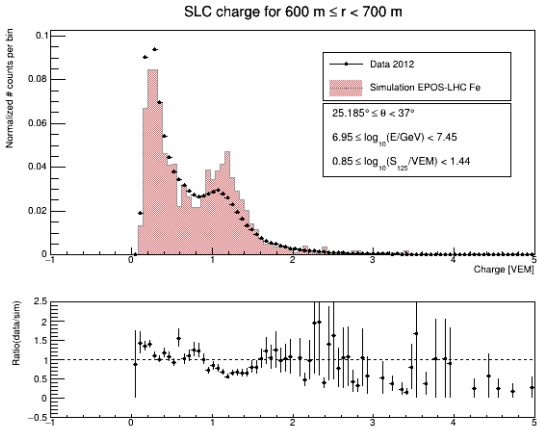
SLC charge for 600 m ≤ r < 700 m
Data 2012
Simulation EPOS-LHC Fe
25.185° ≤ θ < 37°
6.95 ≤ log10(E/GeV) < 7.45
0.85 ≤ log10(S125/VEM) < 1.44
Normalized # counts per bin
Charge [VEM]
Ratio(data/sim)

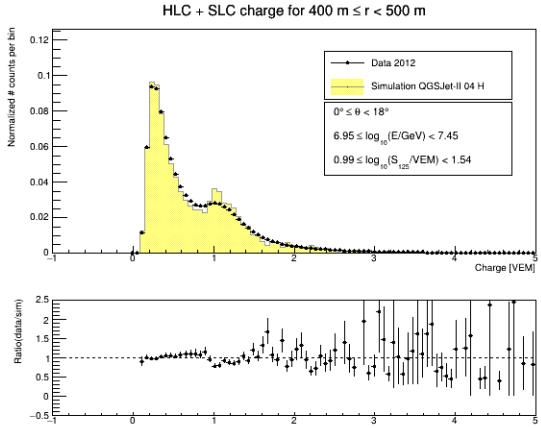
HLC + SLC charge for 400 m ≤ r < 500 m
Data 2012
Simulation QGSJet-II 04 H
0° ≤ θ < 18°
6.95 ≤ log10(E/GeV) < 7.45
0.99 ≤ log10(S125/VEM) < 1.54
Normalized # counts per bin
Charge [VEM]
Ratio(data/sim)

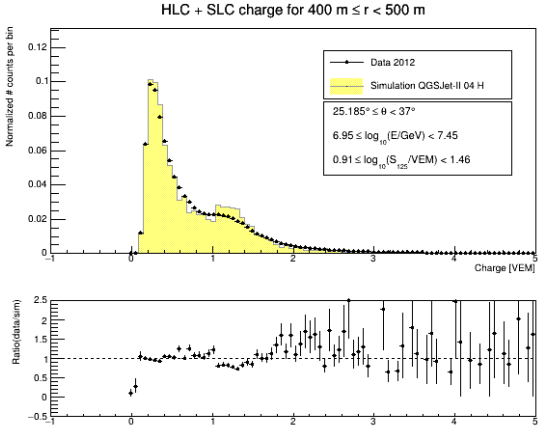
HLC + SLC charge for 400 m ≤ r < 500 m
Data 2012
Simulation QGSJet-II 04 H
25.185° ≤ θ < 37°
6.95 ≤ log10(E/GeV) < 7.45
0.91 ≤ log10(S125/VEM) < 1.46
Normalized # counts per bin
Charge [VEM]
Ratio(data/sim)

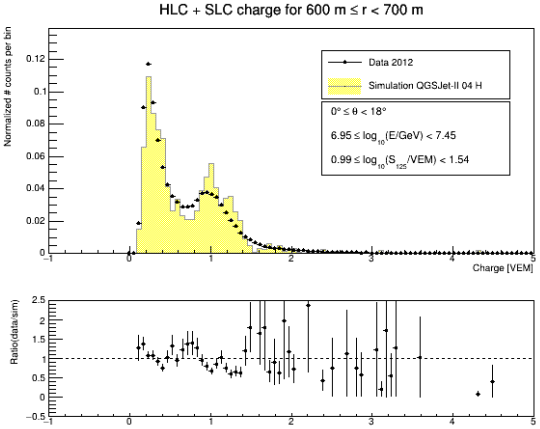
HLC + SLC charge for 600 m ≤ r < 700 m
Data 2012
Simulation QGSJet-II 04 H
0° ≤ θ < 18°
6.95 ≤ log10(E/GeV) < 7.45
0.99 ≤ log10(S125/VEM) < 1.54
Normalized # counts per bin
Charge [VEM]
Ratio(data/sim)

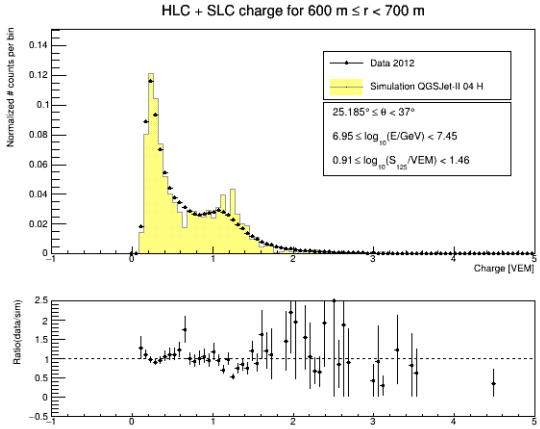
HLC + SLC charge for 600 m ≤ r < 700 m
Data 2012
Simulation QGSJet-II 04 H
25.185° ≤ θ < 37°
6.95 ≤ log10(E/GeV) < 7.45
0.91 ≤ log10(S125/VEM) < 1.46
Normalized # counts per bin
Charge [VEM]
Ratio(data/sim)

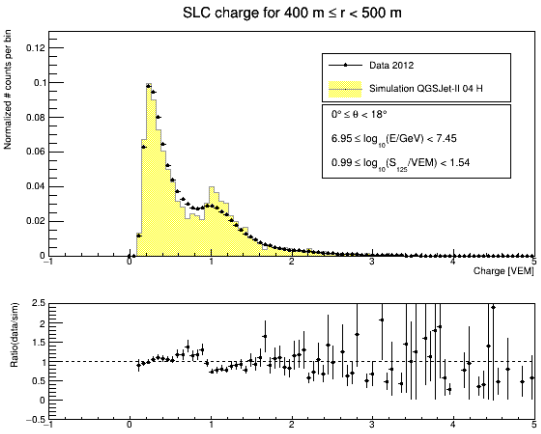
SLC charge for 400 m ≤ r < 500 m
Data 2012
Simulation QGSJet-II 04 H
0° ≤ θ < 18°
6.95 ≤ log10(E/GeV) < 7.45
0.99 ≤ log10(S125/VEM) < 1.54
Normalized # counts per bin
Charge [VEM]
Ratio(data/sim)

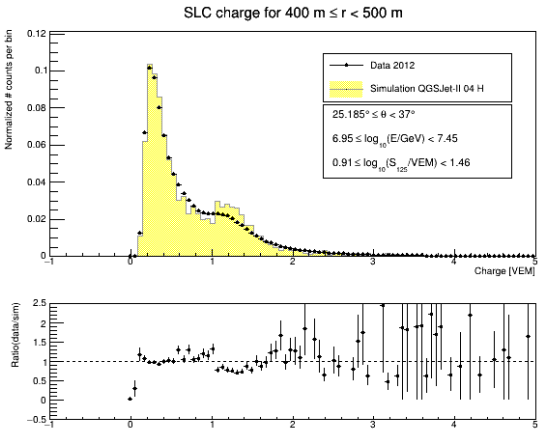
SLC charge for 400 m ≤ r < 500 m
Data 2012
Simulation QGSJet-II 04 H
25.185° ≤ θ < 37°
6.95 ≤ log10(E/GeV) < 7.45
0.91 ≤ log10(S125/VEM) < 1.46
Normalized # counts per bin
Charge [VEM]
Ratio(data/sim)

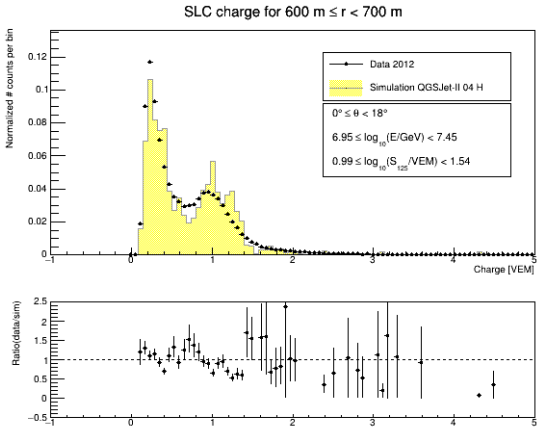
SLC charge for 600 m ≤ r < 700 m
Data 2012
Simulation QGSJet-II 04 H
0° ≤ θ < 18°
6.95 ≤ log10(E/GeV) < 7.45
0.99 ≤ log10(S125/VEM) < 1.54
Normalized # counts per bin
Charge [VEM]
Ratio(data/sim)

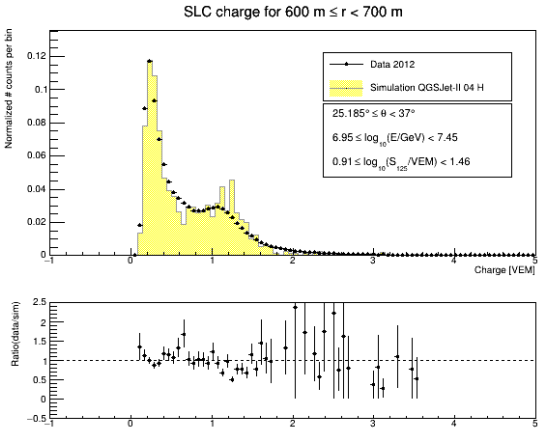
SLC charge for 600 m ≤ r < 700 m
Data 2012
Simulation QGSJet-II 04 H
25.185° ≤ θ < 37°
6.95 ≤ log10(E/GeV) < 7.45
0.91 ≤ log10(S125/VEM) < 1.46
Normalized # counts per bin
Charge [VEM]
Ratio(data/sim)

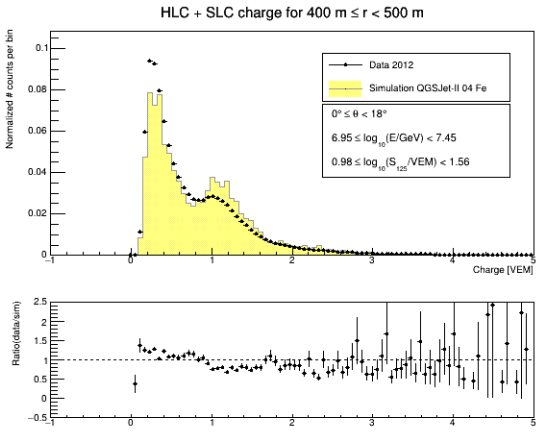
HLC + SLC charge for 400 m ≤ r < 500 m
Data 2012
Simulation QGSJet-II 04 Fe
0° ≤ θ < 18°
6.95 ≤ log10(E/GeV) < 7.45
0.98 ≤ log10(S125/VEM) < 1.56
Normalized # counts per bin
Charge [VEM]
Ratio(data/sim)

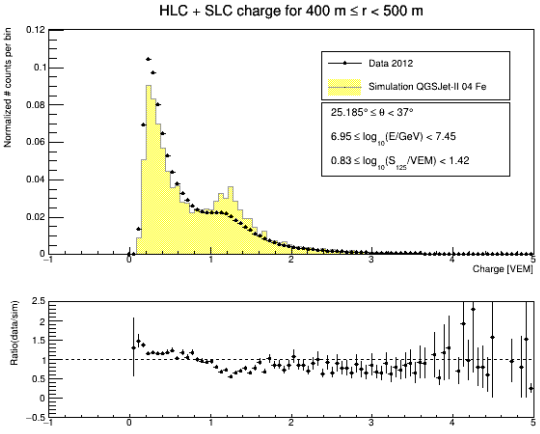
HLC + SLC charge for 400 m ≤ r < 500 m
Data 2012
Simulation QGSJet-II 04 Fe
25.185° ≤ θ < 37°
6.95 ≤ log10(E/GeV) < 7.45
0.83 ≤ log10(S125/VEM) < 1.42
Normalized # counts per bin
Charge [VEM]
Ratio(data/sim)

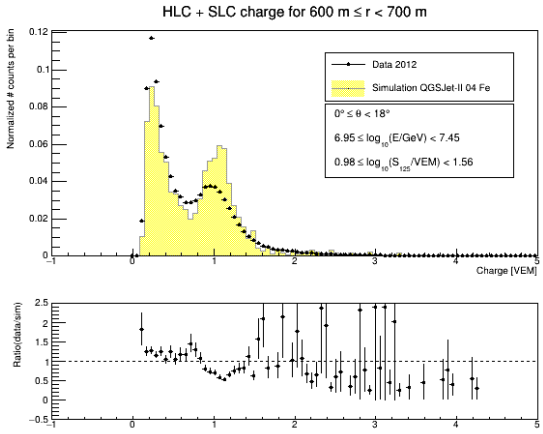
HLC + SLC charge for 600 m ≤ r < 700 m
Normalized # counts per bin
Data 2012
Simulation QGSJet-II 04 Fe
0° ≤ θ < 18°
6.95 ≤ log10(E/GeV) < 7.45
0.98 ≤ log10(S125/VEM) < 1.56
Charge [VEM]
Ratio(data/sim)

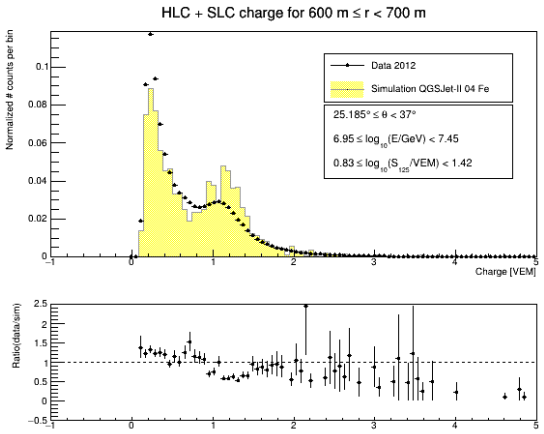
HLC + SLC charge for 600 m ≤ r < 700 m
Normalized # counts per bin
Data 2012
Simulation QGSJet-II 04 Fe
25.185° ≤ θ < 37°
6.95 ≤ log10(E/GeV) < 7.45
0.83 ≤ log10(S125/VEM) < 1.42
Charge [VEM]
Ratio(data/sim)

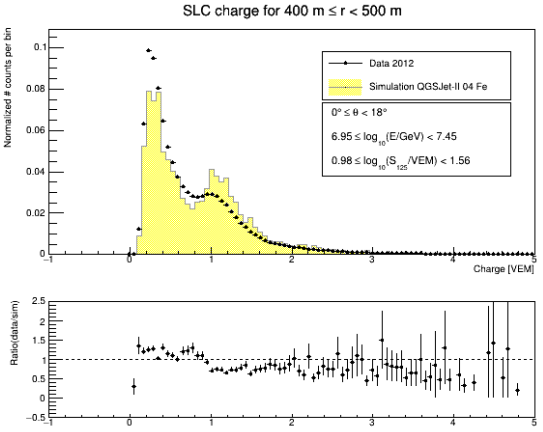
SLC charge for 400 m ≤ r < 500 m
Normalized # counts per bin
Data 2012
Simulation QGSJet-II 04 Fe
0° ≤ θ < 18°
6.95 ≤ log10(E/GeV) < 7.45
0.98 ≤ log10(S125/VEM) < 1.56
Charge [VEM]
Ratio(data/sim)

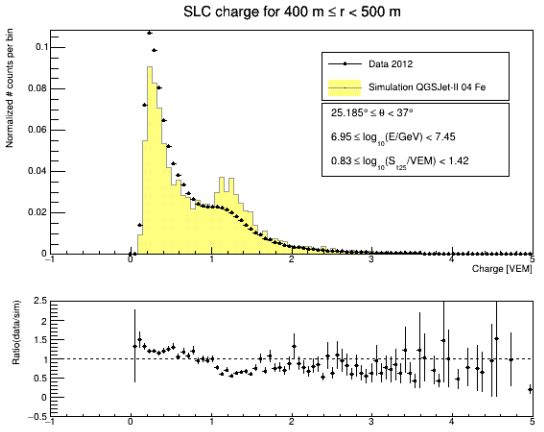
SLC charge for 400 m ≤ r < 500 m
Normalized # counts per bin
Data 2012
Simulation QGSJet-II 04 Fe
25.185° ≤ θ < 37°
6.95 ≤ log10(E/GeV) < 7.45
0.83 ≤ log10(S125/VEM) < 1.42
Charge [VEM]
Ratio(data/sim)

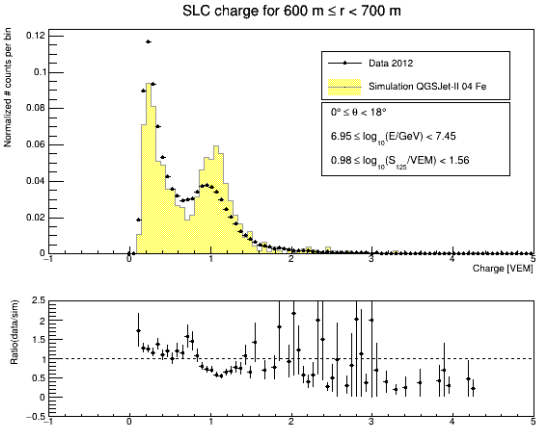
SLC charge for 600 m ≤ r < 700 m
Normalized # counts per bin
Data 2012
Simulation QGSJet-II 04 Fe
0° ≤ θ < 18°
6.95 ≤ log10(E/GeV) < 7.45
0.98 ≤ log10(S125/VEM) < 1.56
Charge [VEM]
Ratio(data/sim)

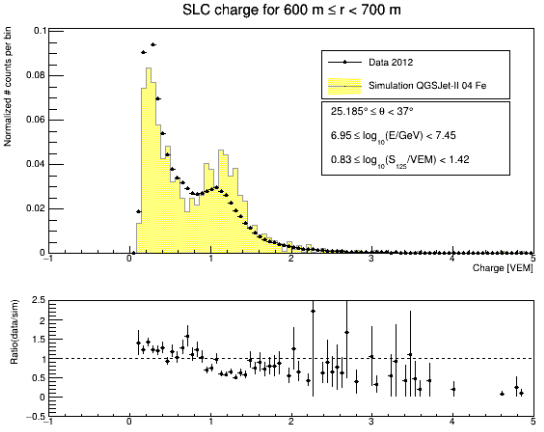
SLC charge for 600 m ≤ r < 700 m
Normalized # counts per bin
Data 2012
Simulation QGSJet-II 04 Fe
25.185° ≤ θ < 37°
6.95 ≤ log10(E/GeV) < 7.45
0.83 ≤ log10(S125/VEM) < 1.42
Charge [VEM]
Ratio(data/sim)

A.2.2. Ratio plots with H and Fe primary

In this Section, the distributions and ratio plots contain experimental data as well as simulated data for proton and iron primaries. First, the plots with normalization according to Equation (26) in Section 6.2.1 are shown.

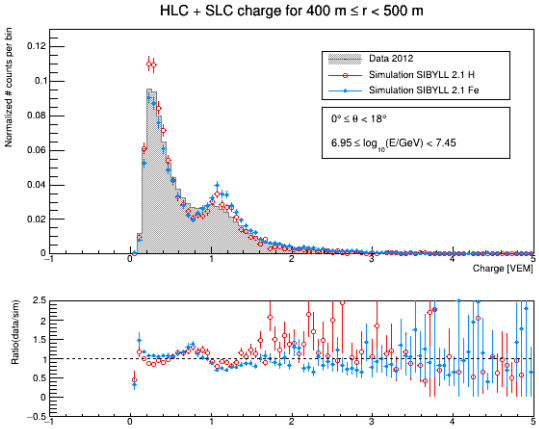

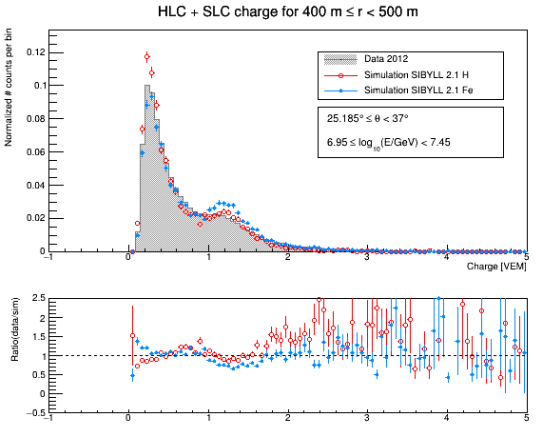

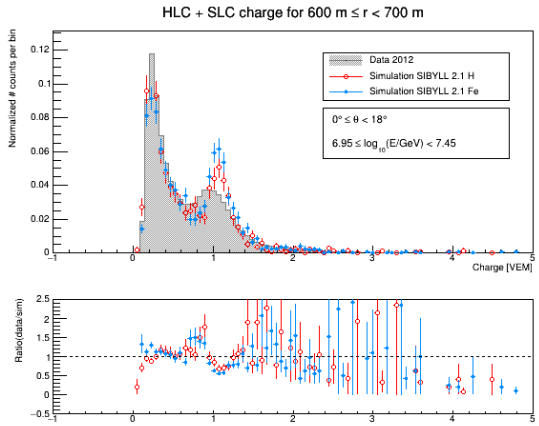

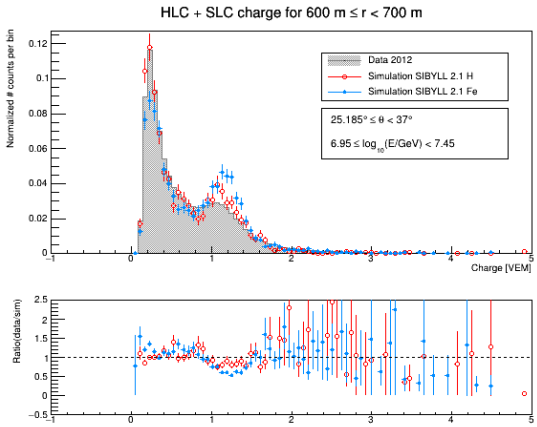

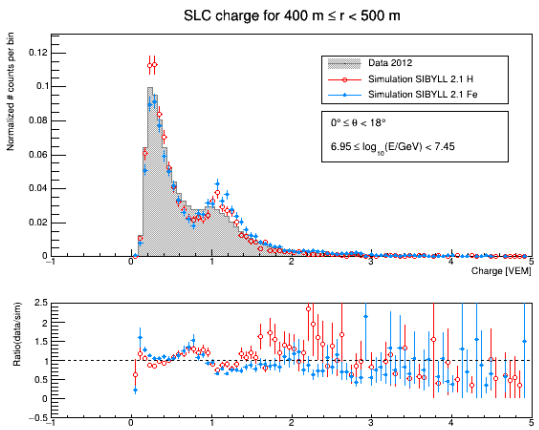

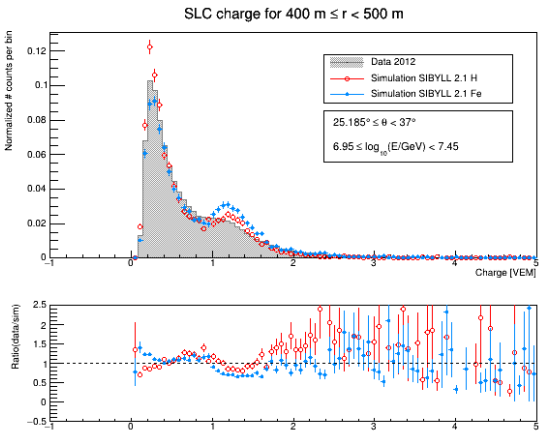

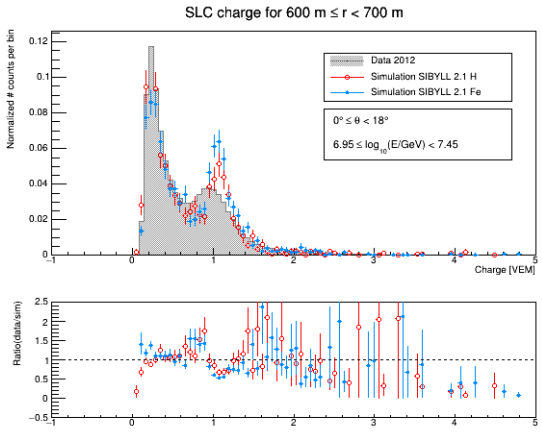
SLC charge for 600 m ≤ r < 700 m
Data 2012
Simulation SIBYLL 2.1 H
Simulation SIBYLL 2.1 Fe
0° ≤ θ < 18°
6.95 ≤ log10(E/GeV) < 7.45
Normalized # counts per bin
Charge [VEM]
Ratio(data/sim)

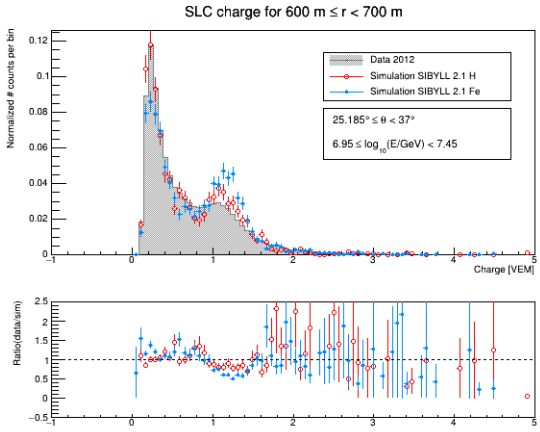
SLC charge for 600 m ≤ r < 700 m
Data 2012
Simulation SIBYLL 2.1 H
Simulation SIBYLL 2.1 Fe
25.185° ≤ θ < 37°
6.95 ≤ log10(E/GeV) < 7.45
Normalized # counts per bin
Charge [VEM]
Ratio(data/sim)

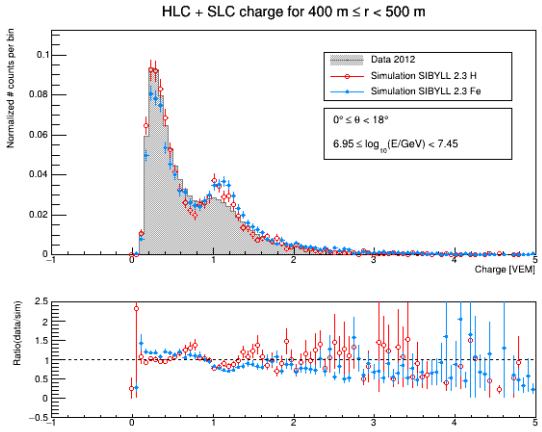
HLC + SLC charge for 400 m ≤ r < 500 m
Data 2012
Simulation SIBYLL 2.3 H
Simulation SIBYLL 2.3 Fe
0° ≤ θ < 18°
6.95 ≤ log10(E/GeV) < 7.45
Normalized # counts per bin
Charge [VEM]
Ratio(data/sim)

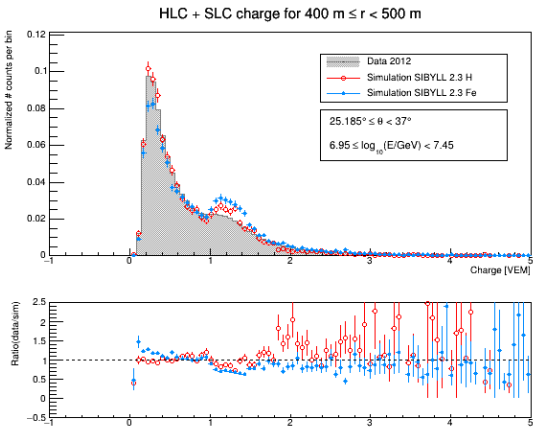
HLC + SLC charge for 400 m ≤ r < 500 m
Data 2012
Simulation SIBYLL 2.3 H
Simulation SIBYLL 2.3 Fe
25.185° ≤ θ < 37°
6.95 ≤ log10(E/GeV) < 7.45
Normalized # counts per bin
Charge [VEM]
Ratio(data/sim)

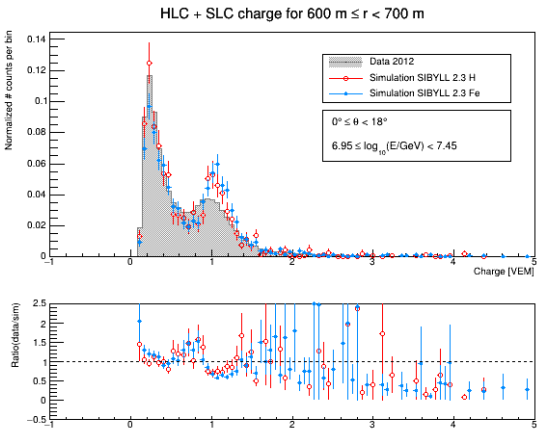
HLC + SLC charge for 600 m ≤ r < 700 m
Data 2012
Simulation SIBYLL 2.3 H
Simulation SIBYLL 2.3 Fe
0° ≤ θ < 18°
6.95 ≤ log10(E/GeV) < 7.45
Normalized # counts per bin
Charge [VEM]
Ratio(data/sim)

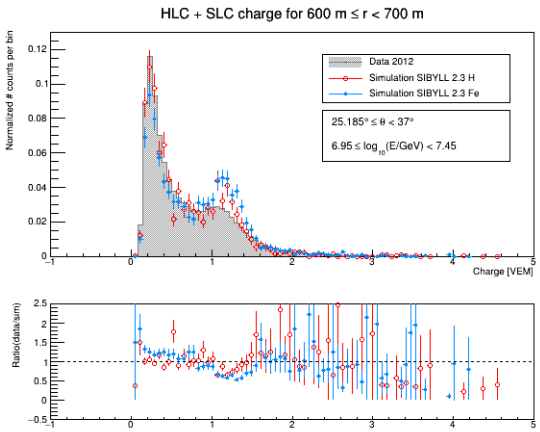
HLC + SLC charge for 600 m ≤ r < 700 m
Data 2012
Simulation SIBYLL 2.3 H
Simulation SIBYLL 2.3 Fe
25.185° ≤ θ < 37°
6.95 ≤ log10(E/GeV) < 7.45
Normalized # counts per bin
Charge [VEM]
Ratio(data/sim)

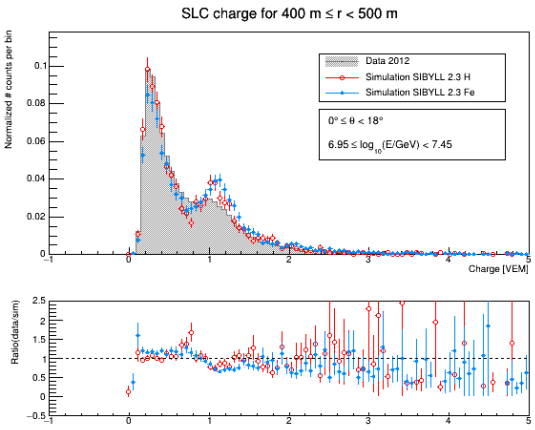
SLC charge for 400 m ≤ r < 500 m
Data 2012
Simulation SIBYLL 2.3 H
Simulation SIBYLL 2.3 Fe
0° ≤ θ < 18°
6.95 ≤ log10(E/GeV) < 7.45
Normalized # counts per bin
Charge [VEM]
Ratio(data/sim)

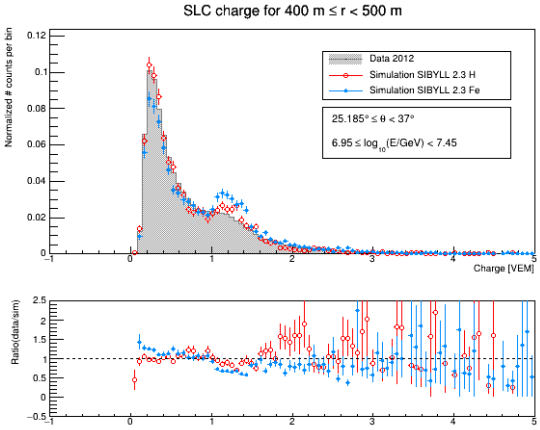
SLC charge for 400 m ≤ r < 500 m
Data 2012
Simulation SIBYLL 2.3 H
Simulation SIBYLL 2.3 Fe
25.185° ≤ θ < 37°
6.95 ≤ log10(E/GeV) < 7.45
Normalized # counts per bin
Charge [VEM]
Ratio(data/sim)

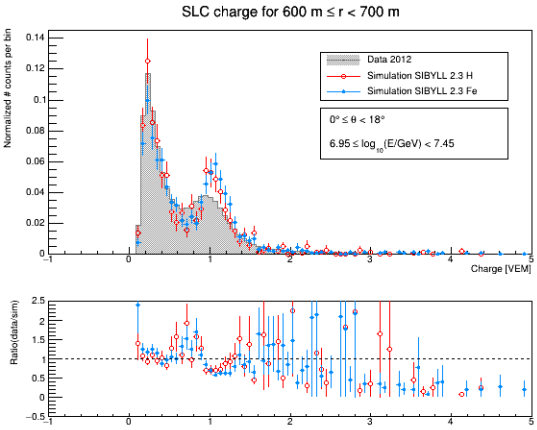
SLC charge for 600 m ≤ r < 700 m
Data 2012
Simulation SIBYLL 2.3 H
Simulation SIBYLL 2.3 Fe
0° ≤ θ < 18°
6.95 ≤ log10(E/GeV) < 7.45
Normalized # counts per bin
Charge [VEM]
Ratio(data/sim)

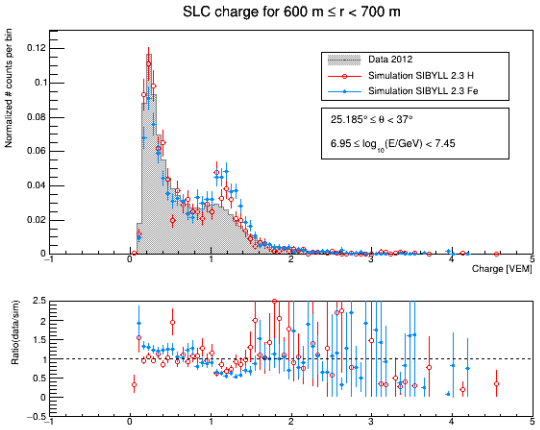
SLC charge for 600 m ≤ r < 700 m
Data 2012
Simulation SIBYLL 2.3 H
Simulation SIBYLL 2.3 Fe
25.185° ≤ θ < 37°
6.95 ≤ log10(E/GeV) < 7.45
Normalized # counts per bin
Charge [VEM]
Ratio(data/sim)

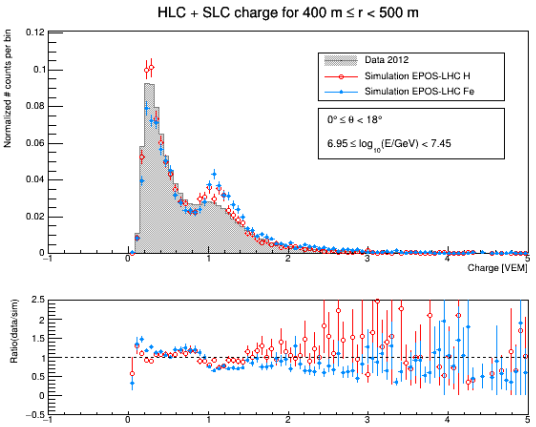
HLC + SLC charge for 400 m ≤ r < 500 m
Data 2012
Simulation EPOS-LHC H
Simulation EPOS-LHC Fe
0° ≤ θ < 18°
6.95 ≤ log10(E/GeV) < 7.45
Normalized # counts per bin
Charge [VEM]
Ratio(data/sim)

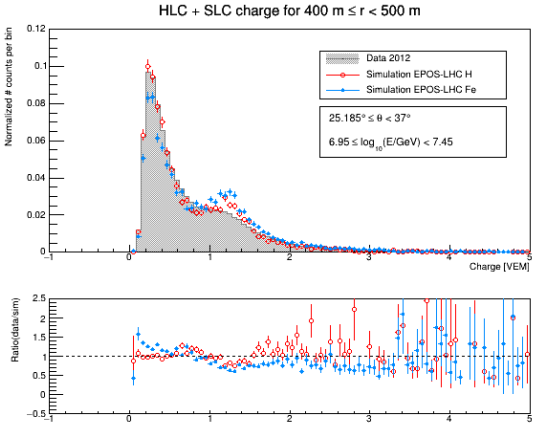
HLC + SLC charge for 400 m ≤ r < 500 m
Data 2012
Simulation EPOS-LHC H
Simulation EPOS-LHC Fe
25.185° ≤ θ < 37°
6.95 ≤ log10(E/GeV) < 7.45
Normalized # counts per bin
Charge [VEM]
Ratio(data/sim)

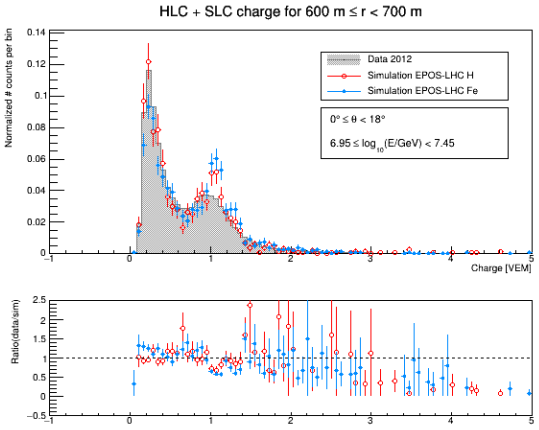
HLC + SLC charge for 600 m ≤ r < 700 m
Normalized # counts per bin
Data 2012
Simulation EPOS-LHC H
Simulation EPOS-LHC Fe
0° ≤ θ < 18°
6.95 ≤ log10(E/GeV) < 7.45
Charge [VEM]
Ratio(data/sim)

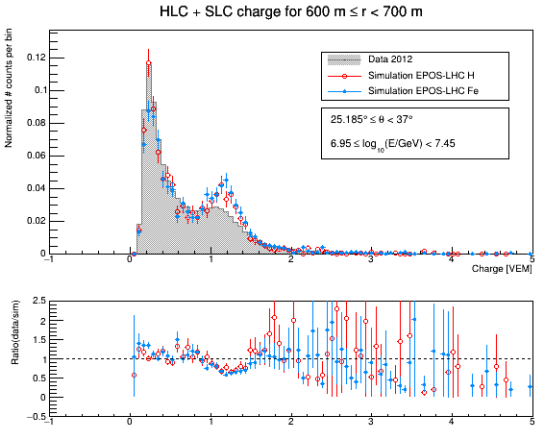
HLC + SLC charge for 600 m ≤ r < 700 m
Normalized # counts per bin
Data 2012
Simulation EPOS-LHC H
Simulation EPOS-LHC Fe
25.185° ≤ θ < 37°
6.95 ≤ log10(E/GeV) < 7.45
Charge [VEM]
Ratio(data/sim)

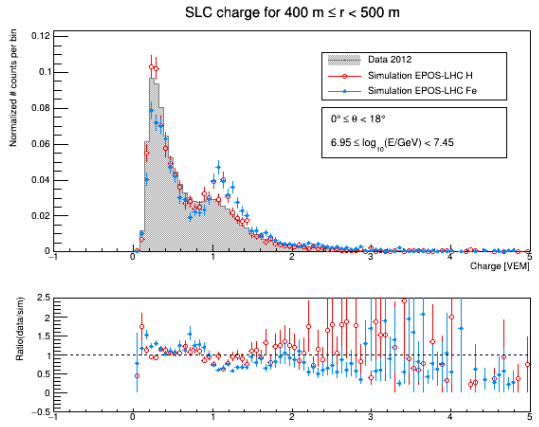
SLC charge for 400 m ≤ r < 500 m
Normalized # counts per bin
Data 2012
Simulation EPOS-LHC H
Simulation EPOS-LHC Fe
0° ≤ θ < 18°
6.95 ≤ log10(E/GeV) < 7.45
Charge [VEM]
Ratio(data/sim)

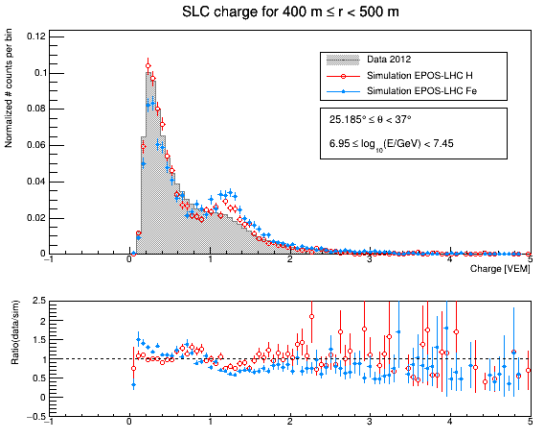
SLC charge for 400 m ≤ r < 500 m
Normalized # counts per bin
Data 2012
Simulation EPOS-LHC H
Simulation EPOS-LHC Fe
25.185° ≤ θ < 37°
6.95 ≤ log10(E/GeV) < 7.45
Charge [VEM]
Ratio(data/sim)

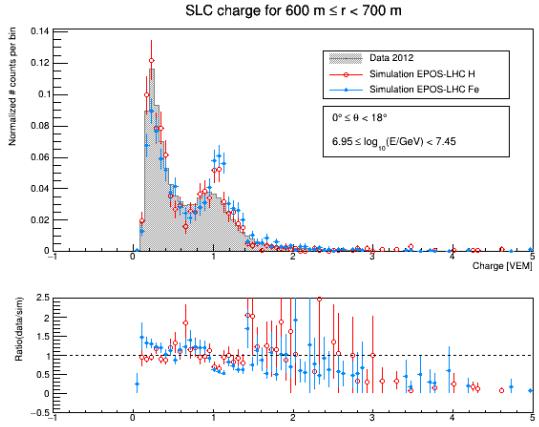
SLC charge for 600 m ≤ r < 700 m
Normalized # counts per bin
Data 2012
Simulation EPOS-LHC H
Simulation EPOS-LHC Fe
0° ≤ θ < 18°
6.95 ≤ log10(E/GeV) < 7.45
Charge [VEM]
Ratio(data/sim)

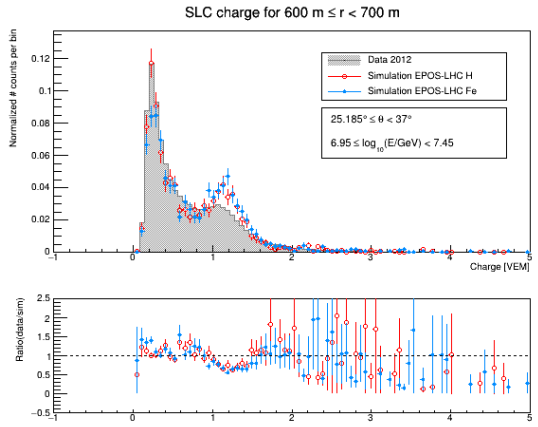
SLC charge for 600 m ≤ r < 700 m
Normalized # counts per bin
Data 2012
Simulation EPOS-LHC H
Simulation EPOS-LHC Fe
25.185° ≤ θ < 37°
6.95 ≤ log10(E/GeV) < 7.45
Charge [VEM]
Ratio(data/sim)

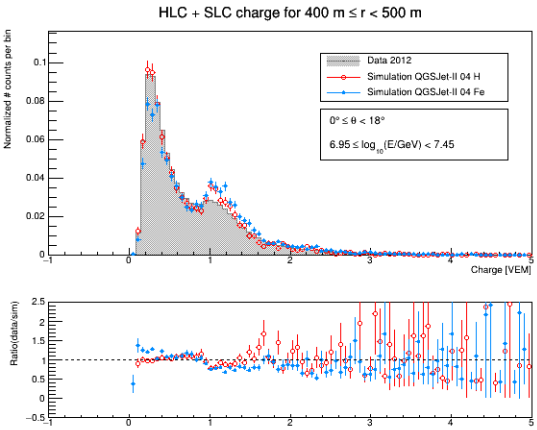
HLC + SLC charge for 400 m ≤ r < 500 m
Data 2012
Simulation QGSJet-II 04 H
Simulation QGSJet-II 04 Fe
0° ≤ θ < 18°
6.95 ≤ log10(E/GeV) < 7.45
Normalized # counts per bin
Charge [VEM]
Ratio(data/sim)

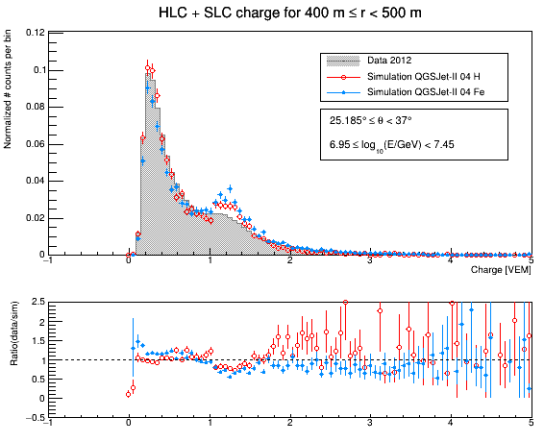
HLC + SLC charge for 400 m ≤ r < 500 m
Data 2012
Simulation QGSJet-II 04 H
Simulation QGSJet-II 04 Fe
25.185° ≤ θ < 37°
6.95 ≤ log10(E/GeV) < 7.45
Normalized # counts per bin
Charge [VEM]
Ratio(data/sim)

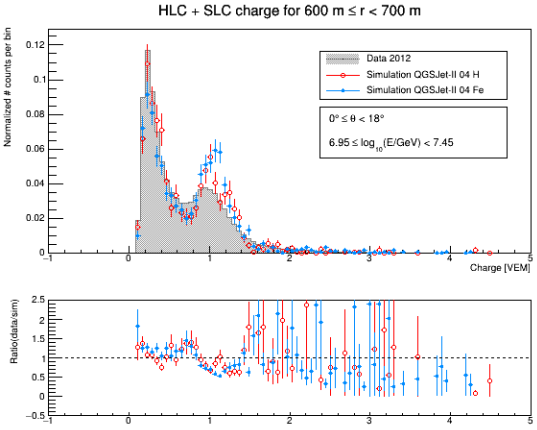
HLC + SLC charge for 600 m ≤ r < 700 m
Data 2012
Simulation QGSJet-II 04 H
Simulation QGSJet-II 04 Fe
0° ≤ θ < 18°
6.95 ≤ log10(E/GeV) < 7.45
Normalized # counts per bin
Charge [VEM]
Ratio(data/sim)

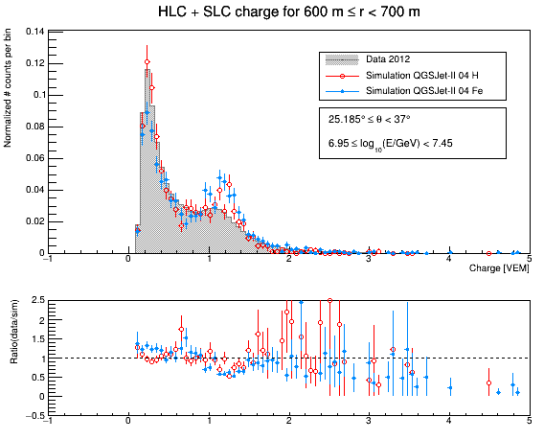
HLC + SLC charge for 600 m ≤ r < 700 m
Data 2012
Simulation QGSJet-II 04 H
Simulation QGSJet-II 04 Fe
25.185° ≤ θ < 37°
6.95 ≤ log10(E/GeV) < 7.45
Normalized # counts per bin
Charge [VEM]
Ratio(data/sim)

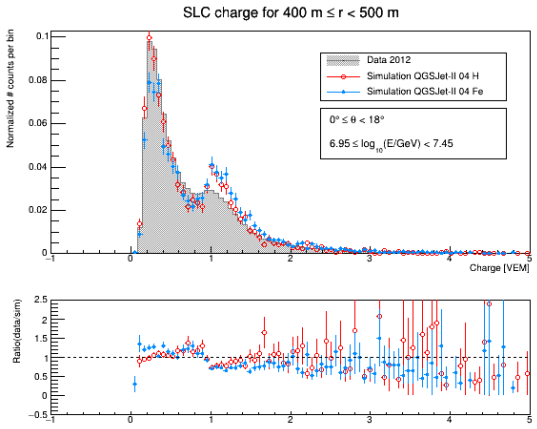
SLC charge for 400 m ≤ r < 500 m
Data 2012
Simulation QGSJet-II 04 H
Simulation QGSJet-II 04 Fe
0° ≤ θ < 18°
6.95 ≤ log10(E/GeV) < 7.45
Normalized # counts per bin
Charge [VEM]
Ratio(data/sim)

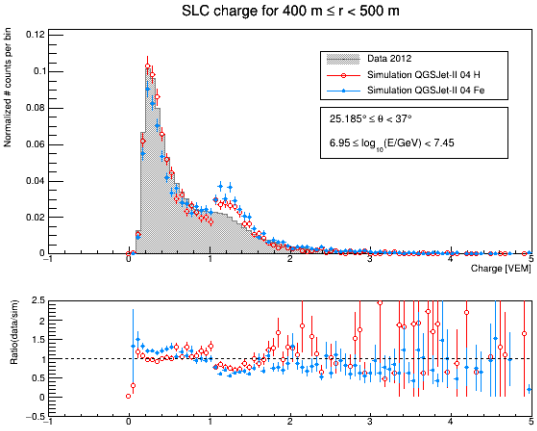
SLC charge for 400 m ≤ r < 500 m
Data 2012
Simulation QGSJet-II 04 H
Simulation QGSJet-II 04 Fe
25.185° ≤ θ < 37°
6.95 ≤ log10(E/GeV) < 7.45
Normalized # counts per bin
Charge [VEM]
Ratio(data/sim)

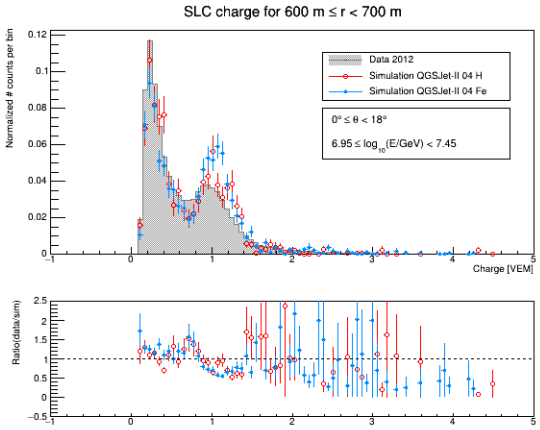
SLC charge for 600 m ≤ r < 700 m
Normalized # counts per bin
Data 2012
Simulation QGSJet-II 04 H
Simulation QGSJet-II 04 Fe
0° ≤ θ < 18°
6.95 ≤ log10(E/GeV) < 7.45
Charge [VEM]
Ratio(data/sim)

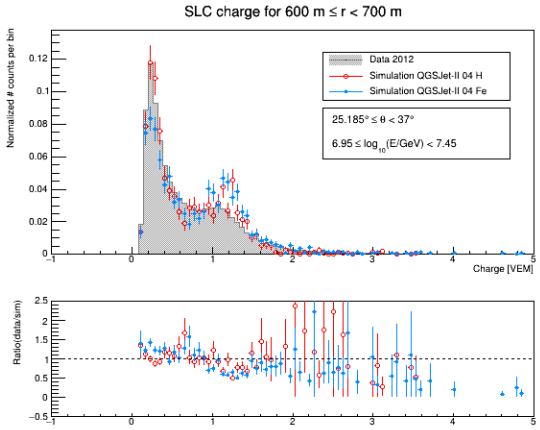
SLC charge for 600 m ≤ r < 700 m
Normalized # counts per bin
Data 2012
Simulation QGSJet-II 04 H
Simulation QGSJet-II 04 Fe
25.185° ≤ θ < 37°
6.95 ≤ log10(E/GeV) < 7.45
Charge [VEM]
Ratio(data/sim)

Now, the plots with normalization according to Equation (27) in Section 6.2.1 are shown.

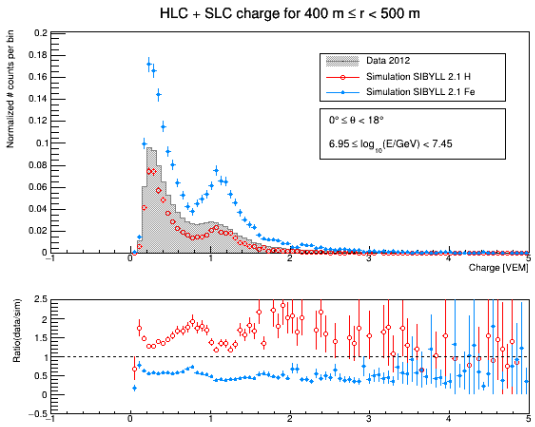

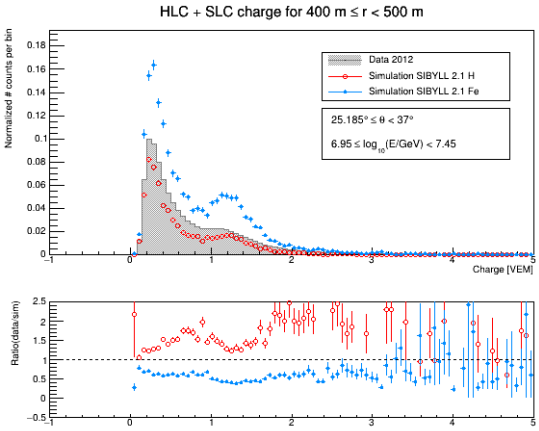

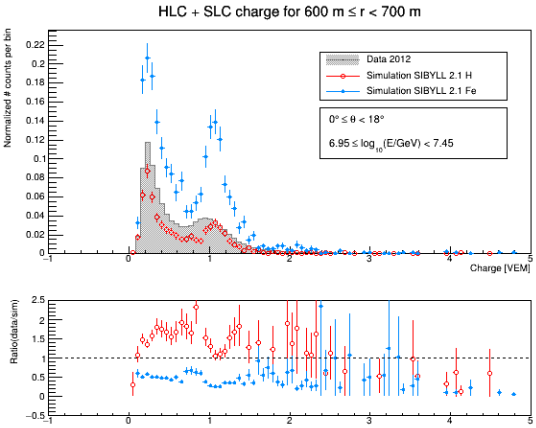

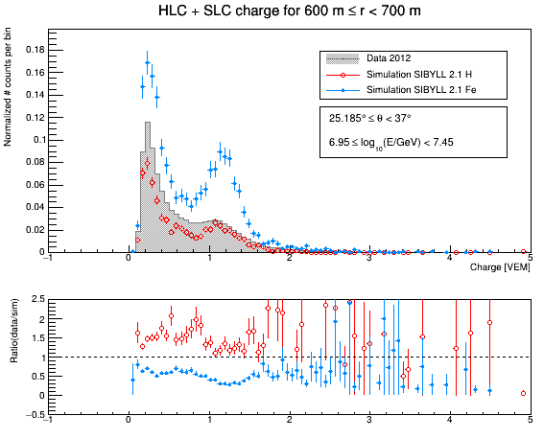

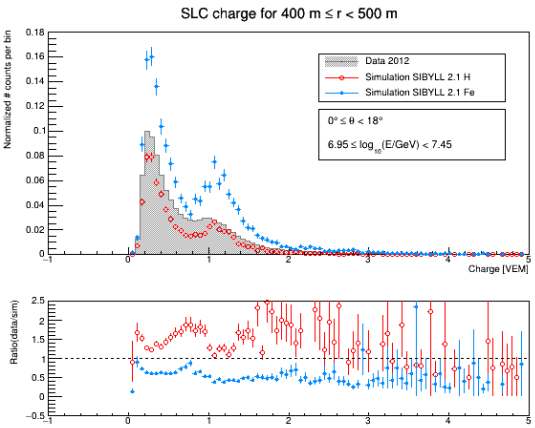

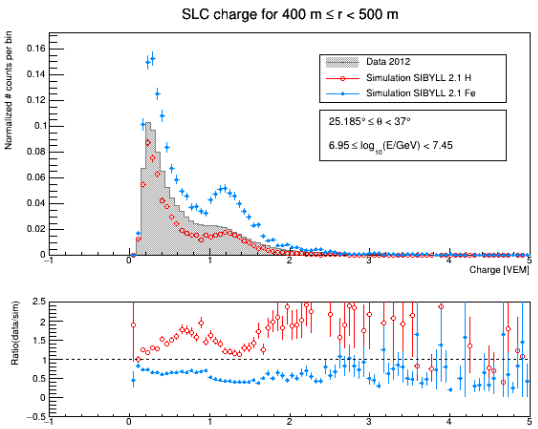

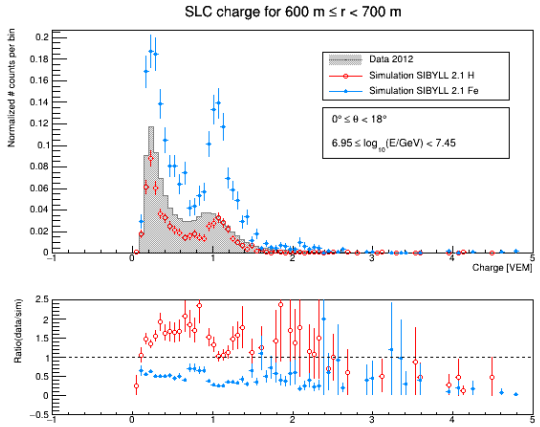
SLC charge for 600 m ≤ r < 700 m
Data 2012
Simulation SIBYLL 2.1 H
Simulation SIBYLL 2.1 Fe
0° ≤ θ < 18°
6.95 ≤ log10(E/GeV) < 7.45
Normalized # counts per bin
Charge [VEM]
Ratio(data/sim)

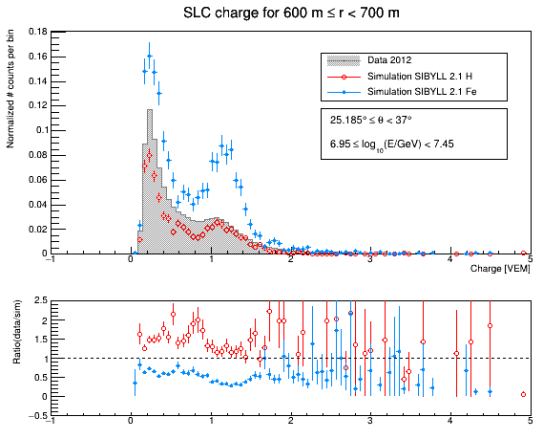
SLC charge for 600 m ≤ r < 700 m
Data 2012
Simulation SIBYLL 2.1 H
Simulation SIBYLL 2.1 Fe
25.185° ≤ θ < 37°
6.95 ≤ log10(E/GeV) < 7.45
Normalized # counts per bin
Charge [VEM]
Ratio(data/sim)

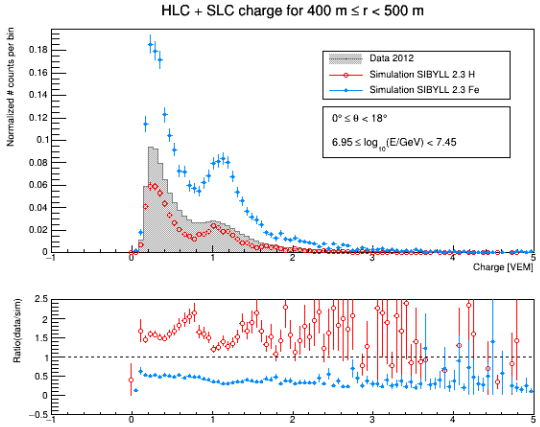
HLC + SLC charge for 400 m ≤ r < 500 m
Data 2012
Simulation SIBYLL 2.3 H
Simulation SIBYLL 2.3 Fe
0° ≤ θ < 18°
6.95 ≤ log10(E/GeV) < 7.45
Normalized # counts per bin
Charge [VEM]
Ratio(data/sim)

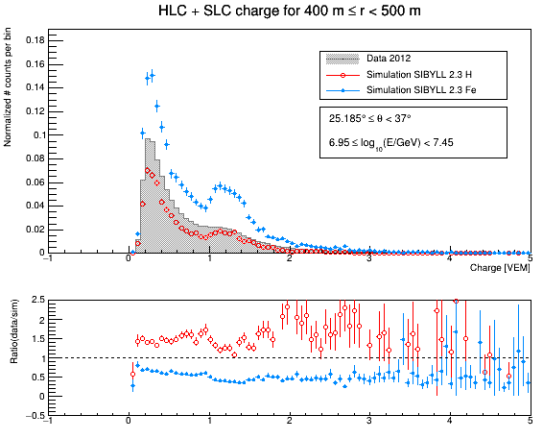
HLC + SLC charge for 400 m ≤ r < 500 m
Data 2012
Simulation SIBYLL 2.3 H
Simulation SIBYLL 2.3 Fe
25.185° ≤ θ < 37°
6.95 ≤ log10(E/GeV) < 7.45
Normalized # counts per bin
Charge [VEM]
Ratio(data/sim)

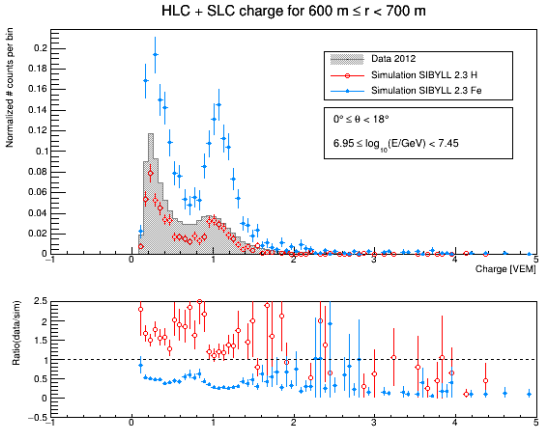
HLC + SLC charge for 600 m ≤ r < 700 m
Data 2012
Simulation SIBYLL 2.3 H
Simulation SIBYLL 2.3 Fe
0° ≤ θ < 18°
6.95 ≤ log10(E/GeV) < 7.45
Normalized # counts per bin
Charge [VEM]
Ratio(data/sim)

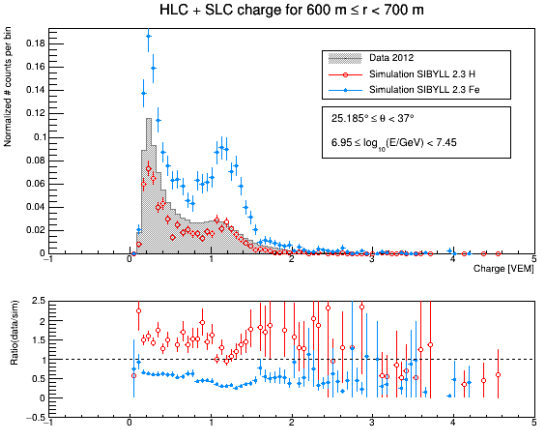
HLC + SLC charge for 600 m ≤ r < 700 m
Data 2012
Simulation SIBYLL 2.3 H
Simulation SIBYLL 2.3 Fe
25.185° ≤ θ < 37°
6.95 ≤ log10(E/GeV) < 7.45
Normalized # counts per bin
Charge [VEM]
Ratio(data/sim)

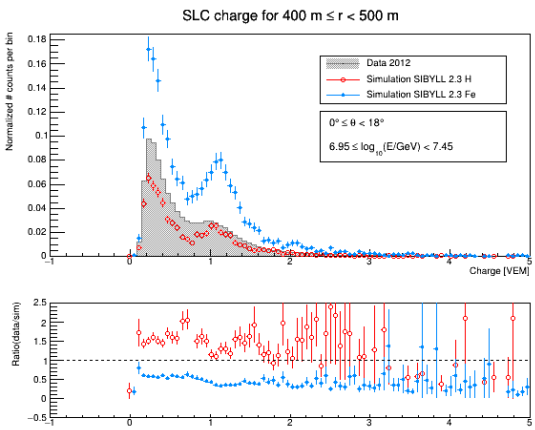
SLC charge for 400 m ≤ r < 500 m
Data 2012
Simulation SIBYLL 2.3 H
Simulation SIBYLL 2.3 Fe
0° ≤ θ < 18°
6.95 ≤ log10(E/GeV) < 7.45
Normalized # counts per bin
Charge [VEM]
Ratio(data/sim)

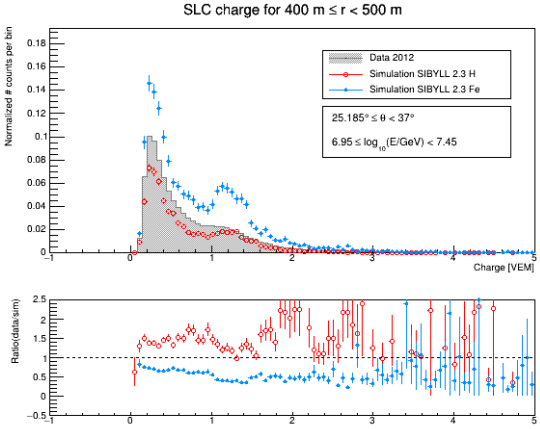
SLC charge for 400 m ≤ r < 500 m
Data 2012
Simulation SIBYLL 2.3 H
Simulation SIBYLL 2.3 Fe
25.185° ≤ θ < 37°
6.95 ≤ log10(E/GeV) < 7.45
Normalized # counts per bin
Charge [VEM]
Ratio(data/sim)

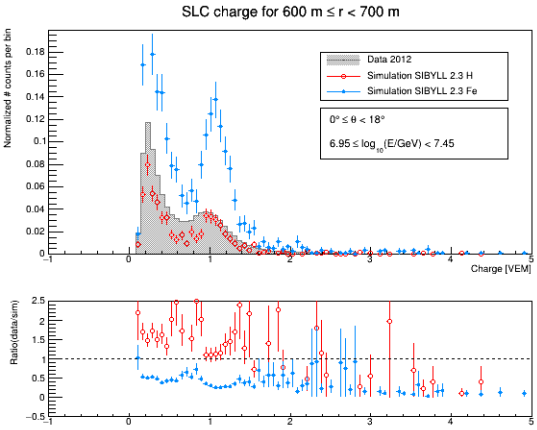
SLC charge for 600 m ≤ r < 700 m
Data 2012
Simulation SIBYLL 2.3 H
Simulation SIBYLL 2.3 Fe
0° ≤ θ < 18°
6.95 ≤ log10(E/GeV) < 7.45
Normalized # counts per bin
Charge [VEM]
Ratio(data/sim)

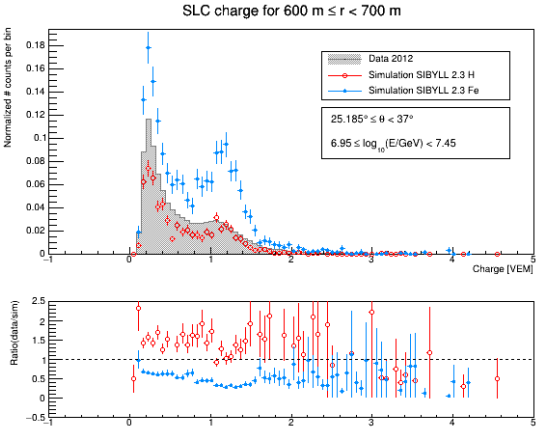
SLC charge for 600 m ≤ r < 700 m
Data 2012
Simulation SIBYLL 2.3 H
Simulation SIBYLL 2.3 Fe
25.185° ≤ θ < 37°
6.95 ≤ log10(E/GeV) < 7.45
Normalized # counts per bin
Charge [VEM]
Ratio(data/sim)

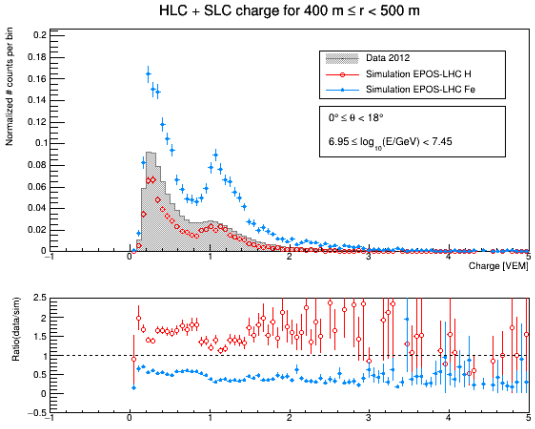
HLC + SLC charge for 400 m ≤ r < 500 m
Data 2012
Simulation EPOS-LHC H
Simulation EPOS-LHC Fe
0° ≤ θ < 18°
6.95 ≤ log10(E/GeV) < 7.45
Normalized # counts per bin
Charge [VEM]
Ratio(data/sim)

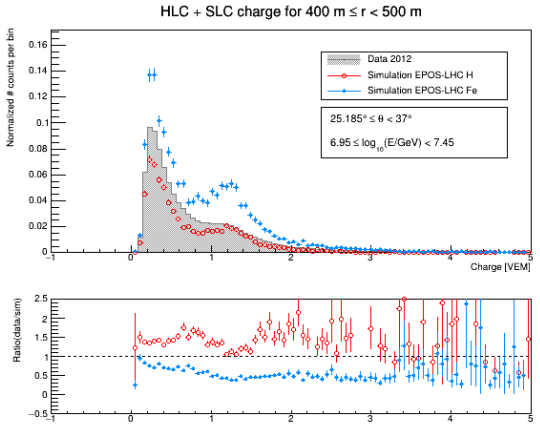
HLC + SLC charge for 400 m ≤ r < 500 m
Data 2012
Simulation EPOS-LHC H
Simulation EPOS-LHC Fe
25.185° ≤ θ < 37°
6.95 ≤ log10(E/GeV) < 7.45
Normalized # counts per bin
Charge [VEM]
Ratio(data/sim)

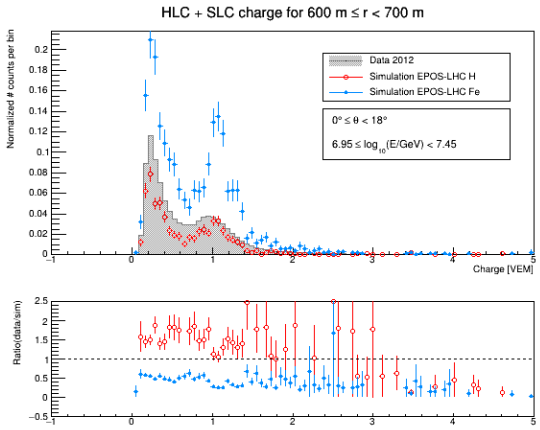
HLC + SLC charge for 600 m ≤ r < 700 m
Normalized # counts per bin
Data 2012
Simulation EPOS-LHC H
Simulation EPOS-LHC Fe
0° ≤ θ < 18°
6.95 ≤ log10(E/GeV) < 7.45
Charge [VEM]
Ratio(data/sim)

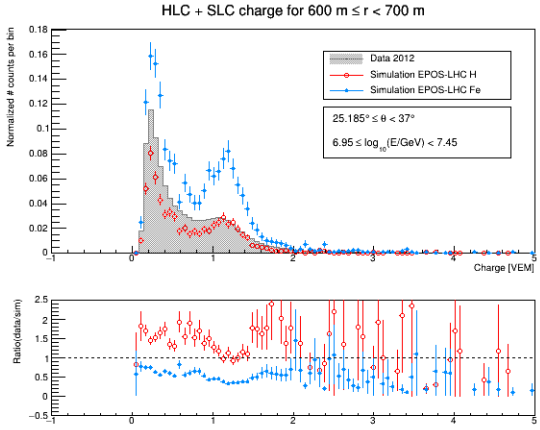
HLC + SLC charge for 600 m ≤ r < 700 m
Normalized # counts per bin
Data 2012
Simulation EPOS-LHC H
Simulation EPOS-LHC Fe
25.185° ≤ θ < 37°
6.95 ≤ log10(E/GeV) < 7.45
Charge [VEM]
Ratio(data/sim)

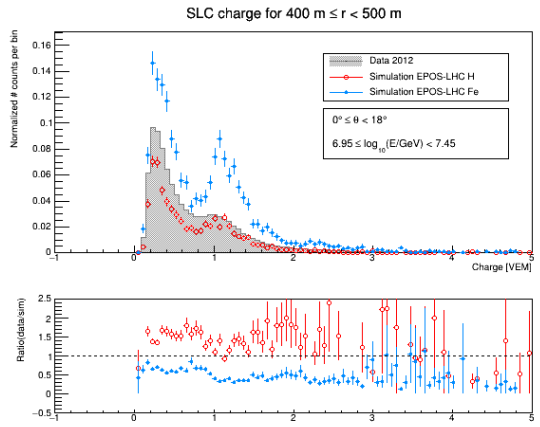
SLC charge for 400 m ≤ r < 500 m
Normalized # counts per bin
Data 2012
Simulation EPOS-LHC H
Simulation EPOS-LHC Fe
0° ≤ θ < 18°
6.95 ≤ log10(E/GeV) < 7.45
Charge [VEM]
Ratio(data/sim)

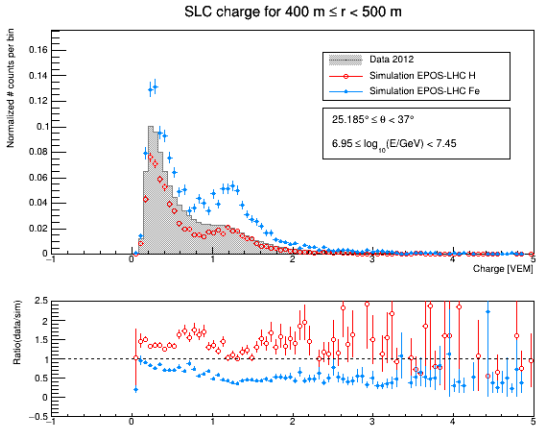
SLC charge for 400 m ≤ r < 500 m
Normalized # counts per bin
Data 2012
Simulation EPOS-LHC H
Simulation EPOS-LHC Fe
25.185° ≤ θ < 37°
6.95 ≤ log10(E/GeV) < 7.45
Charge [VEM]
Ratio(data/sim)

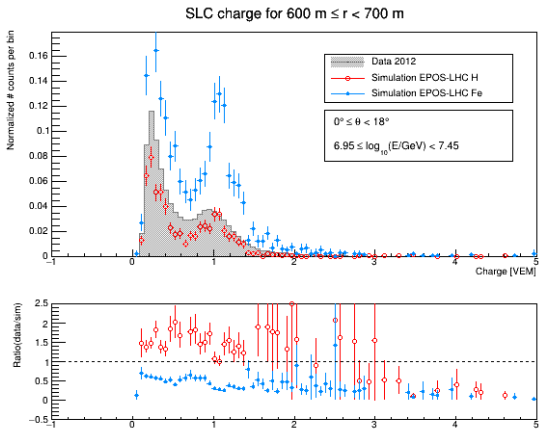
SLC charge for 600 m ≤ r < 700 m
Normalized # counts per bin
Data 2012
Simulation EPOS-LHC H
Simulation EPOS-LHC Fe
0° ≤ θ < 18°
6.95 ≤ log10(E/GeV) < 7.45
Charge [VEM]
Ratio(data/sim)

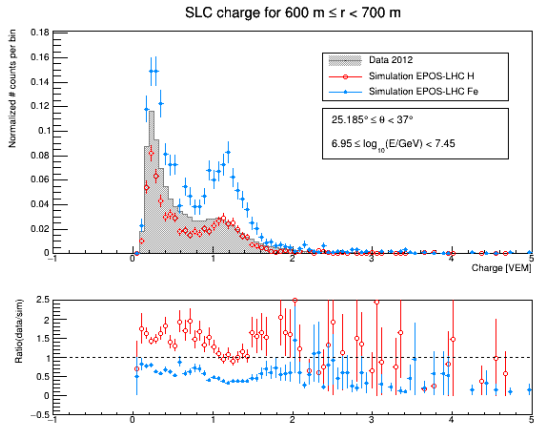
SLC charge for 600 m ≤ r < 700 m
Normalized # counts per bin
Data 2012
Simulation EPOS-LHC H
Simulation EPOS-LHC Fe
25.185° ≤ θ < 37°
6.95 ≤ log10(E/GeV) < 7.45
Charge [VEM]
Ratio(data/sim)

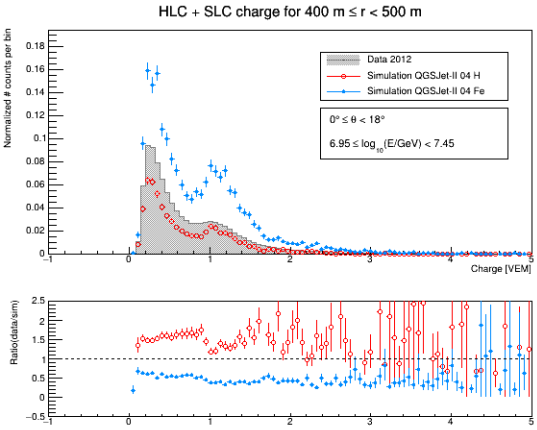
HLC + SLC charge for 400 m ≤ r < 500 m
Data 2012
Simulation QGSJet-II 04 H
Simulation QGSJet-II 04 Fe
0° ≤ θ < 18°
6.95 ≤ log10(E/GeV) < 7.45
Normalized # counts per bin
Charge [VEM]
Ratio(data/sim)

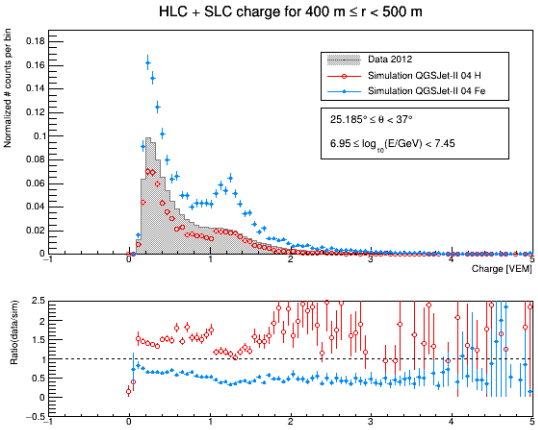
HLC + SLC charge for 400 m ≤ r < 500 m
Data 2012
Simulation QGSJet-II 04 H
Simulation QGSJet-II 04 Fe
25.185° ≤ θ < 37°
6.95 ≤ log10(E/GeV) < 7.45
Normalized # counts per bin
Charge [VEM]
Ratio(data/sim)

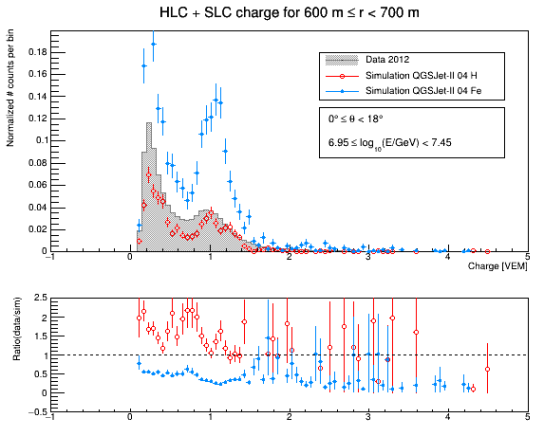
HLC + SLC charge for 600 m ≤ r < 700 m
Data 2012
Simulation QGSJet-II 04 H
Simulation QGSJet-II 04 Fe
0° ≤ θ < 18°
6.95 ≤ log10(E/GeV) < 7.45
Normalized # counts per bin
Charge [VEM]
Ratio(data/sim)

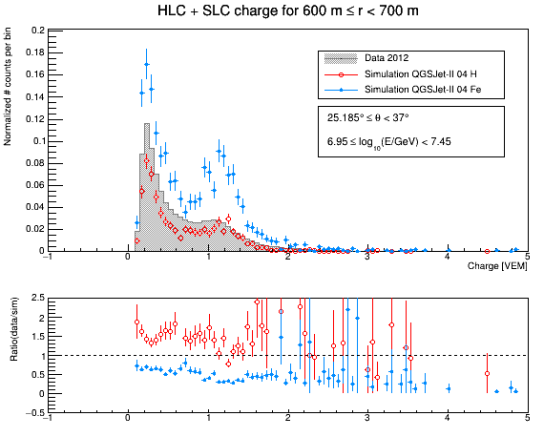
HLC + SLC charge for 600 m ≤ r < 700 m
Data 2012
Simulation QGSJet-II 04 H
Simulation QGSJet-II 04 Fe
25.185° ≤ θ < 37°
6.95 ≤ log10(E/GeV) < 7.45
Normalized # counts per bin
Charge [VEM]
Ratio(data/sim)

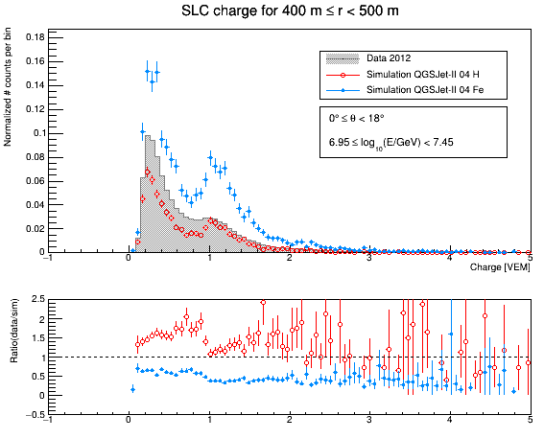
SLC charge for 400 m ≤ r < 500 m
Data 2012
Simulation QGSJet-II 04 H
Simulation QGSJet-II 04 Fe
0° ≤ θ < 18°
6.95 ≤ log10(E/GeV) < 7.45
Normalized # counts per bin
Charge [VEM]
Ratio(data/sim)

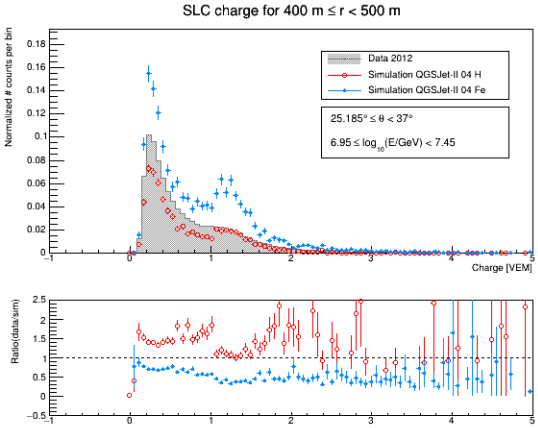
SLC charge for 400 m ≤ r < 500 m
Data 2012
Simulation QGSJet-II 04 H
Simulation QGSJet-II 04 Fe
25.185° ≤ θ < 37°
6.95 ≤ log10(E/GeV) < 7.45
Normalized # counts per bin
Charge [VEM]
Ratio(data/sim)

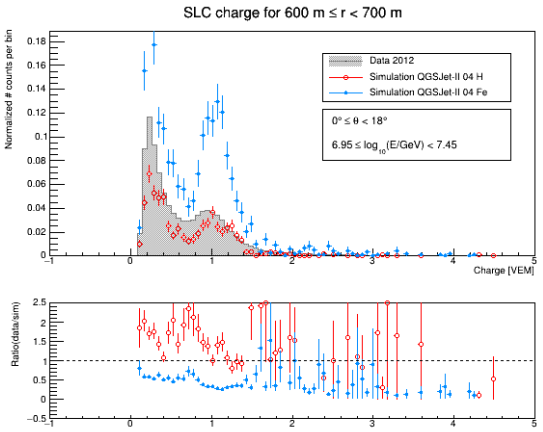

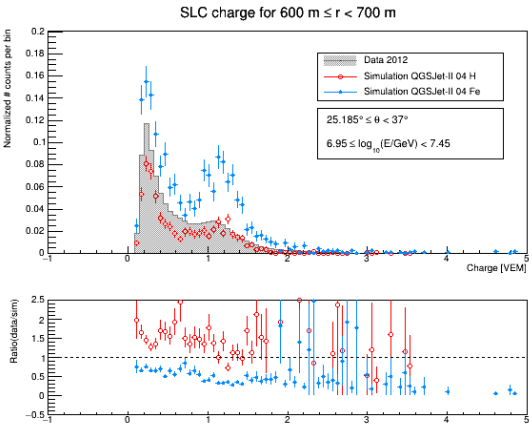

A.3. Comparing zenith angle ranges

In this Section, only the plots from the simulated data are shown because the plots for experimental data with different S_{125} cuts look nearly the same.

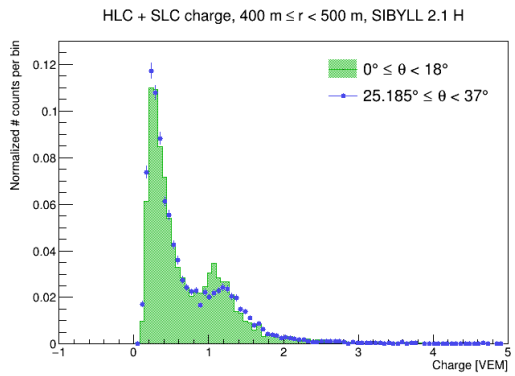

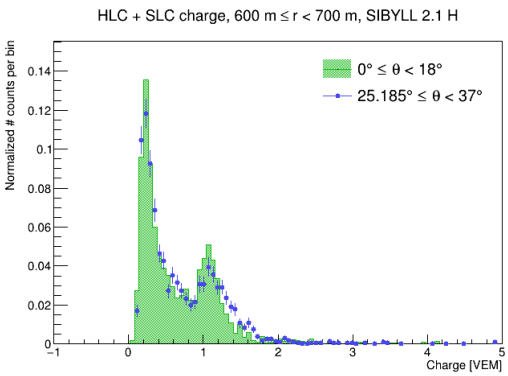

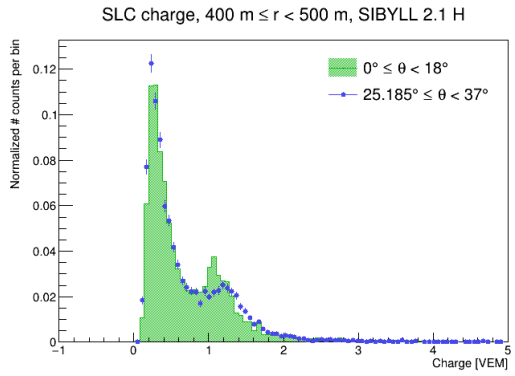

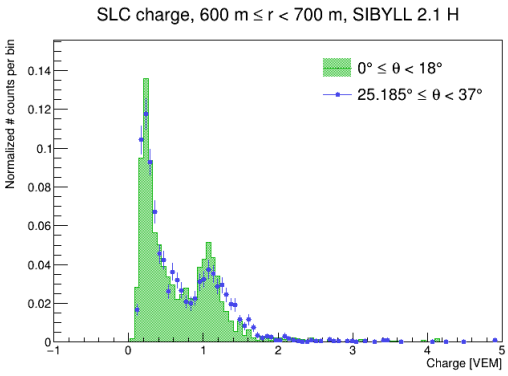

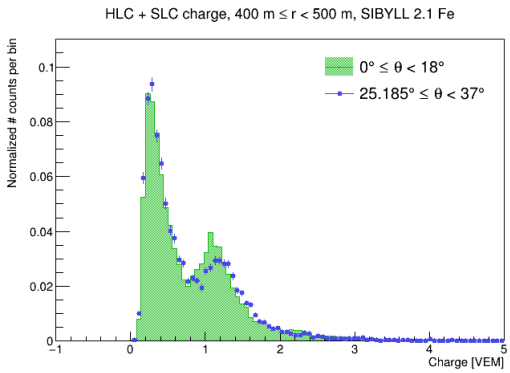
HLC + SLC charge, 400 m ≤ r < 500 m, SIBYLL 2.1 Fe
Normalized # counts per bin
Charge [VEM]
0° ≤ θ < 18°
25.185° ≤ θ < 37°

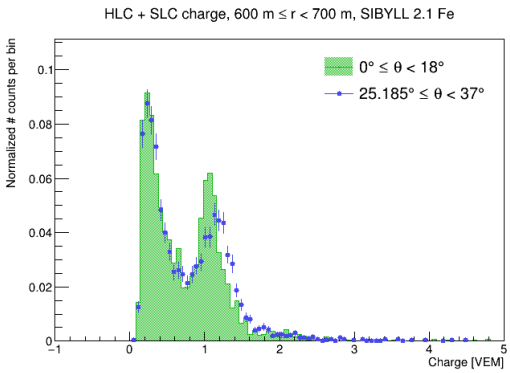
HLC + SLC charge, 600 m ≤ r < 700 m, SIBYLL 2.1 Fe
Normalized # counts per bin
Charge [VEM]
0° ≤ θ < 18°
25.185° ≤ θ < 37°

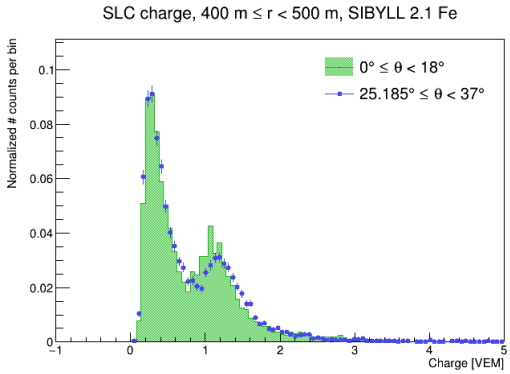
SLC charge, 400 m ≤ r < 500 m, SIBYLL 2.1 Fe
Normalized # counts per bin
Charge [VEM]
0° ≤ θ < 18°
25.185° ≤ θ < 37°

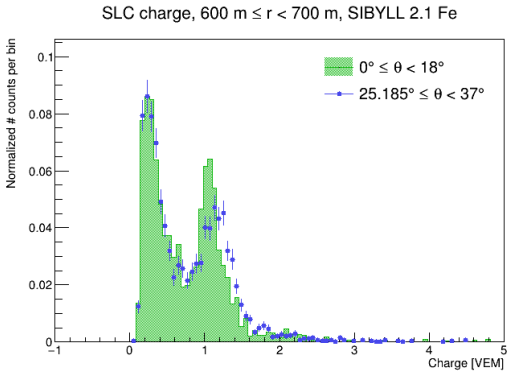
SLC charge, 600 m ≤ r < 700 m, SIBYLL 2.1 Fe
Normalized # counts per bin
Charge [VEM]
0° ≤ θ < 18°
25.185° ≤ θ < 37°

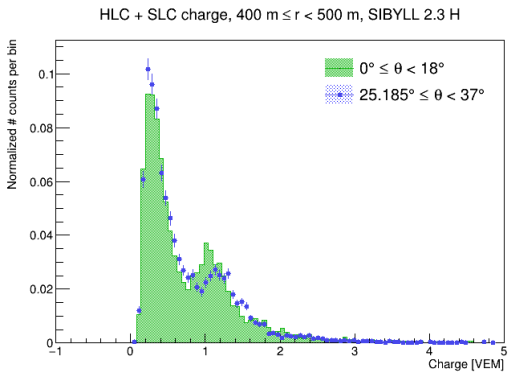
HLC + SLC charge, 400 m ≤ r < 500 m, SIBYLL 2.3 H
Normalized # counts per bin
Charge [VEM]
0° ≤ θ < 18°
25.185° ≤ θ < 37°

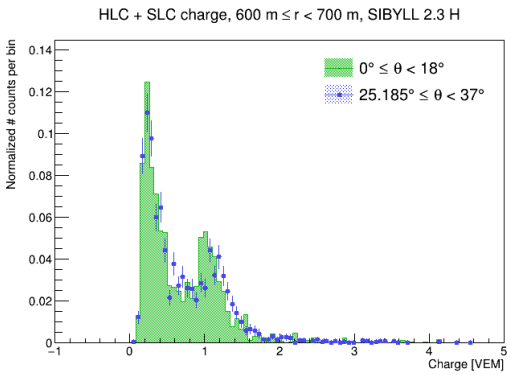
HLC + SLC charge, 600 m ≤ r < 700 m, SIBYLL 2.3 H
Normalized # counts per bin
Charge [VEM]
0° ≤ θ < 18°
25.185° ≤ θ < 37°

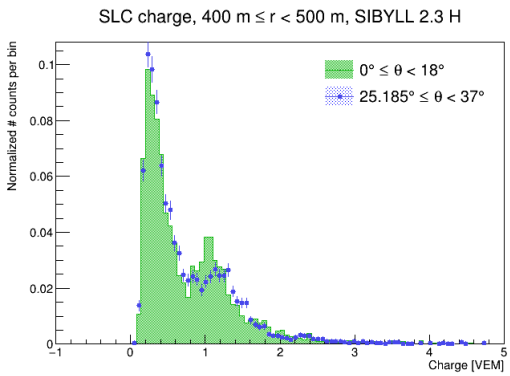
SLC charge, 400 m ≤ r < 500 m, SIBYLL 2.3 H
Normalized # counts per bin
Charge [VEM]
0° ≤ θ < 18°
25.185° ≤ θ < 37°

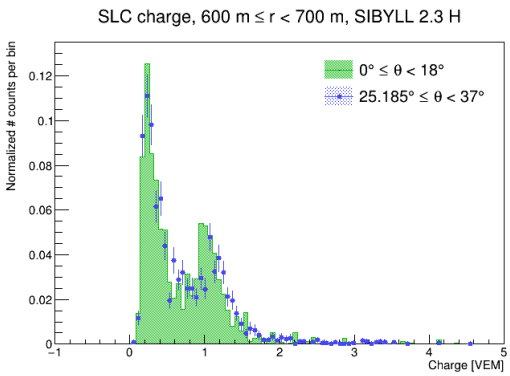
SLC charge, 600 m ≤ r < 700 m, SIBYLL 2.3 H
Normalized # counts per bin
Charge [VEM]
0° ≤ θ < 18°
25.185° ≤ θ < 37°

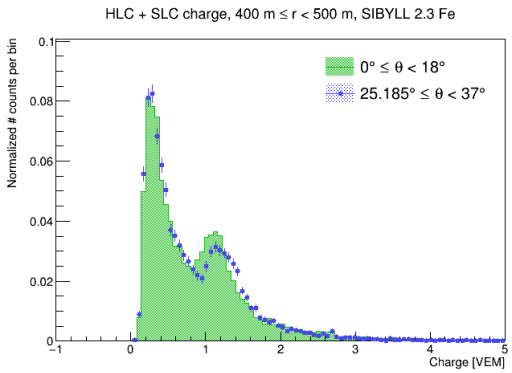
HLC + SLC charge, 400 m ≤ r < 500 m, SIBYLL 2.3 Fe
0° ≤ θ < 18°
25.185° ≤ θ < 37°
Normalized # counts per bin
Charge [VEM]

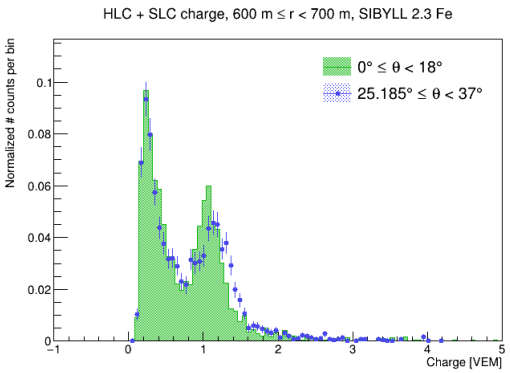
HLC + SLC charge, 600 m ≤ r < 700 m, SIBYLL 2.3 Fe
0° ≤ θ < 18°
25.185° ≤ θ < 37°
Normalized # counts per bin
Charge [VEM]

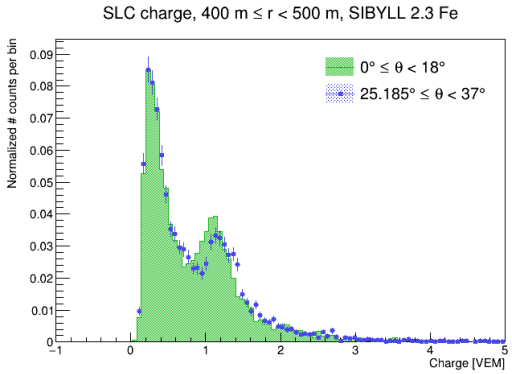
SLC charge, 400 m ≤ r < 500 m, SIBYLL 2.3 Fe
0° ≤ θ < 18°
25.185° ≤ θ < 37°
Normalized # counts per bin
Charge [VEM]

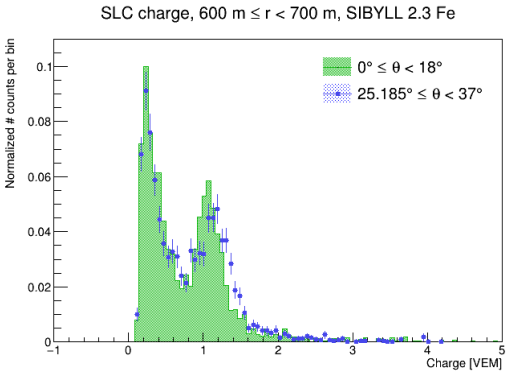
SLC charge, 600 m ≤ r < 700 m, SIBYLL 2.3 Fe
0° ≤ θ < 18°
25.185° ≤ θ < 37°
Normalized # counts per bin
Charge [VEM]

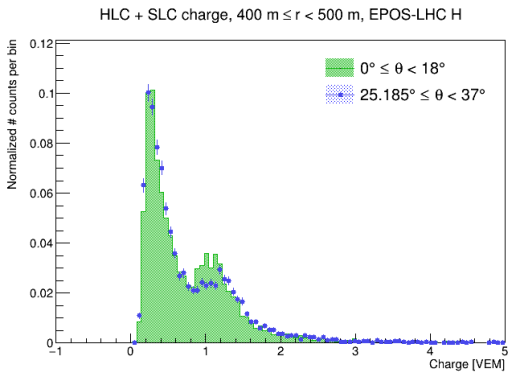
HLC + SLC charge, 400 m ≤ r < 500 m, EPOS-LHC H
0° ≤ θ < 18°
25.185° ≤ θ < 37°
Normalized # counts per bin
Charge [VEM]

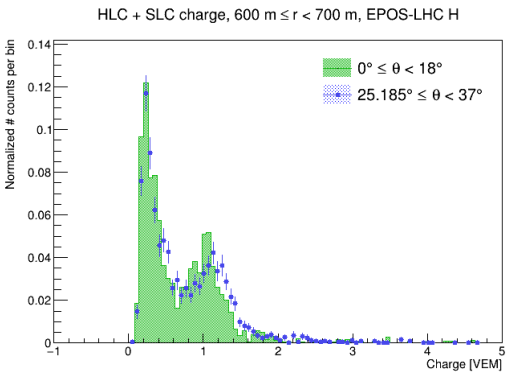
HLC + SLC charge, 600 m ≤ r < 700 m, EPOS-LHC H
0° ≤ θ < 18°
25.185° ≤ θ < 37°
Normalized # counts per bin
Charge [VEM]

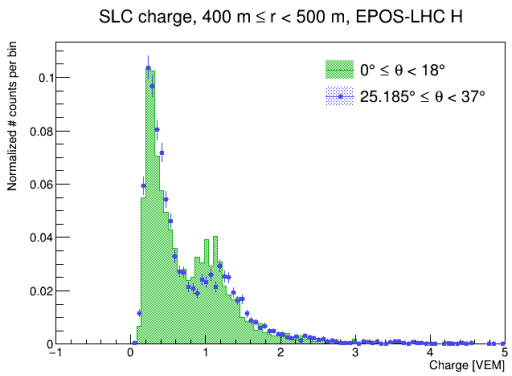
SLC charge, 400 m ≤ r < 500 m, EPOS-LHC H
0° ≤ θ < 18°
25.185° ≤ θ < 37°
Normalized # counts per bin
Charge [VEM]

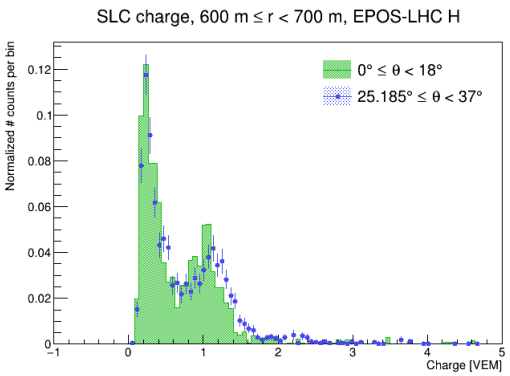
SLC charge, 600 m ≤ r < 700 m, EPOS-LHC H
0° ≤ θ < 18°
25.185° ≤ θ < 37°
Normalized # counts per bin
Charge [VEM]

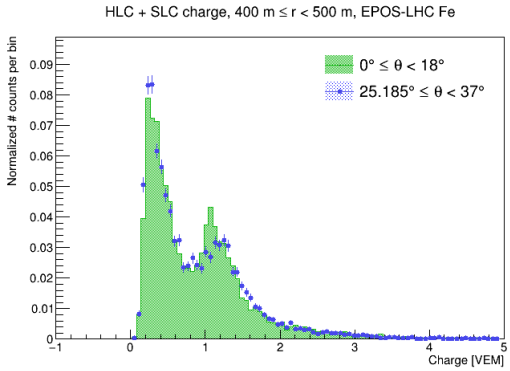
HLC + SLC charge, 400 m ≤ r < 500 m, EPOS-LHC Fe
0° ≤ θ < 18°
25.185° ≤ θ < 37°
Normalized # counts per bin
Charge [VEM]

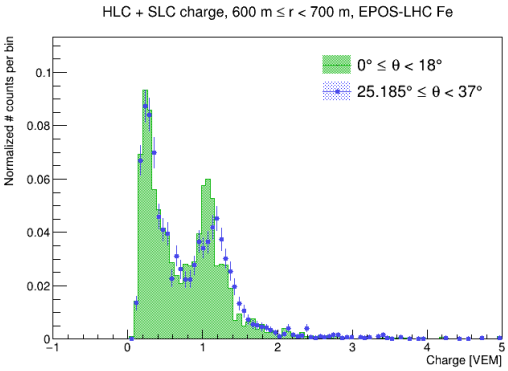
HLC + SLC charge, 600 m ≤ r < 700 m, EPOS-LHC Fe
0° ≤ θ < 18°
25.185° ≤ θ < 37°
Normalized # counts per bin
Charge [VEM]

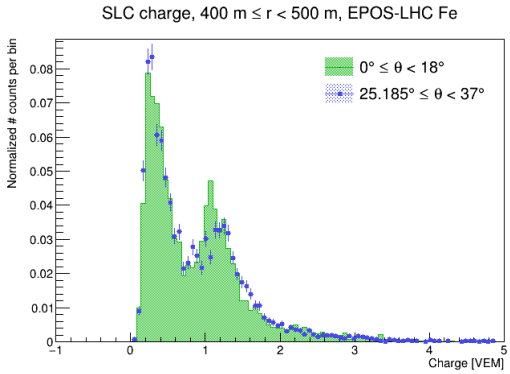
SLC charge, 400 m ≤ r < 500 m, EPOS-LHC Fe
0° ≤ θ < 18°
25.185° ≤ θ < 37°
Normalized # counts per bin
Charge [VEM]

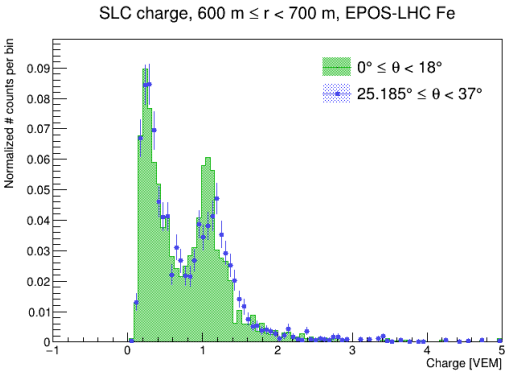
SLC charge, 600 m ≤ r < 700 m, EPOS-LHC Fe
0° ≤ θ < 18°
25.185° ≤ θ < 37°
Normalized # counts per bin
Charge [VEM]

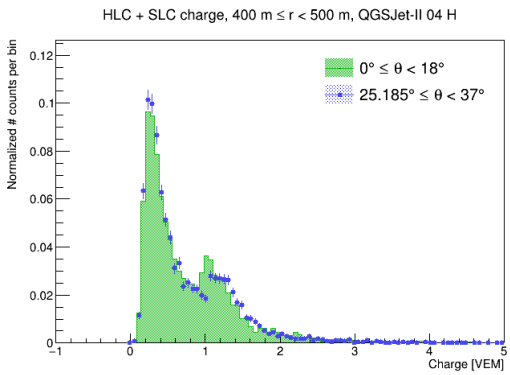
HLC + SLC charge, 400 m ≤ r < 500 m, QGSJet-II 04 H
0° ≤ θ < 18°
25.185° ≤ θ < 37°
Normalized # counts per bin
Charge [VEM]

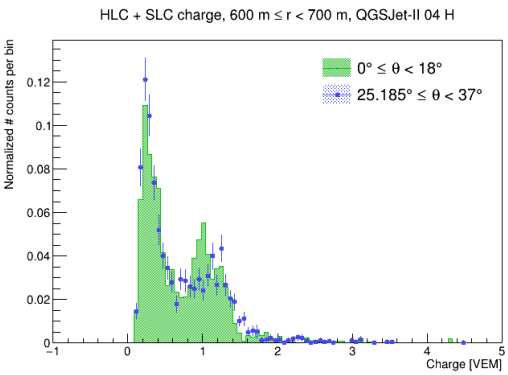
HLC + SLC charge, 600 m ≤ r < 700 m, QGSJet-II 04 H
0° ≤ θ < 18°
25.185° ≤ θ < 37°
Normalized # counts per bin
Charge [VEM]

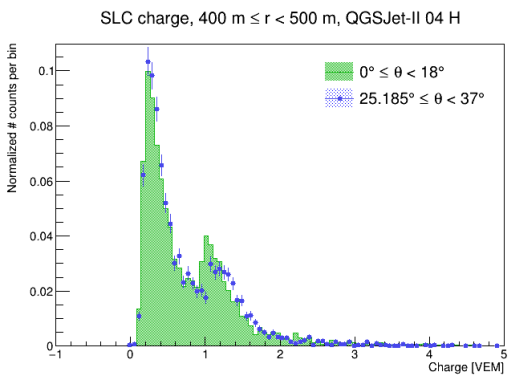
SLC charge, 400 m ≤ r < 500 m, QGSJet-II 04 H
0° ≤ θ < 18°
25.185° ≤ θ < 37°
Normalized # counts per bin
Charge [VEM]

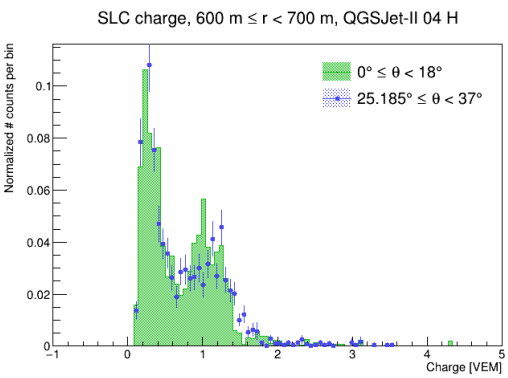
SLC charge, 600 m ≤ r < 700 m, QGSJet-II 04 H
0° ≤ θ < 18°
25.185° ≤ θ < 37°
Normalized # counts per bin
Charge [VEM]

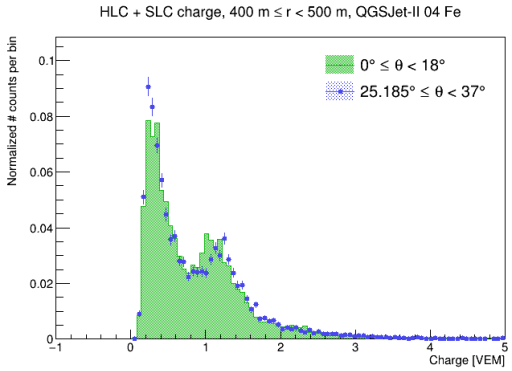
HLC + SLC charge, 400 m ≤ r < 500 m, QGSJet-II 04 Fe
Normalized # counts per bin
Charge [VEM]
0° ≤ θ < 18°
25.185° ≤ θ < 37°

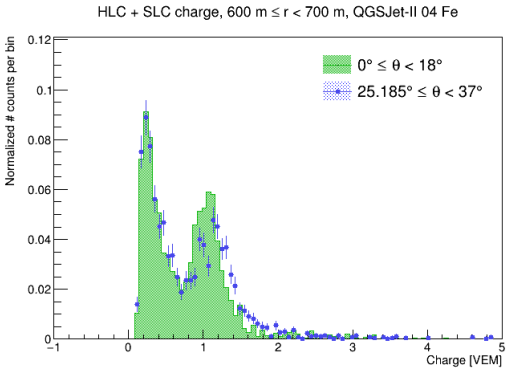
HLC + SLC charge, 600 m ≤ r < 700 m, QGSJet-II 04 Fe
Normalized # counts per bin
Charge [VEM]
0° ≤ θ < 18°
25.185° ≤ θ < 37°

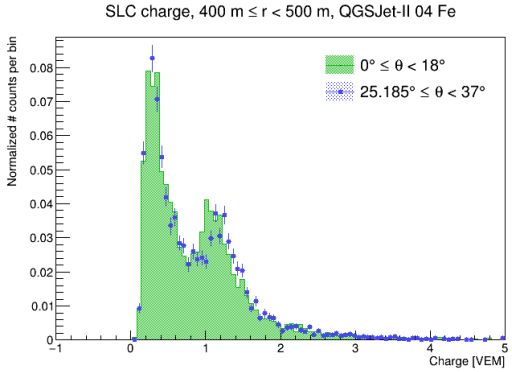
SLC charge, 400 m ≤ r < 500 m, QGSJet-II 04 Fe
Normalized # counts per bin
Charge [VEM]
0° ≤ θ < 18°
25.185° ≤ θ < 37°

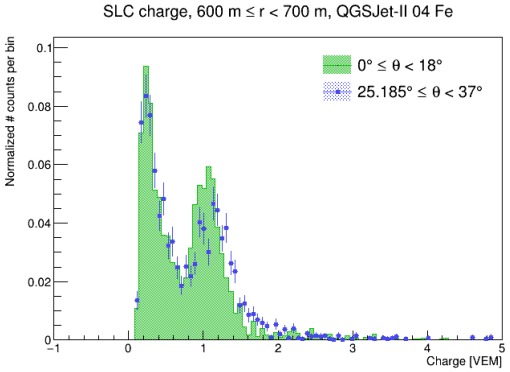
SLC charge, 600 m ≤ r < 700 m, QGSJet-II 04 Fe
Normalized # counts per bin
Charge [VEM]
0° ≤ θ < 18°
25.185° ≤ θ < 37°

A.4. Comparing different interaction models

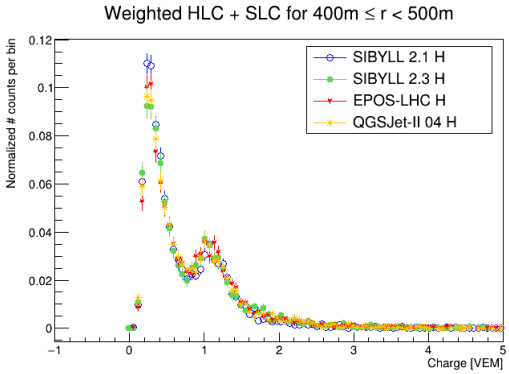

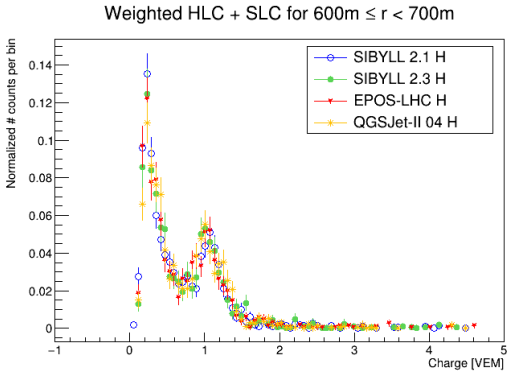

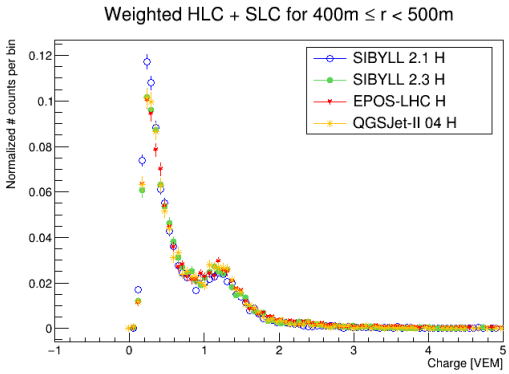

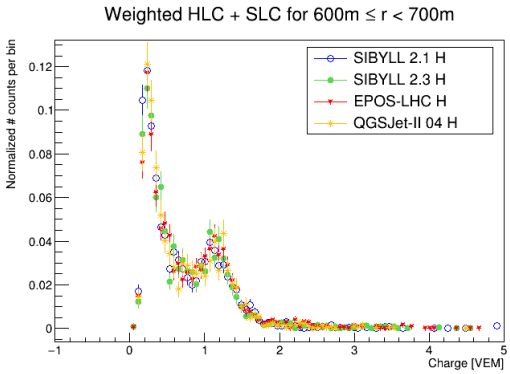

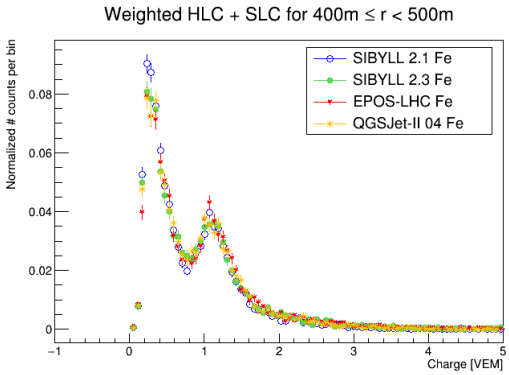

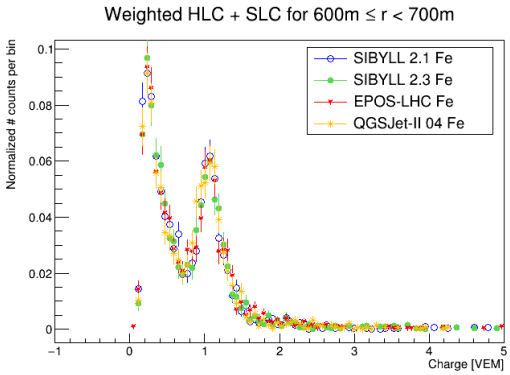

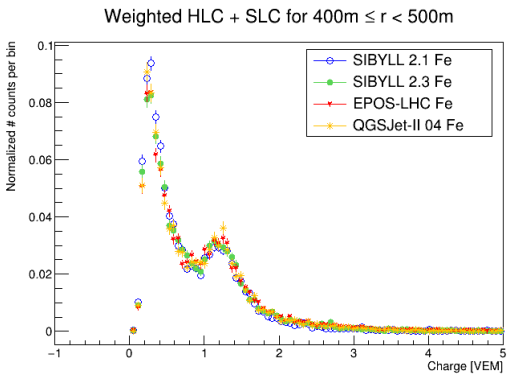

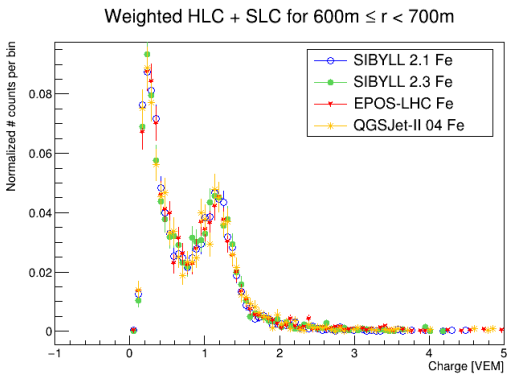

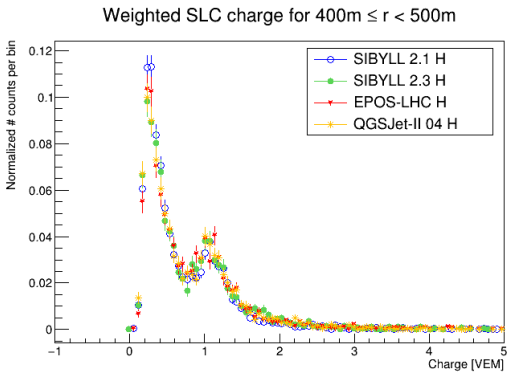
Weighted SLC charge for 400m ≤ r < 500m
SIBYLL 2.1 H
SIBYLL 2.3 H
EPOS-LHC H
QGSJet-II 04 H
Normalized # counts per bin
Charge [VEM]

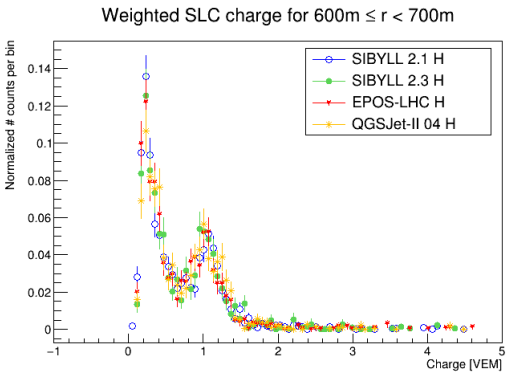
Weighted SLC charge for 600m ≤ r < 700m
SIBYLL 2.1 H
SIBYLL 2.3 H
EPOS-LHC H
QGSJet-II 04 H
Normalized # counts per bin
Charge [VEM]

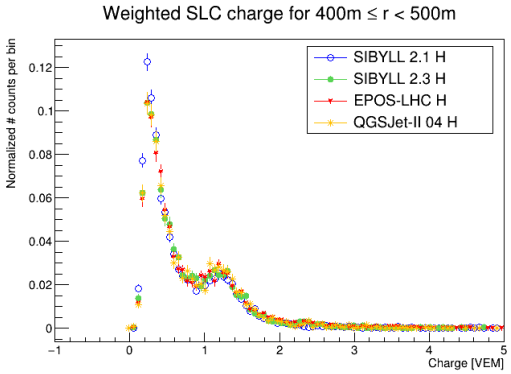
Weighted SLC charge for 400m ≤ r < 500m
SIBYLL 2.1 H
SIBYLL 2.3 H
EPOS-LHC H
QGSJet-II 04 H
Normalized # counts per bin
Charge [VEM]

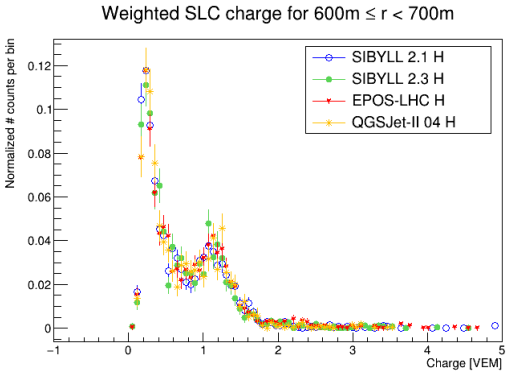
Weighted SLC charge for 600m ≤ r < 700m
SIBYLL 2.1 H
SIBYLL 2.3 H
EPOS-LHC H
QGSJet-II 04 H
Normalized # counts per bin
Charge [VEM]

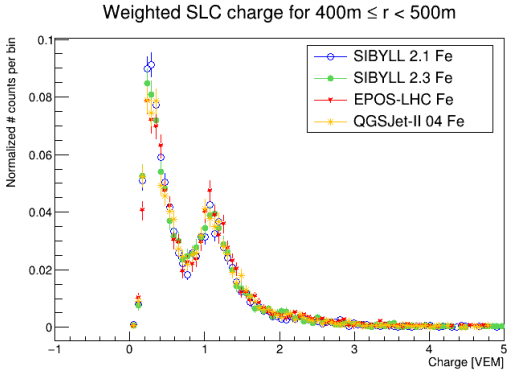
Weighted SLC charge for 400m ≤ r < 500m
SIBYLL 2.1 Fe
SIBYLL 2.3 Fe
EPOS-LHC Fe
QGSJet-II 04 Fe
Normalized # counts per bin
Charge [VEM]

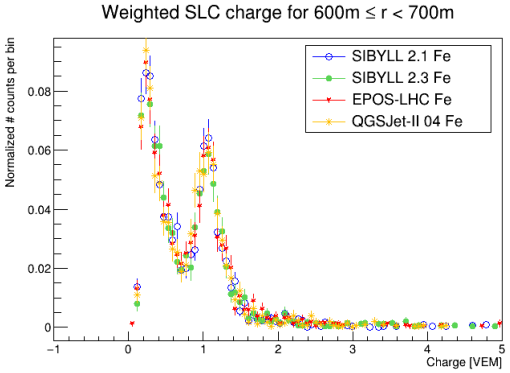
Weighted SLC charge for 600m ≤ r < 700m
SIBYLL 2.1 Fe
SIBYLL 2.3 Fe
EPOS-LHC Fe
QGSJet-II 04 Fe
Normalized # counts per bin
Charge [VEM]

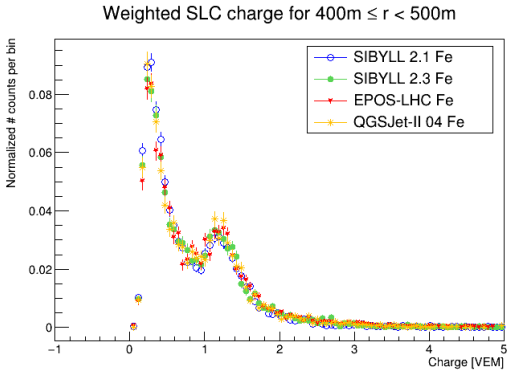
Weighted SLC charge for 400m ≤ r < 500m
SIBYLL 2.1 Fe
SIBYLL 2.3 Fe
EPOS-LHC Fe
QGSJet-II 04 Fe
Normalized # counts per bin
Charge [VEM]

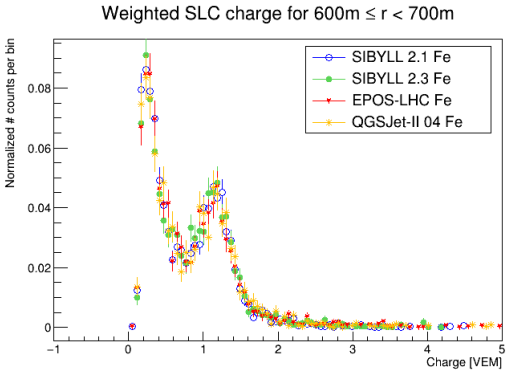
Weighted SLC charge for 600m ≤ r < 700m
SIBYLL 2.1 Fe
SIBYLL 2.3 Fe
EPOS-LHC Fe
QGSJet-II 04 Fe
Normalized # counts per bin
Charge [VEM]

Acknowledgments

I would like to thank Ralph Engel and Kathrin Valerius for reviewing this thesis.
I thank Andreas Haungs very much for taking me on board the IceCube team and giving me the freedom and time to combine my work with being there for my two children as much as possible. I thank him for his supervision, help and encouragement.
I thank my advisor Donghwa Kang a lot for her amazing supervision and all the time she invested in me. I have to thank her so much for her patience and encouragement along the way, all the help she gave me to make me complete this thesis, and for being such a kind and lovely person to work with.
I thank Doris Wochele for her administrative help. I couldn't have even started my work without her.
I also thank Sabine Bucher for bureaucratic support.
I thank the whole IceCube group for welcoming me in the team and supporting me in my work. A special thanks belongs to Marie, Agniezska, Fiona and Shefali for being such kind and supportive office mates.
I thank my friends Rebecca, Steffen and Roman for helping me with my programming challenges.
A big thank you belongs to my faithful babysitters Kathi and Daniela for taking good care of my little children so that I had more time to work on this thesis.
I thank my parents, siblings and all my other friends near and far very much for supporting, encouraging and helping me over the whole year.
Most of all I thank my wonderful husband George, and my two children Aaron and Abigail, for helping and supporting me in every way possible. I thank them for their love, patience and encouragement which carried me through this year.
Thank you, Jesus, for always being with me, guiding my steps and making every day worth living.

Karlsruhe, 09.09.2021

Sally-Ann Browne